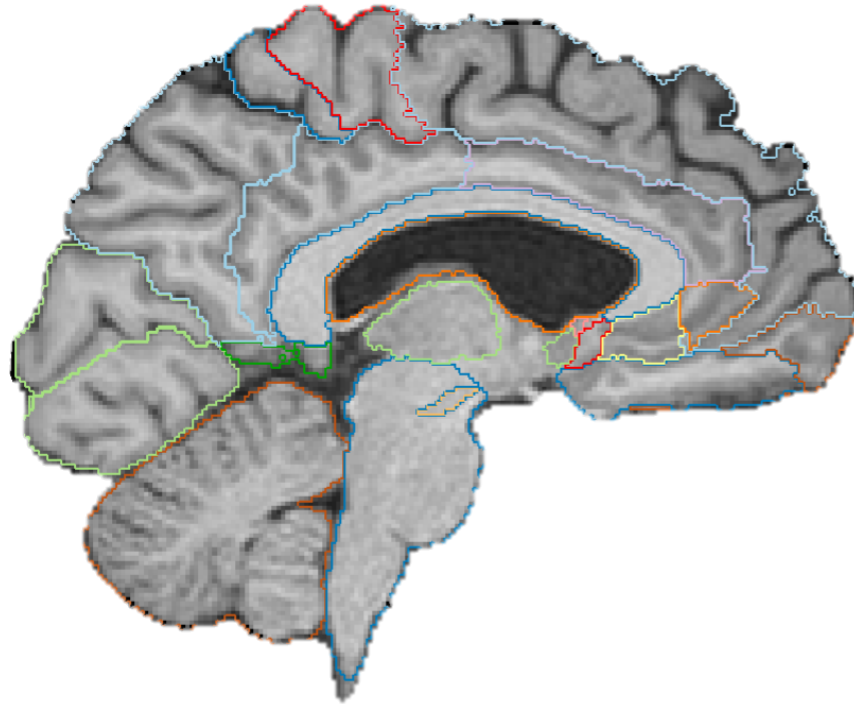




CHALMERS
UNIVERSITY OF TECHNOLOGY



Parkinson's disease and epilepsy: linked entities?

A brain morphometry study with multi-atlas based anatomical segmentation

Master's thesis in Biomedical Engineering

REBECCA HENRYSSON

DEPARTMENT OF ELECTRICAL ENGINEERING

CHALMERS UNIVERSITY OF TECHNOLOGY

Gothenburg, Sweden 2021

www.chalmers.se

MASTER'S THESIS 2021

Parkinson's disease and epilepsy: linked entities?

A brain morphometry study with multi-atlas based anatomical segmentation

REBECCA HENRYSSON



CHALMERS
UNIVERSITY OF TECHNOLOGY

Department of Electrical Engineering
Division of Signal processing and Biomedical engineering
CHALMERS UNIVERSITY OF TECHNOLOGY
Gothenburg, Sweden 2021

Parkinson's disease and epilepsy: linked entities?
A brain morphometry study with multi-atlas based anatomical segmentation
REBECCA HENRYSSON

© REBECCA HENRYSSON, 2021.

Supervisor: Professor Rolf A. Heckemann, Department of Medical Radiation Sciences, Gothenburg University
Examiner: Professor Fredrik Kahl, Department of Electrical Engineering, Chalmers Tehnology of University

Master's Thesis 2021
Department of Electrical Engineering
Division of Signal processing and Biomedical engineering
Chalmers University of Technology
SE-412 96 Gothenburg
Telephone +46 31 772 1000

Cover: Visualisation of brain region segmentation with MAPER using MIRTk Viewer.

Typeset in L^AT_EX
Printed by Chalmers Reproservice
Gothenburg, Sweden 2021

Parkinson's disease and epilepsy: linked entities?

A brain morphometry study with multi-atlas based anatomical segmentation

REBECCA HENRYSSON

Department of Electrical Engineering

Chalmers University of Technology

Abstract

Purpose

This study set out to explore brain volumes in study participants suffering from Parkinson's disease (PD) by conducting a region-wise morphometry study with the automatic anatomical image segmentation software MAPER. Secondly, the study seeks to shed light on the neuromorphological characteristics that PD and epilepsy have in common.

Method

This study utilised cross-sectional data obtained from the Parkinson's Progression Markers Initiative (PPMI). I obtained 3D and 2D T1-weighted MR images and meta-data from 958 subjects of the PPMI database. All images were preprocessed for B1 nonuniformity, header reorientation and brain extraction. Subsequently, region-wise segmentation was performed on the MR data using the atlas-based image segmentation software MAPER and the Hammers Atlas Database of the human brain. The 95 segmented brain regions for each subject were normalised using a residual regression-based ICV normalisation method. I used a split-group hypothesis generation and testing design to conduct statistical comparisons between the participants and the control group.

Result

Significant volume differences between the control and study participants were found in the ICV, in regions along the nigrostriatal pathway, and in regions within the temporal lobe.

Conclusion

This thesis suggests that de novo PD subjects have a significantly larger intracranial volume than controls, which is consistent with earlier studies. The study revealed evidence that the volume of *Pallidum* is greater in PD subjects compared to healthy controls. In contrast to earlier studies, this study provides no evidence of significant differences in *Thalamus*, *Putamen*, and *Caudate nucleus* volume compared to controls. I showed that the intracranial volume in epilepsy subjects was significantly larger compared to the controls. No association between PD and epilepsy subjects was evident. Findings reported in this thesis suggest that there might be a coupling between a PD genetic mutation and participants without PD suffering from hypsomia or REM sleep behaviour disorder, associated with the region *Substantia nigra* and regions within the temporal lobe.

Keywords: Magnetic resonance imaging, Parkinson's disease, epilepsy, biomarker, region-wise brain morphometry, multi-atlas based segmentation.

Acknowledgements

First and foremost, I would like to express my sincere gratitude to my supervisor Professor Rolf A. Heckemann, for giving me the opportunity to do this incredibly interesting project. Thank you for your constant encouragement, patient, support and valuable guidance. I am grateful that you have shared your expertise and always encouraged me to deepen my knowledge in medical imaging and strive for a rewarding thesis. Without your contribution, this thesis would not have been possible.

I also want to express my gratitude to my examiner Fredrik Kahl, for providing guidance and feedback throughout this project. Finally, my deep and sincere gratitude to my family and friends, for their unwavering support and belief in me.

Rebecca Henrysson, Gothenburg, September 2021

Contents

List of Figures	xi
List of Tables	xiii
1 Introduction	1
1.1 Background	1
1.2 Aim & Outcomes	3
1.3 Demarcations	3
2 Theory	5
2.1 Data acquisition with MRI	5
2.1.1 The MRI technique	6
2.1.2 Acquisition parameters	8
2.1.3 Data acquisition	9
2.1.4 Image reconstruction	11
2.1.5 MR image quality	11
2.1.6 MR image artefacts	13
2.2 Medical image preprocessing	14
2.2.1 Intensity non-uniformity correction	14
2.2.2 Brain extraction	15
2.2.3 Reorientation	15
2.2.4 Spatial interpolation	15
2.2.5 Noise reduction	16
2.3 Medical image registration	16
2.3.1 Transformation model	16
2.3.2 Registration basis	18
2.4 Medical image segmentation	19
2.4.1 Multi-atlas segmentation	20
3 Materials and methods	23
3.1 MR data	23
3.2 Study design	24
3.3 High performance computing cluster	25
3.4 Preprocessing	25
3.5 Brain extraction with Pinfram	25
3.5.1 Atlas	27
3.6 Multi-atlas segmentation with MAPER	27

3.6.1	The Hammers atlas	28
3.6.2	Measures of segmentation success	28
3.7	Statistical analysis	29
3.7.1	Individual regions	29
3.7.2	Difference index between ICV and parenchyma volumes	30
3.7.3	Asymmetry	30
3.7.4	Multiple comparison	30
4	Results	31
4.1	Quality of intracranial masks	31
4.2	Quality of individual region segmentation	31
4.3	Exploration and hypothesis generation	32
4.3.1	Intracranial volume	32
4.3.2	Difference index	32
4.3.3	Individual region analysis	33
4.3.4	Asymmetry	42
4.4	Hypothesis testing	44
4.4.1	Intracranial volume	44
4.4.2	Difference index	44
4.4.3	Individual region analysis	46
4.4.4	Asymmetry	56
4.5	Key findings	62
5	Discussion	65
5.1	Intracranial volume	65
5.2	Difference between ICV and parenchyma	65
5.3	Individual regional volume	65
5.4	Asymmetry	67
6	Conclusion	69
	Bibliography	71
A	Hypotheses	I

List of Figures

2.1	The figure visualises protons with and without exposure to a strong magnetic field	7
2.2	The figure visualises what happens to the net magnetisation vector, M_0 , prior to and after applying the RF pulse	8
2.3	The figure visualises the two relaxation phenomena T1 and T2 relaxation, which takes place when the RF pulse is switched off	8
2.4	Comparison between T1, T2 and Proton Density weighted image, produced with a spin echo sequence [30]	10
2.5	Effects of turning on the gradient coils	10
2.6	Data acquisition	11
2.7	Difference between field of view and pixel	12
2.8	Three examples of common artefacts that may occur in an MR image	14
2.9	The figure visualises the process of multi-atlas based segmentation.	21
3.1	A schematic overview of the Pinfram algorithm, where M'_ℓ is the output from the each iteration [46]	26
3.2	Pinfram output visualised with MIRTk Viewer: 3.2a the ICV mask from the first iteration and 3.2b the parenchyma mask from the last iteration	26
3.3	Label output from MAPER, visualised using MIRTk Viewer	29
4.1	A violin boxplot with the intracranial volumes of the exploration half of the cohort groups	33
4.2	The figure shows a violin boxplot of the Difference index between ICV and parenchyma volume for the exploration group.	33
4.3	Fingerprint plot of the 95 regions comparing the control group against the PD group	35
4.4	Fingerprint plot of the 95 regions comparing the control group against the SWEDD group	36
4.5	Fingerprint plot of the 95 regions comparing the control group against the GenPD group	37
4.6	A fingerprint plot of the 95 regions comparing the control group against the GenUn group	38
4.7	A fingerprint plot of the 95 regions comparing the control group with the Pr group	39
4.8	Fingerprint plot of the 95 regions comparing the control group with the E group	41

4.9	Asymmetry index for selected regions	42
4.10	Asymmetry index for selected regions	43
4.11	A violin boxplot with the intracranial volumes for the test half group	44
4.12	The figure shows a violin boxplot of the Difference index between ICV and parenchyma volume for the test group	45
4.13	Volumes for selected regions	47
4.14	Volumes for selected regions	50
4.15	Asymmetry index for selected regions	56
4.16	Asymmetry index for selected regions	60

List of Tables

2.1	Table of T1 and T2 relaxation times for various tissues with a magnetic field strength of 1.5 T [27].	9
3.1	Distribution of cohorts, gender and epilepsy participants within the cohort groups.	24
3.2	Overview of the MAPER steps for generating an individual segmentation	28
4.1	Distribution of cohort and gender after evaluating the Pinfram results. The table also presents how many epilepsy participants belonged to each cohort.	31
4.2	Distribution of cohort and gender after evaluating the MAPER results. The table also presents how many epilepsy participants belong to each cohort.	32
4.3	Distribution of participants in randomly generated exploration and test groups.	32
4.4	Results from the unpaired t-test for ICV.	45
4.5	Results from the unpaired t-test for Difference index comparing ICV and Parenchyma.	46
4.6	Results from the unpaired t-test for Thalamus.	48
4.7	Results from the unpaired t-test for Putamen.	48
4.8	Results from the unpaired t-test for Pallidum.	49
4.9	Results from the unpaired t-test for Nucleus accumbens.	49
4.10	Results from the unpaired t-test for Caudate nucleus.	50
4.11	Results from the unpaired t-test for Substantia nigra.	51
4.12	Results from the unpaired t-test for Hippocampus.	52
4.13	PD specific regions.	52
4.14	SWEDD specific regions.	53
4.15	Pr specific regions.	54
4.16	GenUn specific regions.	54
4.17	GenPD specific regions.	55
4.18	E specific regions.	55
4.19	Results from the unpaired t-test for Thalamus.	57
4.20	Results from the unpaired t-test for Putamen.	57
4.21	Results from the unpaired t-test for Pallidum.	58
4.22	Results from the unpaired t-test for Nucleus accumbens.	59
4.23	Results from the unpaired t-test for Caudate nucleus.	59

4.24	Results from the unpaired t-test for Substantia nigra.	61
4.25	Results from the unpaired t-test for Hippocampus.	61
A.1	Summation of hypotheses generated for the intracranial volume. . . .	I
A.2	Summation of hypotheses generated for DI.	II
A.3	Summation of hypotheses generated for individual regions in the PD cohort.	III
A.4	Summation of hypotheses generated for individual regions in the SWEDD cohort.	IV
A.5	Summation of hypotheses generated for individual regions in the GenPD cohort.	V
A.6	Summation of hypotheses generated for individual regions in the GenUn cohort.	VI
A.7	Summation of hypotheses generated for individual regions in the Pr cohort.	VII
A.8	Summation of hypotheses generated for individual regions in the E cohort.	VIII
A.9	Generated hypothesis (H_A) for asymmetry index.	IX

Acronyms

DI : Difference index between ICV and parenchyma volume. 30, 32

FOV : Field of view. 12

ICV : intracranial volume. v, xi, xiii, 3, 25, 26, 29–32, 44–46, 62, 65

MR : Magnetic resonance. 6, 9, 11, 12, 14

MRI : Magnetic resonance imaging. 5–7, 9, 11, 13, 15

PD : Parkinson’s disease. v, 1–3

PPMI : Parkinson’s Progression Markers Initiative. 23–25

RF : Radiofrequency. 7, 9, 12

SNR : Signal-to-noise ratio. 11, 12

1

Introduction

1.1 Background

Neurological disorders have received considerable scholarly attention in recent years as they are a significant contributing factor to the global burden of disability. Among neurological disorders, Parkinson's disease (PD) is the second most common age-related neurodegenerative disorder after Alzheimer's disease [1]. Perhaps the most comprehensive account of the prevalence of PD is found in the systematic review *Global, regional, and national burden of Parkinson's disease, 1990–2016* [2]. Dorsey et al. reported that approximately 6.1 million individuals suffered from PD worldwide in 2016, however, other studies suggest that the number of individuals might be higher considering the fact that many people go undiagnosed [2]–[4]. Further, Dorsey et al. reported that the number of Parkinson's patients has more than doubled since 1990 and addresses increasing numbers of an older population as one of the key reasons. Age is a significant risk factor for PD, and the prevalence of PD steadily with age [1]. PD usually occurs in people between 65 and 70 years of age, and around 1 % of the global population over the age of 60 suffer from PD [1]. Only approximately 5 % of the PD incidence is seen in the population younger than 40 [1].

PD is a chronic neurodegenerative disease characterised by the motor symptoms tremor, rigidity and bradykinesia [5]. In addition to the three motor symptoms, PD individuals experience several general non-motor symptoms such as sleeping problem, fatigue, mood disorders like depression or anxiety, loss of speech, drooling, and swallowing problems [6]. The mechanisms that underpin PD are not fully understood, and the cause of the disease is currently unknown. However, there is a consensus among scientists that PD is related to lack of dopamine in the substantia nigra, a midbrain region involved in reward and movement. The existing literature on PD has highlighted several regions of interest showing a significant volume difference between PD participants and controls. Among them, Tamari and Utsunomiya showed that the volume of the substantia nigra was significantly lower in PD participants compared to a healthy control [7]. Two papers on regional volume analysis of PD ([8] [9]) agree in suggesting that there is a significant difference in volume in caudate nucleus between PD participants and controls. In addition, evidence for significant difference in thalamus and putamen volume was found in [8] [9]. More-

over, Krabbe et al. showed that the intracranial volumes of PD participants were larger than for the control group [10].

One unanticipated finding on substantia nigra was reported by Keihaninejad et al. in a morphometric study of temporal lobe epilepsy. Keihaninejad et al. observed that the substantia nigra was smaller in the hemisphere containing the epileptic seizure focus, compared to the other hemisphere [11]. This rather unexpected observation raises the question whether epilepsy may be related to PD. Previous studies have explored the relationships between PD and Epilepsy [12]–[14]. A possible relationship between Parkinson’s disease and epilepsy was observed for the first time in 1928 by Yakovlev, who noticed a decrease in seizure frequency in four patients after they developed parkinsonism [13]. A more recent study by Gruntz et al. showed that the prevalence of epilepsy in PD individuals was higher compare to PD-free individuals (266.7/100,000 person-years compared to 112.4/100,000 person-years) [12].

To date, much is still uncertain about the neurobiological basis of both PD and epilepsy. Epilepsy can generally be diagnosed by examination with electroencephalography (EEG). In contrast to epilepsy, there is no definitive test for PD due to absence of a significant biomarker. Instead, identifying two or more of the characteristic signs and symptoms is required to determine a diagnosis [15]. The lack of more definitive diagnostic criteria leads to a high misdiagnosis rate and indicates a need for a robust diagnostic methodology [15]. The Parkinson’s Progression Markers Initiative (PPMI) study is currently the largest observational, international, multi-center study launched and largely sponsored by the Michael J Fox Foundation, designed to search for PD progression biomarkers [16], [17]. PPMI calls for researchers in the field of PD to use PPMI’s shared data to understand the disease and find potential biomarkers.

In recent years, increasingly rapid advances in the field of medical imaging have taken place, both in access and development of technique. A large number of large-scale multicentre studies have been conducted during the last decade, and the imaging data shared publicly. The availability of these data has opened up opportunities to engineer novel imaging biomarkers and to discover as yet unknown biological characteristics of diseases. It is now well established from a variety of studies that various diseases are associated with structural brain changes that can be shown quantitatively on MR images using anatomical segmentation [18]–[20]. Anatomical segmentation has usually been performed visually by experts to identify and understand abnormalities [21], however due to the increasing amount of data, we are not able to educate new experts rapidly enough to keep pace with the increasing amount of data. In order to support the experts and save valuable time, the past years have seen development of automatic anatomic image segmentation software. Image segmentation software is useful in executing quantitative image analysis and identifying structural abnormalities in various regions in the brain. Image segmentation has shown to be accurate and robust to delineate brain regions automatically [22]. In recent years, we have witnessed a growing academic interest in such software, particularly in the context of seeking potential imaging biomarkers for diagnosing and monitoring neurological diseases.

So far, few studies have examined structural brain changes in PD participants using automatic anatomical segmentation [23]–[26]. Most of these studies have only been carried out with voxel-based methodology, and region-wise quantitative morphometric studies with automatic anatomic image segmentation software have, to my knowledge, not yet been conducted. Moreover, the existing studies on regional brain volume in PD participants, are limited by relatively small sample sizes. In addition, no previous study has been carried out on structural brain changes in PD and epilepsy by comparison. The extent to which epilepsy is associated with Parkinson’s disease remains poorly understood.

1.2 Aim & Outcomes

In the study described in this thesis, I set out to investigate brain region volumes in PD participants in comparison to a healthy cohort, by conducting a region-wise morphometry study with the automatic image segmentation software MAPER. The secondary aim of this study is to shed light on the neuromorphological characteristics that PD and epilepsy have in common.

In particular, in this thesis we will:

- Compare region volumes along the nigrostriatal pathway between PD participants, epilepsy participants and a control group.
- Compare asymmetry indices in regions along the nigrostriatal pathway between PD participants, epilepsy participants and a control group.
- Compare ICV volume between PD, epilepsy participants and controls.
- Compare the difference between ICV and parenchyma volume in PD participants, epilepsy participants and a control group.

1.3 Demarcations

Due to a limited time frame, this master thesis does not encompass all brain regions in detail. I will focus instead on Substantia nigra and connected regions via the nigrostriatal pathway.

In brain morphometry, there are several different methodologies available, such as voxel-based, deformation-based, pattern-based and surface-based morphometry. This thesis is limited to just one methodology, namely region-wise morphometry.

2

Theory

Medical imaging is an extensive subject that encompasses significant parts of image acquisition, processing and analysis. The following chapter provides a brief overview of essential concepts and theories in medical imaging as applied in this thesis.

Section 2.1 gives a brief overview of the physics behind magnetic resonance imaging and how images are acquired. Fundamental definitions and characteristics of an image will be presented in the latter part of section one. Some commonly used processing techniques will be presented in Section 2.2. Section 2.3 and 2.4 will treat the theory behind image registration and segmentation, which are essential concepts in this thesis.

2.1 Data acquisition with MRI

The term *medical image* refers to an image that depicts the insides of a human body and has been acquired using a medical imaging technique (modality)[27]. There has been remarkable progress in medical imaging systems during the past century, which has engendered frequent and worldwide use of the technology. Medical images come in many various shapes and visualise body structures differently. Hence, a modality is chosen for every occasion, depending on the target of interest [27]. Some commonly used modalities are:

- Computed tomography (CT)
- Magnetic resonance imaging (MRI)
- Positron emission tomography (PET)
- Projection radiography
- Ultrasonography

The primary data discussed in this thesis are anatomical brain images acquired from magnetic resonance imaging (MRI) scanners. MRI is characterised by high sensitivity to soft tissue differences (high contrast resolution) and non-ionising radiation, which are the key reasons for choosing MRI over other modalities when examin-

ing the brain [27]. However, MRI has noteworthy drawbacks, including high siting costs, acoustic noise, tissue heating, a risk of claustrophobia in patients / study participants, and long imaging times [27]. We will further investigate the MRI technique, data acquisition, image reconstruction and quality aspects to achieve a more in-depth understanding of the medical images used in this thesis.

2.1.1 The MRI technique

MRI is a rather complex technique based on quantum mechanics, mathematics and classical physics [28]. Considering the extensive theory of MRI, this thesis only accounts for the general concepts.

The most crucial concept in MR imaging is the magnetic properties of the atomic nucleus [29]. Each atom has a nucleus that consists of neutrally charged neutrons and positively charged protons [29]. Each proton in a nucleus continually rotates around its own axis, a property referred to as the *spin* [27]. As the proton is positively charged, the spin will cause a magnetic field. Thus, one can model a proton as a small magnet [29]. However, the magnetic moment of a single proton is undetectable. The *hydrogen atom* is vital in MRI since it has a large magnetic moment and isotopic abundance [27]. Moreover, hydrogen makes up large parts of fat and water, which the human body contains a lot of, and is therefore the main focus for generating MR signals [27].

Usually, the spinning protons are randomly orientated in the body [27], see Figure 2.1a, and a magnetisation is not detectable. During an MRI session, the patient is exposed to a strong magnetic field, B_0 . Magnetic field strength is measured in Tesla (T), and 0.3-4 T are common strengths in MRI scanners [27]. The large magnetic field forces the spinning protons to orientate in parallel and antiparallel direction to the magnetic field [27], see Figure 2.1b. The parallel and antiparallel protons are distributed at two different energy levels due to thermal energy within the sample of protons. At equilibrium, a slight majority of protons exists in the low-energy parallel direction. The strong magnetic field increases the energy separation between the high and low levels of protons and results in a surfeit of protons in the low energy state. The surfeit produces an observable sample of magnetic moments, further called the *net magnetic vector* M_0 , aligned parallel to the magnetic field [27]. In addition to the energy separation, the protons' spin axes start to rotate around the magnetic field axis [27], see Figure 2.1c, when they are exposed to the strong magnetic field B_0 . The spin around the magnetic field axis is referred to as *precession*. Precession occurs at an angular frequency, f , proportional to the magnetic field strength B_0 [27]. The *Larmor equation* describes the relationship between the angular frequency and the magnetic field strength B_0 :

$$f = \gamma * B_0 \tag{2.1}$$

where γ is the gyromagnetic ratio [27].

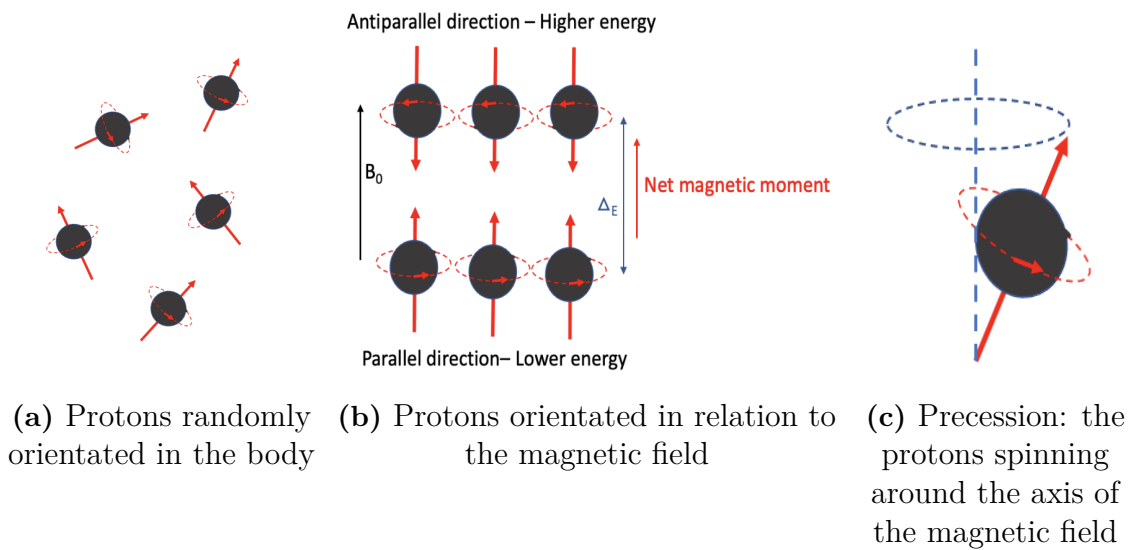


Figure 2.1: The figure visualises protons with and without exposure to a strong magnetic field

Signal induction

Initially, the net magnetisation vector, M_0 , is at equilibrium as seen in Figure 2.2a [27]. The net magnetisation vector is weak, and it is not possible to localise it due to the strong magnetic field [29]. To induce an MRI signal which the scanner can detect, a radiofrequency (RF) pulse, tuned to the Larmor frequency, is transmitted from the RF coils within the scanner [27]. When the RF pulse's frequency is equal to the protons' Larmor frequency, the magnetic moments resonate and the imaged object absorbs energy from the pulse. The absorbed energy corresponds to a transition of protons in the low-energy level (parallel direction) to the high-energy level (antiparallel direction) [27]. The RF pulse causes a flip to the net magnetisation vector with a specific flip angle α [27], see Figure 2.2b. When the magnetic moments are synchronised, they reinforce each other and produce a strong magnetic moment [29]. The greatest magnetic moment is obtained when the net magnetisation vector is perpendicular to the magnetic field, strictly speaking when the flip angle is $\alpha = 90$ [29]. The large magnetic moment in the transverse direction to the magnetic field B_0 induces an MRI signal that the RF coils can detect [29].

Relaxation

The net magnetisation vector returns to equilibrium when the RF pulse is switched off; this is referred to as *relaxation*, illustrated in Figure 2.3. The restoration of the net magnetisation vector to equilibrium results in energy emission from the protons that flip from the high energy level to the low energy level. *T1 relaxation* refers to the time it takes for the magnetisation vector to return from the Y-axis to the Z-axis, proportional to a specific *T1 time constant*, see Figure 2.3a. The *T1 time constant* is distinct for each tissue category. The *T2 relaxation* is the time it takes for the magnetisation vector to get out of phase; in other words, the time in which the x-y

direction component disappears (see Figure 2.3b). Like the *T1 time constant*, there is also a specific *T2 time constant* for each specific tissue. The *T1 relaxation* and *T2 relaxation* take place simultaneously but take different amounts of time. Table 2.1 gives some examples of *T1 constants* and *T2 constants* for some tissues. [27]

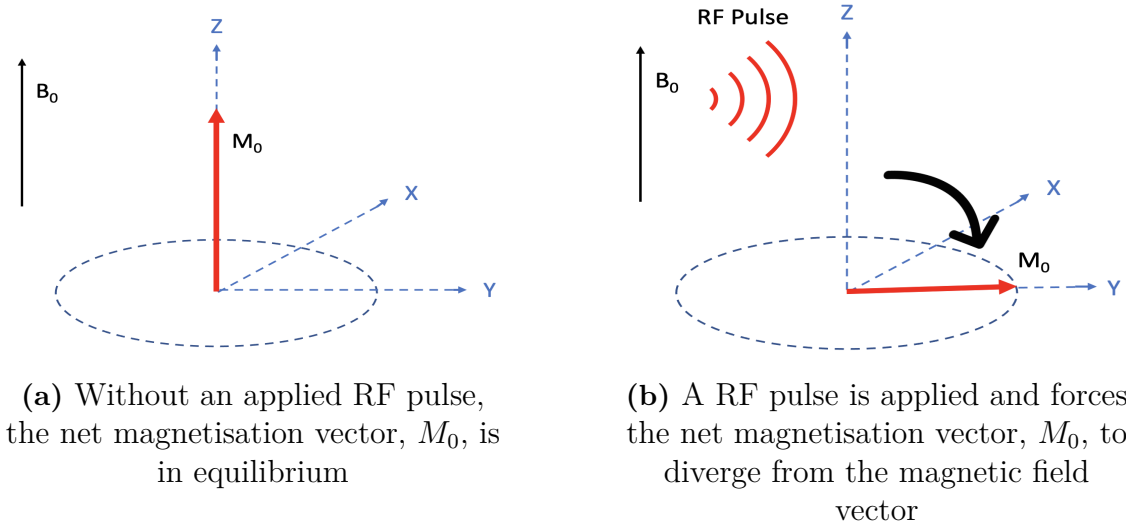


Figure 2.2: The figure visualises what happens to the net magnetisation vector, M_0 , prior to and after applying the RF pulse

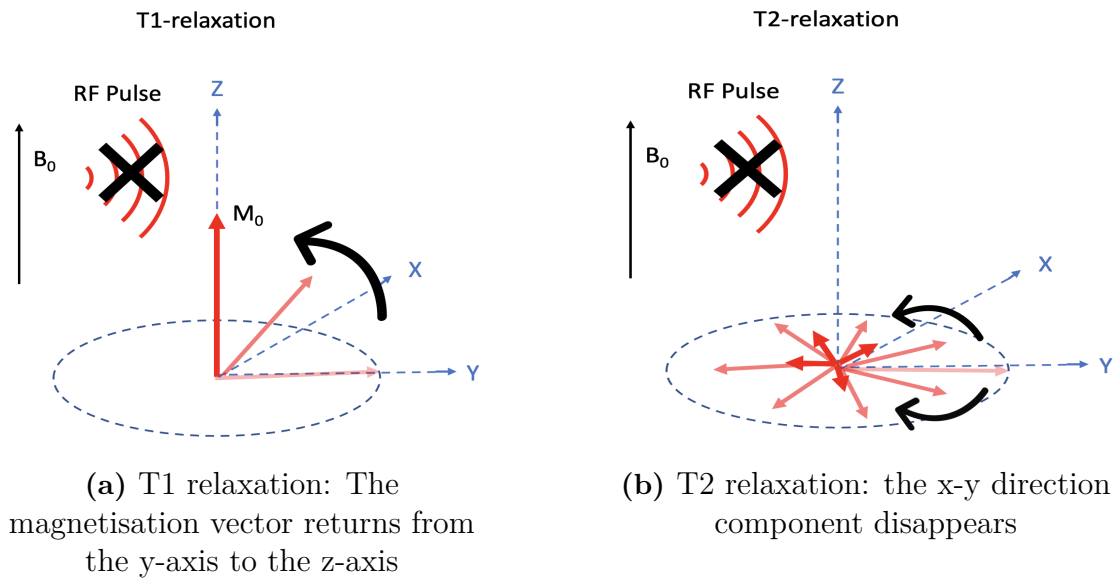


Figure 2.3: he figure visualises the two relaxation phenomena T1 and T2 relaxation, which takes place when the RF pulse is switched off

2.1.2 Acquisition parameters

Emphasising the differences between T1 and T2 relaxation time constants and proton density of the tissue is a fundamental aspect that determines the contrast in

Table 2.1: Table of T1 and T2 relaxation times for various tissues with a magnetic field strength of 1.5 T [27].

TISSUE	T1 (ms)	T2 (ms)
Fat	260	80
Liver	500	40
Muscle	870	45
White matter	780	90
Gray matter	900	100
Cerebrospinal fluid	2,400	160

images. Images reflect all of the three characteristic properties; however, the acquisition is usually parametrised for one of the characteristics to appear more distinct. Various parameters are set during the MRI session to achieve the desired weighted image. Two of the main parameters are TR and TE . During an MRI session, the volume of interest must be stimulated several times to produce an image. TR is the time between two stimuli (excitation of the same volume), and TE is the time between the excitation and the measurement of the image signal. Together with the resolution and FOV, TR and TE significantly impact the quality of the data. Further aspects of image quality are dealt with in Section 2.1.5.

The RF pulses must be applied in sequences together with the choice of TR , TE and *flip angle* to achieve a contrast-weighted image. Three pulse sequences are commonly applied: spin echo (SE), inversion recovery (IR), and gradient echo (GE). We will not go further into the meaning of each pulse sequence. Figure 2.4 shows three different weighted images produced with a SE pulse sequence, together with the range of recommended parameter values in order to archive the weighted images. [27]

2.1.3 Data acquisition

An important aspect of MR image acquisition is to localise the source of the MR signals. The MRI scanner uses gradients to isolate the source of the signal to localise the specific magnetic moments. There are three gradient coils in an MRI scanner, which creates small magnetic field gradients in three directions when the coils are turned on, see Figure 2.5. These gradients are called *slice select gradient*, *frequency encode gradient* and *phase encode gradient*.

The spatial localisation is performed in three steps, as seen in the upper part of Figure 2.6, but can be applied variously depending on the sequence. Firstly, a specific slice of the body is selected by stimulating a position in the *slice select gradient*. The phase and frequency encode coils are then turned on and off in the second and third steps to create variations in the magnetic moments' phase and frequency in each voxel of the slice. The scanner then collects the position-dependent variations of the protons precessional frequency. The process continues until each element in the slice is determined with a specific phase and frequency. The signals

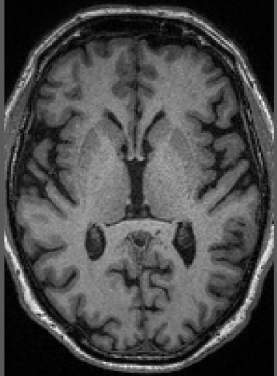
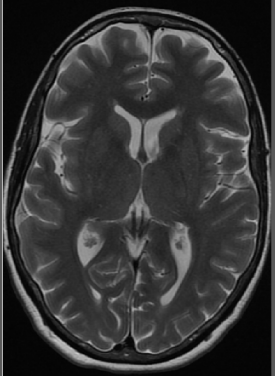
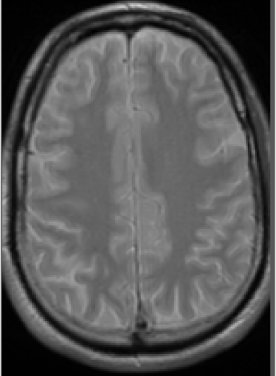
Image			
Weightning:	T1	T2	PD
TR	Short 300-600 ms	Long. 2000 ms	Long. 1000-3000 ms
TE	Short 10-30 ms	Long. 90-140 ms	Short. 15 ms
Example:	Water appears dark and fat appears bright.	Water appears bright, and the fat appears less bright.	The fat appears bright, and the water appears less bright.

Figure 2.4: Comparison between T1, T2 and Proton Density weighted image, produced with a spin echo sequence [30]

are encoded into the so-called K-space (the frequency domain) as complex numbers. An overview of the acquisition procedure can be seen in the lower part of Figure 2.6. [27]

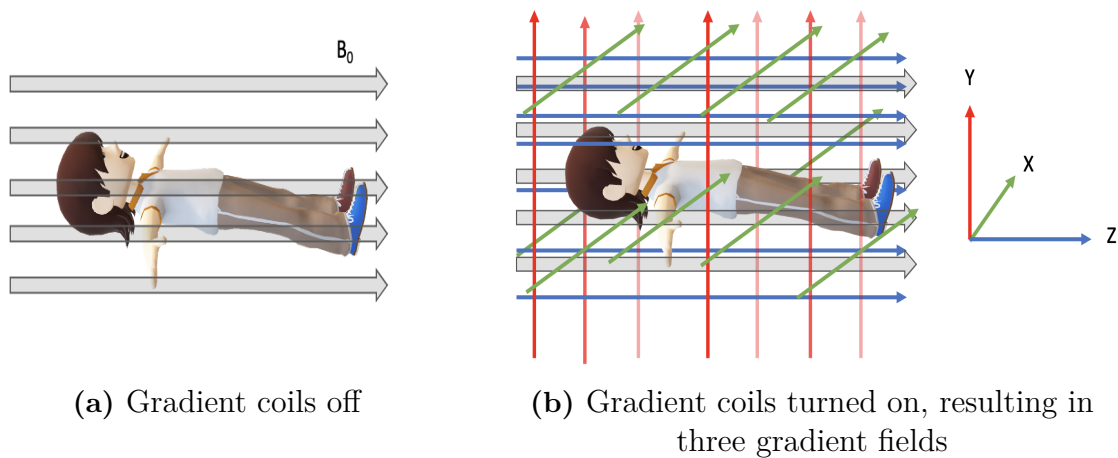


Figure 2.5: Effects of turning on the gradient coils

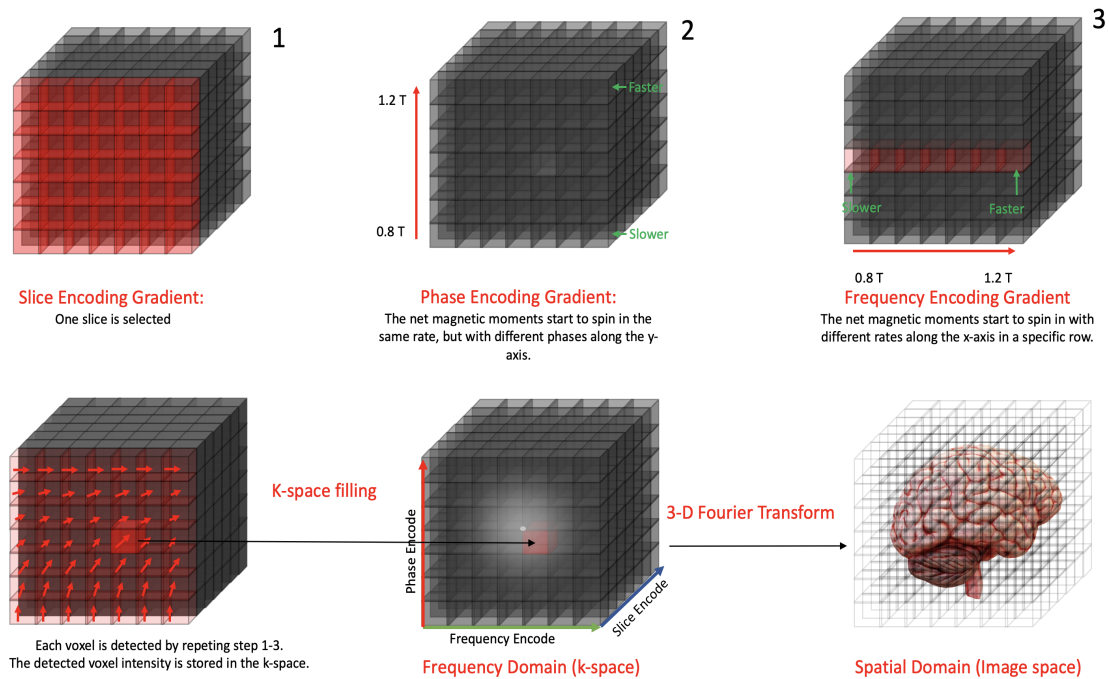


Figure 2.6: Data acquisition

2.1.4 Image reconstruction

The K-space is transformed from analogue (continuous) signals into digital (discrete) signals $x(t_1, t_2 \implies x[n_1, n_2])$, by the use of the Fourier transform. The Fourier transform turns each frequency and phase into a specific intensity value in a matrix. The output from the digitisation is a mathematical matrix with discrete values indicating intensities in each position. The image reconstruction process is illustrated in the bottom-right part of Figure 2.6.[27]

Recall that the output from the MRI scanner is a digital image, which implies a matrix with discrete values. A 2D image is a matrix in two dimensions, and a 3D image is a matrix with three dimensions. Each matrix element is called a pixel or a voxel (volume pixel in the case of a 3D image), where each pixel (or voxel) represents an intensity value in the greyscale. The greyscale is a scale from black to white and shades of grey in between. An intensity value of zero is equal to black, while the highest number in the scale represents white. The size of the greyscale, intensity levels L , is determined as an integer to the power of two $L = 2^k$, where k is the number of bits. For example, a 256-level image is $L = 2^8 = 256$ and is called an 8-bit image. An MR image usually has $L = 2^{12}$ intensity levels, called 12-bit image [27].

2.1.5 MR image quality

Image quality in MRI is a trade-off between signal-to-noise ratio (SNR), scan speed and spatial resolution [27]. Increasing one of the factors entails reducing the other two factors. The choice of parameters controls the image quality during the MRI

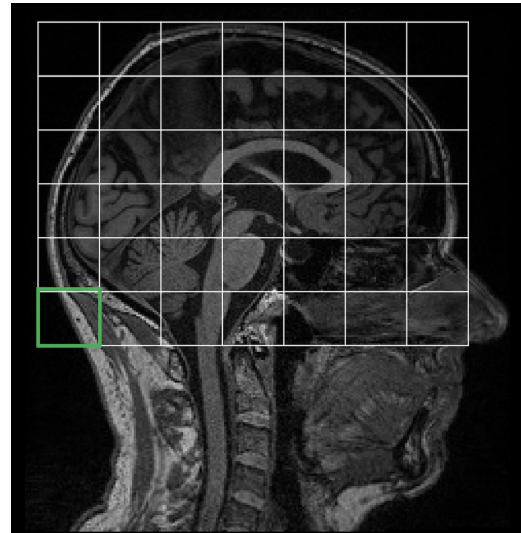
session, for example, TR, TE, matrix size, slice thickness and FOV [27]. Some of the quality characteristics will be presented below.

Spatial resolution

The ability of an imaging system to show details in an image is called spatial resolution. High spatial resolution implies a good ability to show details. The spatial resolution is highly determined from the choice of field of view (FOV). The FOV determines the pixel size, where common amount of pixels are 128, 256, 512 or 1024 in all directions. The size of the individual pixel determines the resolution, and a pixel edge length is usually between 0.5 and 1 mm. For example, a 250 mm FOV with matrix size 256×256 has a pixel size of approximately 1 mm, implying a resolution of 1 mm ($250/256 \approx 1$). [27]



(a) Field of view (FOV): area being imaged



(b) Pixel: the smallest addressable element in an image. The size of the individual pixels determines the resolution

Figure 2.7: Difference between field of view and pixel

Signal-to-noise ratio (SNR)

The signal-to-noise ratio is defined as the fraction between the power of the signal and the power of the noise. The SNR of the MR image is dependent on several variables [27]. The SNR for two-dimensional image acquisition is:

$$\text{SNR} \propto I \times \text{voxel}_{x,y,z} \times \frac{\sqrt{\text{NEX}}}{\sqrt{\text{BW}}} \times f(\text{QF}) \times f(\text{B}) \times f(\text{slice gap}) \times f(\text{reconstruction}) \quad (2.2)$$

where I is the intrinsic signal, $\text{voxel}_{x,y,z}$ is the voxel volume, NEX is the number of excitations, BW is the frequency bandwidth of the RF receiver, $f(\text{B})$ is the function

of the magnetic field strength, $f(\text{slice gap})$ is the function of interslice gap effects, $f(\text{QF})$ is the function of the coil quality factor parameter, and $f(\text{reconstruction})$ is the function of the reconstruction algorithm. [27]

2.1.6 MR image artefacts

Artefacts are characteristics or features of an image that do not represent the depicted object. Artefacts may occur for various reasons. Some common artefacts are motion artefacts, wraparound artefacts, and intensity non-uniformity, see Figure 2.8 [27].

Motion artefacts

Due to the relatively long acquisition time during an MRI session, MR images frequently show motion artefacts. They arise from the patient's voluntary and involuntary movements. In addition, blood flow and CSF flow also have an impact. Motion artefacts can appear as ringing in the image, see Figure 2.8a. [27]

Wraparound artefacts

An example of a wraparound artefact is shown in figure 2.8b, where part of the anatomy is depicted at the opposite side of the image. Wraparound artefacts occur due to mismapping of anatomy and can be caused by nonlinear gradients or under-sampling of the k-space (aliasing). To avoid wraparound artefacts due to aliasing, the sampling frequency, f_s , should be chosen according to the Nyquist–Shannon sampling theorem [27]:

$$f_s \geq 2f_{\text{MAX}} \quad (2.3)$$

which implies that the minimum sampling frequency should be at least twice as large as the maximum frequency in the signal. [27]

Intensity non-uniformity

Intensity non-uniformity is a common source of artefact, where a given class of tissue has variations in intensity when it should be constant throughout the image.

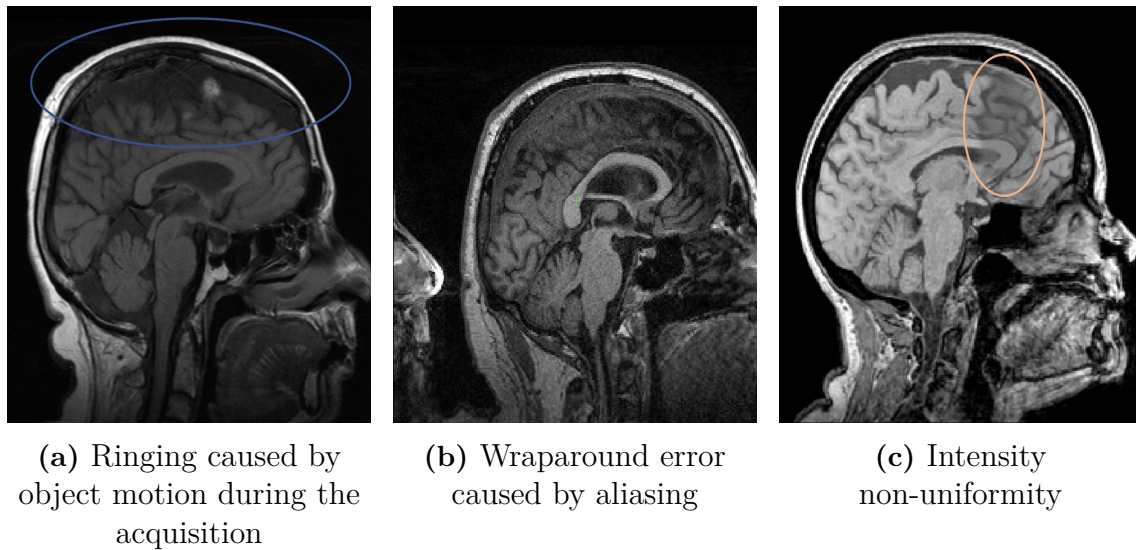


Figure 2.8: Three examples of common artefacts that may occur in an MR image

2.2 Medical image preprocessing

Raw images as generated by MR scanners are affected by acquisition-related artefacts and noise. Furthermore, the size and resolution of the raw data might not be optimal for the intended analysis process. Thus, raw MR images usually need to be preprocessed before using the data for further processing, such as registration and segmentation. The preprocessing takes place in so-called preprocessing pipelines and differs between applications. Some preprocessing steps in the pipelines might include:

- Intensity non-uniformity correction
- Resampling and spatial interpolation
- Geometric distortion correction
- Noise reduction
- Motion correction
- Foreground/background segmentation (e.g. brain extraction)

In this section, we will describe some of the common techniques that can be applied in the preprocessing part of analysing structural MR images.

2.2.1 Intensity non-uniformity correction

Field bias is a common source of low-frequency noise. As noted previously in Section 2.1.6, field bias causes the same type of tissue to have varying signal intensity across an image. While moderate amounts of field bias do not affect image interpretation

by humans, intensity-based image segmentation algorithms can fail unless correction for the inhomogeneity is applied. A popular approach to inhomogeneity correction has been implemented as a software program called N3 software and its successor, N4 [31], [32].

N3 is an iterative algorithm that does not require any prior knowledge from the image. The algorithm seeks the smooth multiplicative field that maximises the high-frequency content of the tissue intensity distribution. [31]

The N4 algorithm improves upon N3 by replacing the B-spline smoothing strategy. In addition, the iterative optimisation scheme has been enhanced [32].

2.2.2 Brain extraction

Head images acquired from an MRI scanner contain the skull and other non-brain tissue such as scalp, face, neck, and eyeballs [33]. To analyse the brain itself, it is preferable to apply a preprocessing step that distinguishes between such background objects and the foreground (brain) [33]. The process is called brain extraction or skull stripping. Several such algorithms are available [34]. They fall into five categories: mathematical morphology-based methods, intensity-based methods, deformable surface-based methods, atlas-based methods, and hybrid methods [34]. There is no algorithm that performs best on all occasions [34].

2.2.3 Reorientation

There are several file formats for storing MR images, such as DICOM and NIfTI. The choice of file format is important to keep tight control on the spatial representation of the imaged object to retain consistency across the steps of the processing pipeline. The NIfTI format (short for Neuroimaging Informatics Technology Initiative) has been designed specifically for neuroimages to give the user this kind of control. Therefore it is desirable to convert images to NIfTI early on if they have been supplied in another format.

Moreover, independent of the file format, the information in the header of the image file, such as where the origin is placed, can vary across the images. To ensure that the images used in a study are orientated in the same way, we wish to re-orientate the images. A reorientation tool can be applied in the preprocessing pipeline to arrange the data to retain consistency between the images. [35]

2.2.4 Spatial interpolation

In the context of image processing, an image often needs to be re-sampled into a new image space through transformations to achieve, for example, a different resolution or size. Interpolation is a way of estimating unknown pixel values by using a set of known values to determine the new image pixels after transformation. Some commonly used interpolation methods are:

- Nearest neighbour
- Truncated and windowed sinc
- Linear
- Quadratic
- B-spline
- Gaussian

[36].

2.2.5 Noise reduction

Undesirable noise sometimes appears in MRI images during the acquisition process, causing reduced quality and SNR. Common types of noise in medical images are Gaussian, Poisson, Blurred, Speckle and salt-and-pepper noise. Sometimes, noise reduction is crucial to apply to increase the image's quality and accuracy for further processing steps. To reduce the noise in MRI images, there are several linear and non-linear methods available, which are applied depending on the noise type. Commonly applied filtering methods are non-local means, Median Filter, Gaussian filter. [37]

2.3 Medical image registration

Image registration is the process of aligning a source image to a target image, by finding corresponding anatomical locations in the two images [38]. The process of image registration involves finding a transformation between the images that minimises the difference between them [39]. Image registration allows for several design options

1. A transformation model - defines the geometric transformation between a target and source image.
2. Registration basis - measures the degree of alignment between the source and target image.

In the subsections that follows, we will briefly explain the design options.

2.3.1 Transformation model

In 3D image registration, we seek to find a transformation $\mathbf{T} : (x, y, z) \mapsto (x', y', z')$ which maps every point in the source image to a point in the target image. There are several available transformations, distinguished by the number of degrees of freedom (DoF). Simple rigid transformation allows for translation and rotation in

all spatial directions (up to 6 DoF); affine transformation additionally allows for rotation and scaling (up to 12 DoF). More complex transformations are termed deformable, elastic, or fluid, with principally unlimited DoF.

In medical imaging, the images are typically aligned using a rigid and/or affine transformation, followed by a nonlinear local transformation. The following describes transformation models relevant for the study presented in this thesis.

Rigid transformation

A rigid transformation allows alignment for translation and rotation. The rigid transformation in the 3D case allows for six DoFs: three rotations and three translations [38].

$$\mathbf{T}_{\text{rigid}}(x, y, z) = \begin{pmatrix} x' \\ y' \\ z' \\ 1 \end{pmatrix} = \begin{pmatrix} r_{11} & r_{12} & r_{13} & t_x \\ r_{21} & r_{22} & r_{23} & t_y \\ r_{31} & r_{32} & r_{33} & t_z \\ 0 & 0 & 0 & 1 \end{pmatrix} \begin{pmatrix} x \\ y \\ z \\ 1 \end{pmatrix}. \quad (2.4)$$

Affine transformation

In addition to rotation and translation, affine transformation also enables scaling and shearing. The affine transformation has up to twelve DoF. Shearing (in the x-y plane) can be expressed as:

$$\mathbf{T}_{\text{shear}}^{xy} = \begin{pmatrix} 1 & 0 & h_x & 0 \\ 0 & 1 & h_y & 0 \\ 0 & 0 & 1 & 0 \\ 0 & 0 & 0 & 1 \end{pmatrix} \quad (2.5)$$

and scaling as:

$$\mathbf{T}_{\text{scale}} = \begin{pmatrix} s_x & 0 & 0 & 0 \\ 0 & s_y & 0 & 0 \\ 0 & 0 & s_z & 0 \\ 0 & 0 & 0 & 1 \end{pmatrix}. \quad (2.6)$$

By combining rigid transformation with scaling and shearing, we arrive at affine transformation as [38]:

$$\mathbf{T}_{\text{affine}}(x, y, z) = \mathbf{T}_{\text{shear}} \cdot \mathbf{T}_{\text{scale}} \cdot \mathbf{T}_{\text{rigid}} \cdot (x, y, z, 1)^T. \quad (2.7)$$

Non-Rigid transformation

Affine and rigid transformation use a small number of parameters (six or twelve DoF), which is insufficient for more complex mapping that is necessary for applications where significant deformation is expected. Using non-rigid transformations is

a more appropriate option when dealing with complex transformations. Non-rigid transformations are divided into two branches: *parametric non-rigid transformations* or *non-parametric non-rigid transformations*. The *non-parametric non-rigid transformation* describes the deformation at every voxel by a stored dense displacement field. The *parametric non-rigid transformations* transformation models use a set of parameters that is usually much smaller than the number of voxels [38].

In medical imaging processing, free-form deformation is a common option of non-rigid transformation. Sederberg and Parry first proposed free-form deformations in 1986 [40]. free-form deformations with b-splines as subsequently proposed by Rueckert et al. found widespread use [41]. Non-rigid transforms are usually described as a linear combination of basis functions θ_i [38]:

$$\mathbf{T}(x, y, z) = \begin{pmatrix} x' \\ y' \\ z' \\ 1 \end{pmatrix} = \begin{pmatrix} a_{00} & \dots & a_{0n} \\ a_{10} & \dots & a_{1n} \\ a_{20} & \dots & a_{2n} \\ 0 & \dots & 1 \end{pmatrix} \begin{pmatrix} \theta_1(x, y, z) \\ \vdots \\ \theta_n(x, y, z) \\ 1 \end{pmatrix}. \quad (2.8)$$

Commonly used basis functions are Fourier (trigonometric) or wavelet basis functions. An appropriate basis function is chosen considering three aspects: the ability to describe local transformations, smoothness, and simplicity [38].

2.3.2 Registration basis

After choosing an appropriate transformation model, the second step in a registration algorithm is to implement a registration basis. The registration basis measures the degree of alignment between the images and represents the cost function in the optimisation process. The goal is to minimise the cost function by maximising the correspondence between the source and target image. There are two main approaches: Feature-based registration or intensity-based registration.

Feature based registration relies on point-to-point correspondence between images for estimating the transform. The feature-based registration relies on landmarks and is a popular option in computer vision.

Intensity-based similarity measures are more commonly used when dealing with medical images. They measure the degree of shared information of the image intensities. Several similarity measure methods can be used, and we will now present some of the commonly used ones.

Below, we denote the source image as β , which will be transformed to the target image α . The similarity measure, S , measures the correspondence between the target, α , and the transformed image β' . When the similarity measure is maximised, the cost function of the optimisation function is minimised.

Sum of squared differences (SSD)

Sum of Squared Differences (SSD) utilises intensity between the image α and β' . The similarity measure assumes that the difference between the two images has a Gaussian distribution. The SSD are calculated as:

$$S_{SSD}(\alpha, \beta') = \sum_{i=1}^N (\alpha_i - \beta'_i)^2 \quad (2.9)$$

where N is the number of voxels in the overlap between α and β' . [39]

Mutual information measure (MI)

Likewise SSD, the Mutual information measure (MI) also utilises intensity changes between α and β' . In contrast to SSD, MI measure the intensity changes by the images joint histogram. Moreover, the aim in this approach is to find a transformation that maximises the mutual information:

$$MI(\alpha, \beta') = H(\alpha) + H(\beta') - H(\alpha, \beta') \quad (2.10)$$

where H stand for entropy. [39]

Cross correlation (CC)

Cross Correlation (CC) is a good option of measure when one can assume that there are a linear relationship between the two intensities [38]. CC is estimated as:

$$CC(\alpha, \beta') = \frac{\sum_i (\alpha_i - \bar{\alpha})(\beta'_i - \bar{\beta}')}{\sqrt{\sum_i (\alpha_i - \bar{\alpha})^2 \sum_i (\beta'_i - \bar{\beta}')^2}} \quad (2.11)$$

where $\bar{\alpha}$ and $\bar{\beta}'$ correspond to average voxel intensities in α and β' [39].

2.4 Medical image segmentation

Image segmentation is a frequently used image processing method that implies dividing an image into specific regions of interest [42]. More specifically, when dividing an image, the image's pixels are assigned to different predefined classes. The segmentation output is an image labeling, where each pixel has been assigned to a specific label. In medical imaging, the segmentation could, for example, separate an image of the abdomen into its' constituent parts like liver, kidney, spleen, pancreas etc. In this thesis, we will divide the brain into different regions like hippocampus, cerebellum, substantia nigra, etc. There are several segmentation techniques that could be applied for different applications.

Several segmentation techniques are available, among them threshold-, edge-, clustering-, and atlas-based methods. Some of the segmentation methods can be used with Convolutional neural network (CNN). However, a drawback with CNN is that we need many images to train a good network, especially when handling 3D medical images. When handling with medical images, the data often comes with a high cost due to acquisition time and expertise time to manually segment the images. A more appropriate solution is, therefore, to use multi-atlas segmentation. In the following section, we will turn the light on multi-atlas segmentation, which is the method used in this thesis.

2.4.1 Multi-atlas segmentation

To begin with, an atlas is an image together with a, usually manual, segmentation. In other words, an atlas is an image with known information about the specific anatomic which have been produced by an expert. By aligning the atlas image to a target image, which we have no information about, the purpose is to transfer the known knowledge to the target image. "Multi" implies that we register and propagates several atlases, instead of a single atlas, to the target image. Multi-atlas segmentation is more robust for anatomical variations and appears more robust than the single-based method.

The steps of multi-atlas segmentation can be summarised as:

1. Image registration - All atlases are registered with the target image.
2. Label propagation - The labellings are transferred and automatically assigned to the unlabelled target image.
3. Label fusion - all transferred labellings are combined to one segmentation using majority voting for each pixel.
4. Evaluation of the result.

Label propagation in combination with label fusion have shown high accuracy when segment a large amount of brain structures in MR images by Heckemann et al. [43] An visual explanation of the multi-atlas based segmentation are shown in Figure 2.9.

Image registration and label propagation

The target is registered with each of the atlases, as described in Section 2.3. The registered labellings are later transferred and propagated to the target image.

Label fusion

Label fusion is the process of combining all propagated labellings into one estimated segmentation of the target image. The simplest way of doing this is through majority voting which implies that one assigns the label with the highest number of votes.

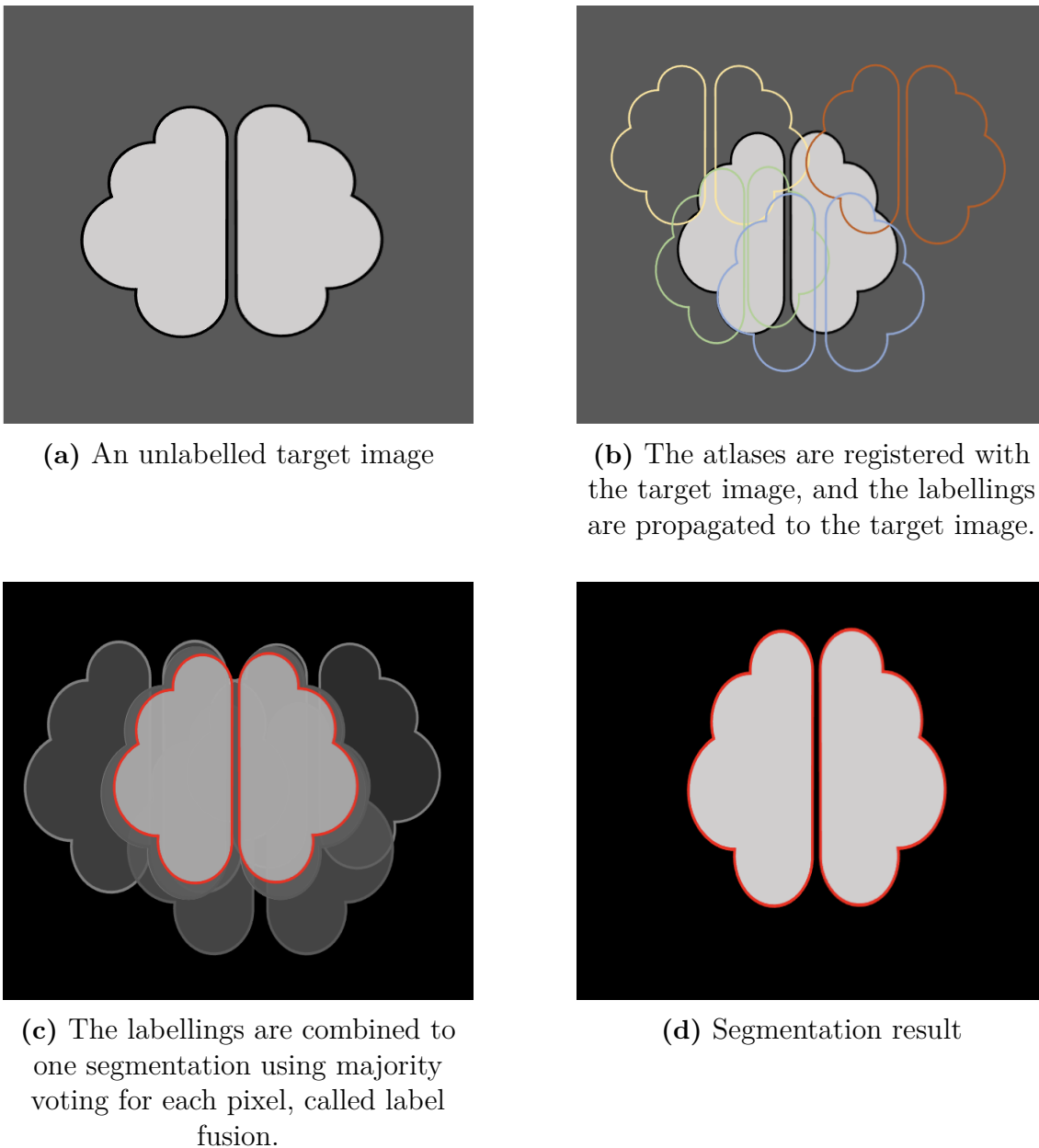


Figure 2.9: The figure visualises the process of multi-atlas based segmentation.

The label fusion can be described as a delta function, δ , which returns 1 if the argument is true and zero otherwise:

$$\hat{F}(x) = \arg \max_{l \in \{0,1\}} \left\{ \sum_{i \in A} \delta(L_i(x) = l) \right\}. \quad (2.12)$$

where the segmentation label on each target voxel is denoted $\hat{F}(x)$, each atlas label is denoted as L_i and A is the set of atlases. [44]

The advantage of combining multiple atlases by majority voting is that it tends to correct errors made by an individual atlases. However, sometimes more advanced

fusion strategies is needed to compensate for specific error patterns, such as *Weighted voting* approaches or *Probabilistic* approaches. [44]

Evaluation of the result

Once we have received an target label map, we can evaluate the performance of the segmentation by using different similarity measures. One of the popular once is the dice coefficient and measures the overlap between the estimated target label map and the "true" label map:

$$S_{\text{DICE}} = \frac{2|\mathcal{L} \cap \mathcal{L}_{\text{GT}}|}{|\mathcal{L}| + |\mathcal{L}_{\text{GT}}|}. \quad (2.13)$$

where \mathcal{L} is the estimated target label map and \mathcal{L}_{GT} is the ground truth label map.

Another popular measure is the Jaccard index:

$$S_{\text{JACCARD}} = \frac{|\mathcal{L} \cap \mathcal{L}_{\text{GT}}|}{|\mathcal{L} \cup \mathcal{L}_{\text{GT}}|}. \quad (2.14)$$

where \mathcal{L} is the estimated target label map and \mathcal{L}_{GT} is the ground truth label map.

3

Materials and methods

The methodological approach taken in this study is region-wise morphometry using atlas-based image segmentation on a cross-section of participants in a multi-centre study on PD. 958 MR images were obtained from the PPMI database, preprocessed and segmented using image analysis software as MAPER and Pinfram.

The first section (3.1) gives an overview of the data used in this thesis. Section 3.2 is concerned with the study design employed for this study. Section 3.3 provides information about the software installation, while Section 3.4, 3.5 and 3.6 examine the preprocessing and segmentation processes. The last section (3.7) outlines the methodological approach taken in the statistical evaluation.

3.1 MR data

Study data used in this thesis were obtained from the Parkinson’s Progression Markers Initiative (PPMI) [16], an observational, international, multi-center study on PD, with more than 1,400 participants recruited from 33 clinical sites in 11 countries [16]. The full repository of PPMI images was accessed in January 2021, and images and metadata were retrieved during spring 2021. Data from six different PPMI cohorts were obtained:

Control (C): Control participants without PD who are 30 years or older and who do not have a first degree blood relative with PD.

De novo PD (PD): Participants with a recent (two years or less) diagnosis of PD who are not taking PD medications.

Subjects showing evidence of a dopaminergic deficit (SWEDD): Participants consented as PD participants who have DaT scans that do not show evidence of a dopaminergic deficit.

Prodromal (Pr): Participants without PD who have a diagnosis of hyposmia or REM sleep behaviour disorder.

GenCohort PD (GenPD): Participants with PD who have a genetic mutation in LRRK2, GBA, or SNCA.

GenCohort Unaff (GenUn): Participants without PD who have a genetic mutation in LRRK2, GBA, or SNCA.

The study inclusion criteria are documented on *ppmi-info.org*.

To identify participants relevant for the study presented here, I searched for all available T1-weighted baseline and screening images within the six cohorts. The search returned 1179 images from 961 participants. If more than one image was returned for a participant, one of them was selected at random for inclusion. The remaining 961 images were reviewed to determine if they were directly acquired in 3D or not. Images that were not 3D acquisitions (62/961) were replaced by a previously deselected image, if the latter was a 3D acquisition. Three images could not be identified as either 3D or 2D images. Replacements for these were not available from the database, therefore the three corresponding participants were excluded. After this, 958 participants and 958 remained for inclusion.

To identify the subset of participants with epilepsy or a history of epileptic seizures, the medical history of the included participants was reviewed. An additional search in the medication history did not help to identify additional participants with epilepsy. Instead, two questionnaires, REM Sleep Disorder Questionnaire and FOUND Self-Reported Dx, was found in the study metadata of PPMI where one of the questions in the questionnaires was if the patient has had a medical history of epilepsy. Sixteen participants answered that they have had epilepsy in one of the two questionnaires and were marked as epilepsy participants in this study. An overview of the study data used in this thesis is shown in Table 3.1.

Table 3.1: Distribution of cohorts, gender and epilepsy participants within the cohort groups.

	C	PD	SWEDD	GenPD	GenUn	Pr	Total
Female	65	139	21	51	106	10	392
Male	113	254	40	54	67	38	566
E*	(1)	(5)	(2)	(2)	(2)	(4)	(16)
Total	178	393	61	105	173	48	958

Note: E* = Epilepsy participants included in the cohorts.

The MRI data used in this thesis consisted of T1-weighted 3D or 2D MRI images, which were acquired by PPMI according to a protocol on the project web site *ppmi-info.org/*. The 3D T1-weighted images needed to have a slice thickness of no less than 1.5 mm with no interslice gap to be included in this work. Other parameters such as FOV, voxel size, TR and TE were set according to manufacturer recommendations for the specific scanner and were therefore not equal between the selected images.

3.2 Study design

Considering the number of cohorts and areas we wanted to investigate in this study, we could not state hypotheses for each specific test in advance, especially since we

did not have reasons to make assumptions about all data. Instead, we decided to utilise a split-group hypothesis generation and testing design to both generate and test hypotheses on the same data. I randomly divided the cohorts into two parts; one exploration group and one test group.

3.3 High performance computing cluster

This study makes use of a cluster computing resource, Tetralith, provided by the Swedish National Infrastructure for Computing (SNIC), into which I uploaded all MR data and installed the necessary software (in collaboration with my supervisor). The supervisor simultaneously updated the software used in this thesis, and my principal part in the installation was to pilot testing the new versions of the software and report faults to the supervisor. The cluster resource supported the large scale computation and data storage. The allocation provided for this project was a middle compute allocation in Tetralith, together with a small storage resource in Centre Storage. More information on Tetralith can be found at nsc.liu.se/systems/tetralith.

3.4 Preprocessing

The images obtained from PPMI consisted of images as provided by the scanners and converted to NIfTI format. They needed preprocessing to meet the requirements of MAPER. Initially, the images were preprocessed for B1 nonuniformity correction using the N4ITKBiasFieldCorrection module from Slicer (slicer.org). The N4ITKBiasFieldCorrection module removed field inhomogeneity artefacts from the images by using the N4 bias field correction algorithm, proposed by Tustison et al. [32]. Secondly, the image origin was set to the grid centre using the edit-image module from MIRTk [45] (github.com/BioMedIA/MIRTk).

3.5 Brain extraction with Pincram

The next required preprocessing step before introducing region-wise segmentation with MAPER involves brain extraction, a method to create a brain mask where the brain voxels are separated from non-brain tissue and background voxels using Pincram software [46]. The Pincram algorithm procedure, shown in figure 3.1, is repeated three times in order to optimise an appropriate brain mask. The brain boundary optimisation ranges from coarse to more refine estimation along with three refinement levels. A specific registration method is adopted at each refinement level: first rigid, second affine, and last non-linear image registration. More information on Pincram can be found at github.com/soundray/pincram.

Pincram generates three outputs: a parenchyma mask, an intracranial volume (ICV) mask and a file with the success indices. The ICV mask, containing the parenchyma plus internal cerebrospinal fluid, is the output from the first iteration. The last iteration generates a parenchyma mask, a mask containing the functional tissue in

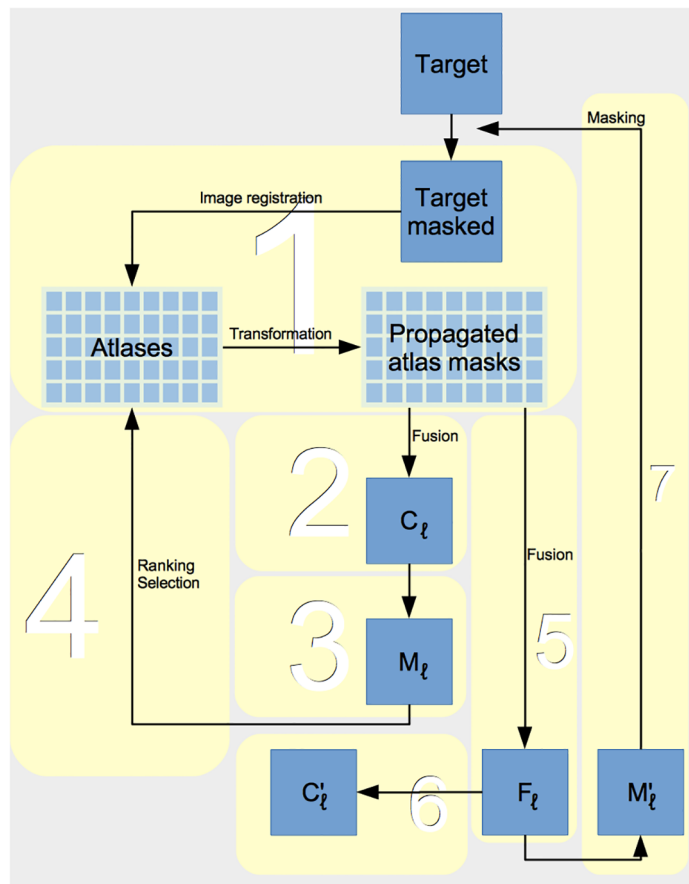


Figure 3.1: A schematic overview of the Pinfram algorithm, where M'_ℓ is the output from the each iteration [46]

the brain. A visualisation of an ICV mask from the first iteration, compared with a parenchyma mask from the last iteration, can be seen in figure 3.2. [46]

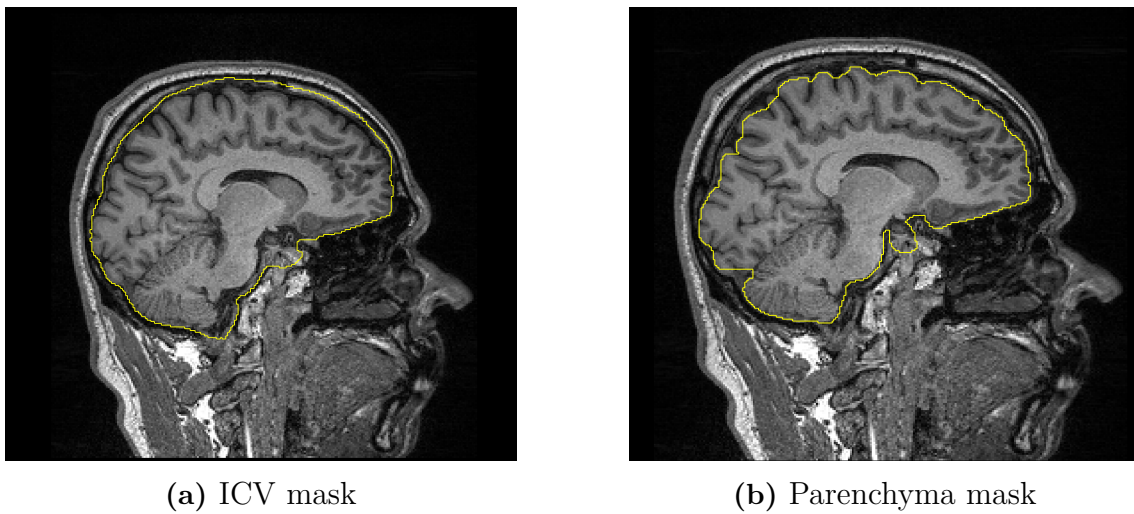


Figure 3.2: Pinfram output visualised with MIRTk Viewer: 3.2a the ICV mask from the first iteration and 3.2b the parenchyma mask from the last iteration

3.5.1 Atlas

Atlas data required for Pinfram were obtained from the publicly available IXI repository of MR images (*brain-development.org*) [47] and consisted of data from 575 healthy, adult subjects.

The quality of the Pinfram masks was confirmed by statistical and visual analysis. The statistical analysis was achieved utilising the success index found in the Pinfram output, a Jaccard coefficient that expresses the agreement between the prefinal and final mask output and thus quantifies convergence. Initially, a sample of 100 segmentations was randomly selected to be visually evaluated by investigating apparent differences from the actual brain anatomies. The visualisation was performed using MIRTk Viewer, an open-source software developed for visualisation of brain images and segmentations in three planes, available for download at *github.com/MIRTk/Viewer*. The quality evaluation showed that the segmentations were insufficient in many cases. The insufficient result might be related to the fact that the study participants in this thesis are of an older population (mean age: 61.8) compared to the atlas set and suffers from atrophy to a larger extent than young adults. Therefore, it was decided to create a customised atlas for the study.

In order to create a new atlas, over 100 of the segmentations were rated visually with MIRTk Viewer. Segmentations with a high quality rating (appearing correct visually) were selected to create the new atlas. The new atlas consisted of 86 segmentations gathered from the study participants and the IXI dataset. The new atlas was tested on 100 of the study participants and evaluated both statistically and visually. The new atlas yielded a better performance on the study participants than the IXI atlas, and it was chosen to continue with the preprocessing using the new atlas for the entire study collection.

3.6 Multi-atlas segmentation with MAPER

Following preprocessing all images with Pinfram, image segmentation was performed with the software MAPER, Multi-atlas segmentation with enhanced registration. MAPER is an improved software developed by Heckemann et al. 2010, based on the former proposal on multi-atlas based segmentation [43], and has been described and validated in [22]. MAPER addressed shortcomings of MR brain image segmentation software available at the time (low robustness, lack of accuracy, necessity to obtain reference (atlas) data from the same scanner as the target images) by introducing tissue classification information into the image registration process. MAPER was the first automatic whole-brain multi-region segmentation method that has been shown to generate robust results in subjects with advanced neurodegenerative disease as well as healthy or ageing subjects [22].

MAPER is open-source software, available for download at *github.com/soundray*. In contrast to the approach presented in [22], the implementation of MAPER used in this thesis relies on software tools sourced from MIRTk and Nifty-seg. Using MAPER, each target image is aligned to each of the atlas images with image regis-

tration. The image registration process in MAPER is summarised in Table 3.2. The steps are performed for each combination of a target image and the atlas images, resulting in 30 segmentations for each target. Following the registration steps, the generated segmentations are combined using vote-rule decision fusion resulting in one optimised whole-brain segmentation for each target image. The label output from MAPER was later processed to determine the volumes of 95 anatomical regions. A visualisation of a MAPER segmentation, visualised using MIRTk Viewer, are shown in Figure 3.3

Table 3.2: Overview of the MAPER steps for generating an individual segmentation

Step	Type	Level	Image data	Similarity index	Toolkit	Tool
1	Global	rigid, affine, coarse	mstprob	CC	MIRTk	register
2	Detailed	nonrigid 10, 5, 2.5	T1 signal	NMI	MIRTk	register
3	Transform	nonrigid 2.5	atlas labels	n/a	MIRTk	transform- image

mstprob: multi-spectral tissue probability map

CC: cross correlation

NMI: normalised mutual information

3.6.1 The Hammers atlas

Atlas data required for MAPER were obtained from the Hammers Atlas Database [47], and consisted of 30 T1-weighted 3D MR images from 30 healthy adults, with 95 expert-delineated anatomical regions of the brain.

3.6.2 Measures of segmentation success

The individual region segmentations from MAPER were assessed by using a level of agreement ratio between each subject segmentation and each of the 30 atlas segmentations. Segmentations contributing to the 100 lowest agreement ratios, and some of the maximum agreement ratios, were visually reviewed with MIRTk Viewer.

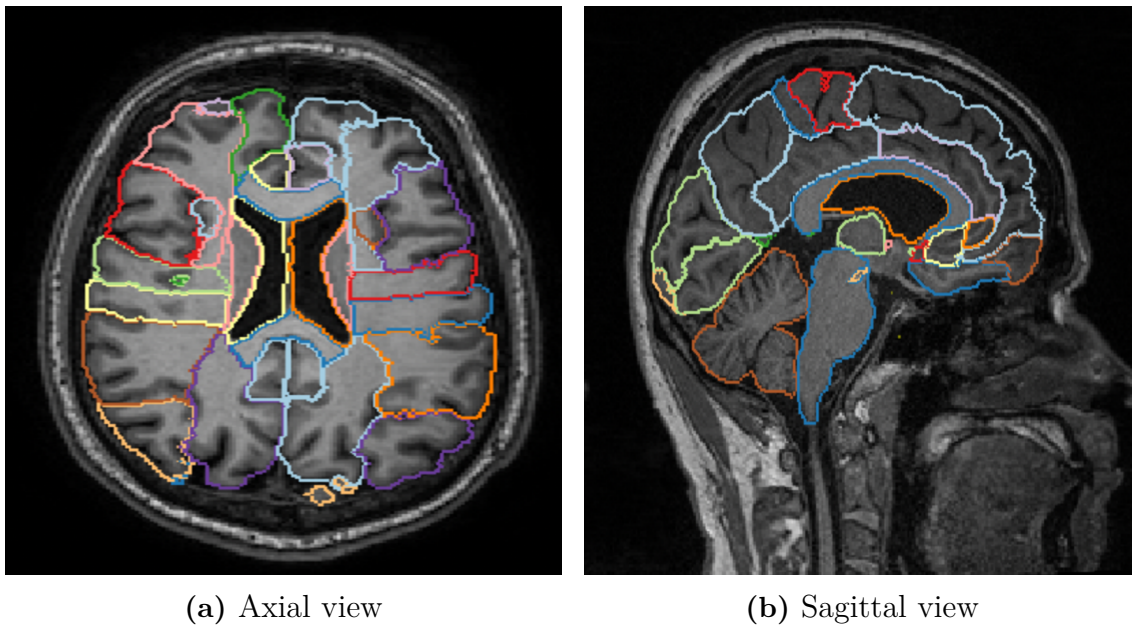


Figure 3.3: Label output from MAPER, visualised using MIRTk Viewer

3.7 Statistical analysis

The label output from MAPER needed to be processed to determine the volumes of 95 anatomical regions in each participant. The R package IKUB was downloaded from github.com/yupingikub and applied to convert the label output to volume. The data was assembled into the study cohorts presented in Section 3.1 using the R environment (r-project.org/).

An additional study cohort was created from all participants whose records indicated current or past epileptic seizures. These participants were not removed from their primary cohort; instead, they appear twice in the study.

Statistical analysis on the study cohorts was carried out using standard statistical methods provided by the R environment.

3.7.1 Individual regions

Data containing the 95 region volumes were normalised using a residual regression-based ICV normalisation method, proposed by Jack et al. [48], where a specific region volume is calculated as:

$$\text{Volume}_{\text{adjusted } i} = \text{Volume}_{\text{raw } i} - \beta (\text{ICV}_{\text{raw } i} - \text{ICV}_{\text{mean}}). \quad (3.1)$$

To analyse the individual region volumes, the region volumes were transformed to z-scores by:

$$z = \frac{x - \mu}{\sigma}. \quad (3.2)$$

where x is the volume of the specific region for a participant, μ is the mean value of the particular region for all study participants, and σ is the standard deviation for the specific region for all study participants. Region volumes were plotted per cohort as *morphometric fingerprints* using the z-scores.

3.7.2 Difference index between ICV and parenchyma volumes

To investigate the correlation between the ICV and parenchyma volumes, a difference index (DI) was generated for each participant as:

$$DI = 2 * \frac{ICV - Parenchyma}{ICV + Parenchyma}. \quad (3.3)$$

A high DI implies that there is a large difference between the ICV and parenchyma volume.

3.7.3 Asymmetry

The balanced asymmetry indices for paired regions was investigated for seven pre-determined regions. The asymmetry index was calculated as:

$$A_r = \frac{2|V_R - V_L|}{V_R + V_L}. \quad (3.4)$$

where V_R are the volume of the right region and V_L are the volume of the left region.

3.7.4 Multiple comparison

In this thesis, I am testing several hypotheses simultaneously, called multiple comparisons. When using multiple comparisons, the possibility of finding a rare event by random coincidence increases. Various methods have been proposed to compensate for the increased risk of finding a rare event when using multiple comparisons, such as Bonferroni correction, family-wise error rate, or the Benjamini-Hochberg procedure. In this thesis, I used the Benjamini-Hochberg procedure to reduce the chance of rejecting the null hypothesis, when it is in fact true (Type I error) [49].

For each case of multiple comparisons, the p-values are ranked from the lowest to the largest. I decided to accept a 5% false discovery rate. A Benjamini-Hochberg (B-H) critical value was calculated for each hypothesis as:

$$p^{BH} = (i/m)*Q. \quad (3.5)$$

When the p-value is lower than the B-H critical value, the hypothesis is considered accepted. In addition, all values that are lower than the highest accepted p-value are accepted.

4

Results

In the following chapter are the results from the segmentation review and analyse presented. The first two sections (4.1, 4.2) provides results from the quality evaluation of the intracranial masks and the individual region segmentations. Section 4.3 presents result from the exploratory session and provide hypotheses generated for ICV, difference index, individual regions and asymmetry on the half study group. In the Section 4.4, the hypotheses generated in Section 4.3 were tested on a test group to evaluate any significant differences between the controls and the other cohorts. The final section summarises the key findings of this project.

4.1 Quality of intracranial masks

The first set of analyses examined the quality of the intracranial masks on the Jaccard index from the Pinfram output. Visual assessments were carried out with MIRTK Viewer on segmentations with a Jaccard index below 0.970 or above 0.992 to identify obviously failed segmentations. Further visual assessments were performed on a randomly selected group of 50 images to identify any additional failures. Three images were removed from the study at this point due to acquisition faults. Table 4.1 provides a summary of the remaining study participants.

Table 4.1: Distribution of cohort and gender after evaluating the Pinfram results. The table also presents how many epilepsy participants belonged to each cohort.

	C	PD	SWEDD	GenPD	GenUn	Pr	Total
Female	65	138	21	51	105	10	390
Male	113	253	40	54	67	38	565
E*	(1)	(5)	(2)	(2)	(2)	(4)	(16)
Total	178	391	61	105	172	48	955

Note: E* = Epilepsy participants included in the cohorts.

4.2 Quality of individual region segmentation

During the visual review, it was found that approximately ten images showed a poor result. Most of these images were images acquired as 2D images, and borders

between brain regions were difficult to evaluate. A cut-off limit was selected to exclude as many uncertain images as possible from the study and leave as many valuable images as possible. The cut-off limit was set at to 0.6600, and each image with at least one agreement ratio under the limit was excluded. The procedure led to the exclusion of eight images. An updated breakdown of gender and cohort is presented in Table 4.2.

Table 4.2: Distribution of cohort and gender after evaluating the MAPER results. The table also presents how many epilepsy participants belong to each cohort.

	C	PD	SWEDD	GenPD	GenUn	Pr	Total
Female	65	138	21	49	105	9	387
Male	113	251	39	54	67	36	560
E*	(1)	(5)	(2)	(2)	(2)	(4)	(16)
Total	178	389	60	103	172	45	947

Note: E* Epilepsy participants included in the cohorts.

4.3 Exploration and hypothesis generation

Table 4.3 shows how many participants are included in the exploratory- and the test group, respectively. The remaining part of this section presents the exploratory results and the hypotheses generated from them. Results from the hypotheses tests are presented in the subsequent Section 4.4.

Table 4.3: Distribution of participants in randomly generated exploration and test groups.

	C	PD	SWEDD	GenPD	GenUn	Pr	E	Total
Exploration	89	194	30	51	86	22	8	480
Test	89	195	30	52	86	23	8	483

4.3.1 Intracranial volume

The intracranial volumes for the randomly selected exploration groups are presented together in Figure 4.1. Interestingly, there were differences in the median values of the cohorts compared to the control group. The observation raises the possibility of a difference in ICV between the cohorts and the control group. Therefore, alternative hypotheses were generated from the figure and are presented in Table A.1 in Appendix A.

4.3.2 Difference index

All DI were plotted together, arranged in cohorts, and are shown in Figure 4.2. From Figure 4.2 we can see that all cohorts have a DI above the control group. Hypotheses indicating a possibility that all cohorts have a higher DI than the control group are found in Table A.2 in appendix A.

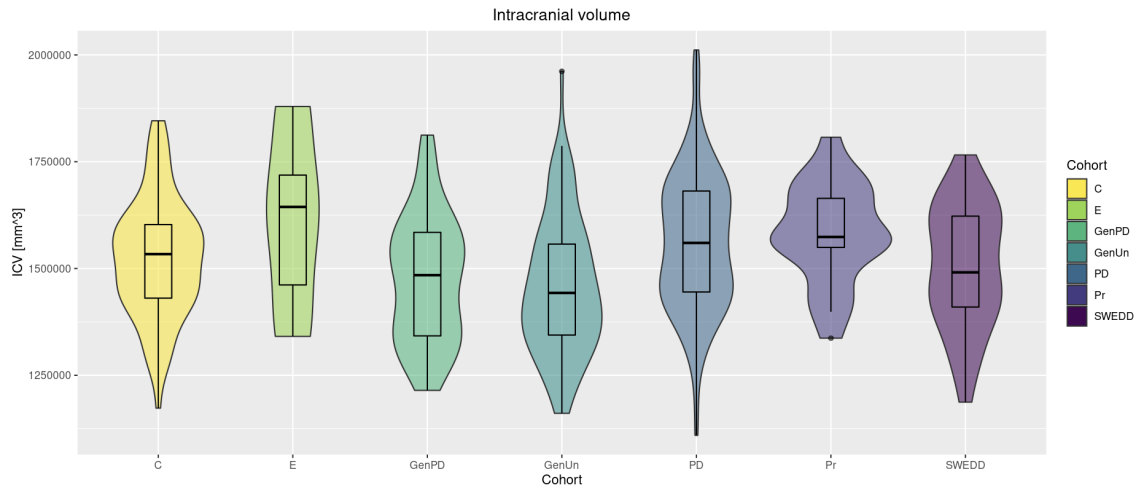


Figure 4.1: A violin boxplot with the intracranial volumes of the exploration half of the cohort groups

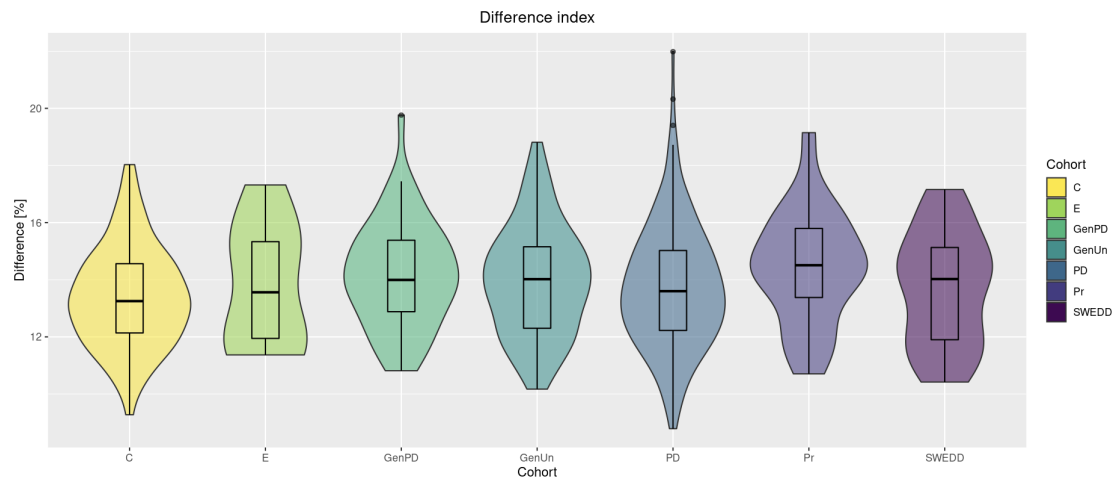


Figure 4.2: The figure shows a violin boxplot of the Difference index between ICV and parenchyma volume for the exploration group.

4.3.3 Individual region analysis

An analysis of individual regions was conducted to identify possible volume differences between the control group and the other cohorts. A morphometric fingerprint plot of the 95 regions with z-scores was generated for each cohort containing the exploration participants. The median z-score is marked for the specific cohort and the control group. Nine regions were selected for a deeper investigation in each cohort: seven regions were predetermined, and two regions were selected specifically for each cohort. The two regions selected in each cohort were chosen since they showed the most distinct differences between the control group and the specific cohort. Six of the seven predetermined regions were chosen, considering that they were connected to the nigrostriatal pathway. The six regions were: Putamen, Pallidum, Nucleus accumbens, Caudate nucleus, Thalamus and Substantia nigra. The seventh predetermined region was Hippocampus and was chosen as it is a region often involved

in epilepsy. Fingerprint plots for each cohort are found below.

PD

A fingerprint plot of the 95 individual region volumes calculated for the PD cohort is shown in Figure 4.3. What stands out in the figure is that a majority of the seven predetermined regions have a higher median z-score compared to the control group. The two regions with the largest difference compared to the control group were: *TL posterior temporal lobe* and *Insula middle short gyrus*, which both had a smaller z-score compared to the control group. Summation of generated hypothesis for the PD group can be found in Table A.3 in appendix A.

SWEDD

An inspection of the region volumes in Figure 4.4 reveals that the mean volume of *TL parahippocampal and ambient gyrus* and *OL lateral remainder occipital lobe* differs distinctly between the SWEDD group and the control group. Looking at the predetermined regions, *Pallidum* seems to differ most from the control group, which raises the possibility that Pallidum has a smaller volume in SWEDD participants compared to the controls. A summary of generated hypotheses (H_A) for the nine regions is found in Table A.4 in Appendix A.

GenPD

Differences in the median score between the control group and the GenPD group are highlighted in Figure 4.5. The most considerable differences between the controls and the GenPD group are seen in the regions: *TL middle and inferior temporal gyrus* and *TL anterior temporal lobe lateral*. Moreover, region *TL posterior temporal lobe lateral* and region *CG posterior cingulate gyrus* show a remarkable difference from the control group. Nevertheless, we are only choosing two regions to investigate further for each cohort and therefore, will no further investigations be made for *TL posterior temporal lobe lateral* and *CG posterior cingulate gyrus* in this thesis. A summation of the generated hypotheses for GenPD can be found in Table A.5 in Appendix A.

GenUn

The data in Figure 4.6 can be compared with the data in Figure 4.5 which shows that region *TL middle and inferior temporal gyrus* and *TL anterior temporal lobe lateral* have large differences compared to the control group in the GenUn participants as well. However, *TL anterior temporal lobe medial part* shows a slightly larger difference than *TL anterior temporal lobe lateral*. Therefore, the selected region to investigate further are *TL middle and inferior temporal gyrus* and *TL anterior temporal lobe medial part*. Table A.6 provides an overview of the hypotheses set for the GenUn cohort and are found in Appendix A.

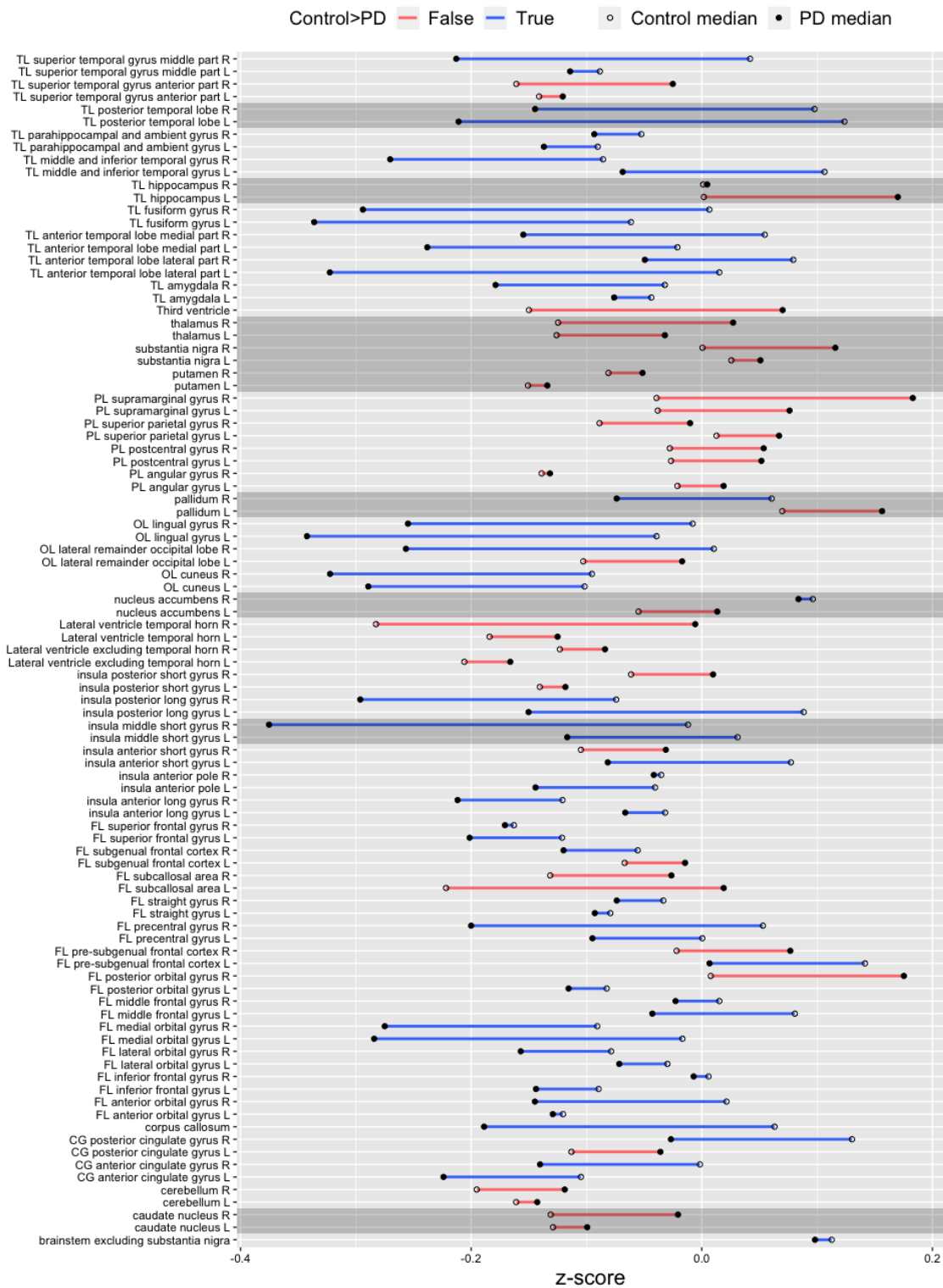


Figure 4.3: Fingerprint plot of the 95 regions comparing the control group against the PD group

Pr

Figure 4.7 shows the results obtained from the exploratory analysis of region volumes in the Pr group. As Figure 4.7 shows, there were several regions beyond the prede-

4. Results

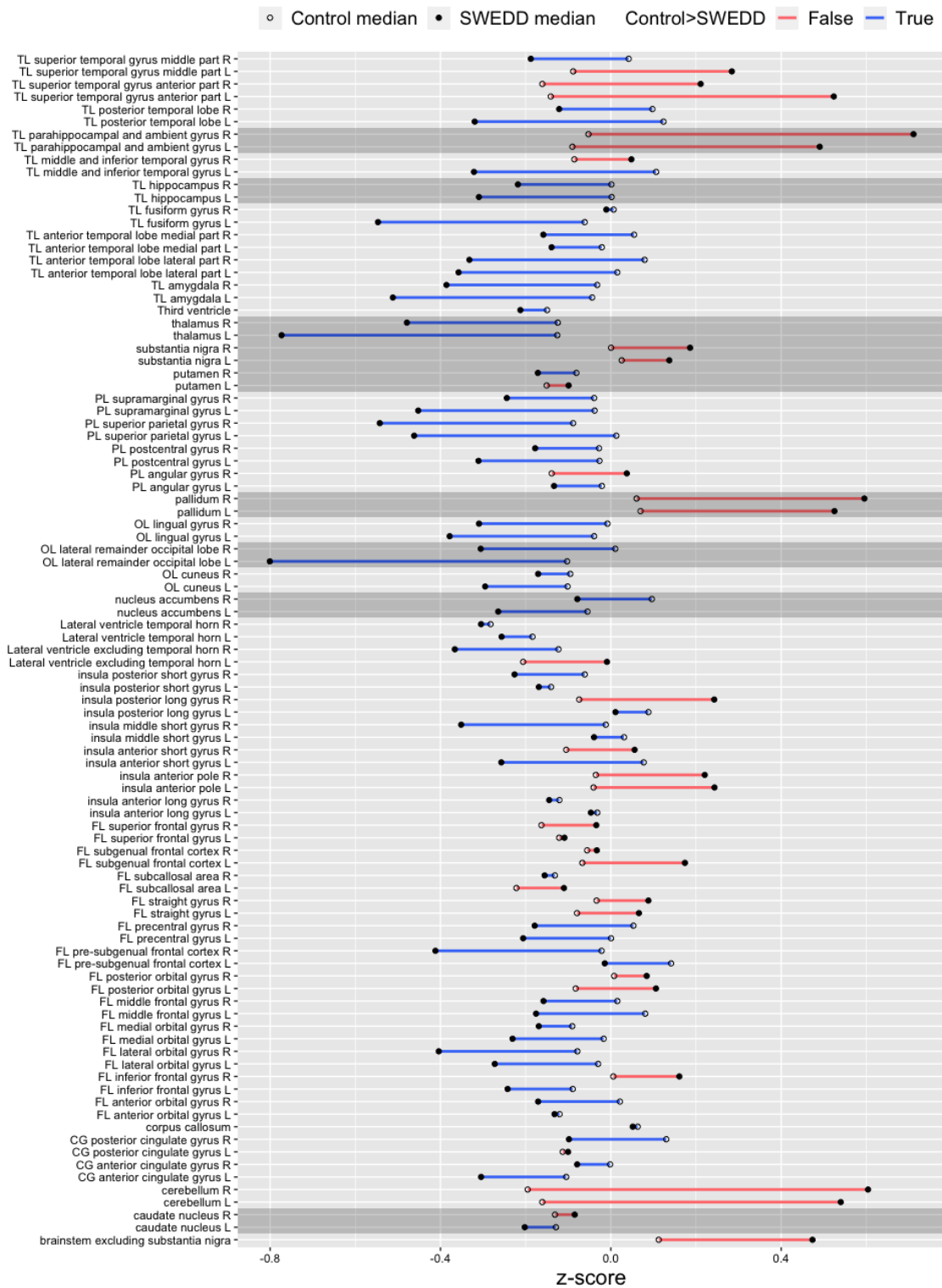


Figure 4.4: Fingerprint plot of the 95 regions comparing the control group against the SWEDD group

terminated ones that had a considerable difference between Pr and C. The two regions with the largest difference in z-score, *TL posterior temporal lobe* and *Insula middle*

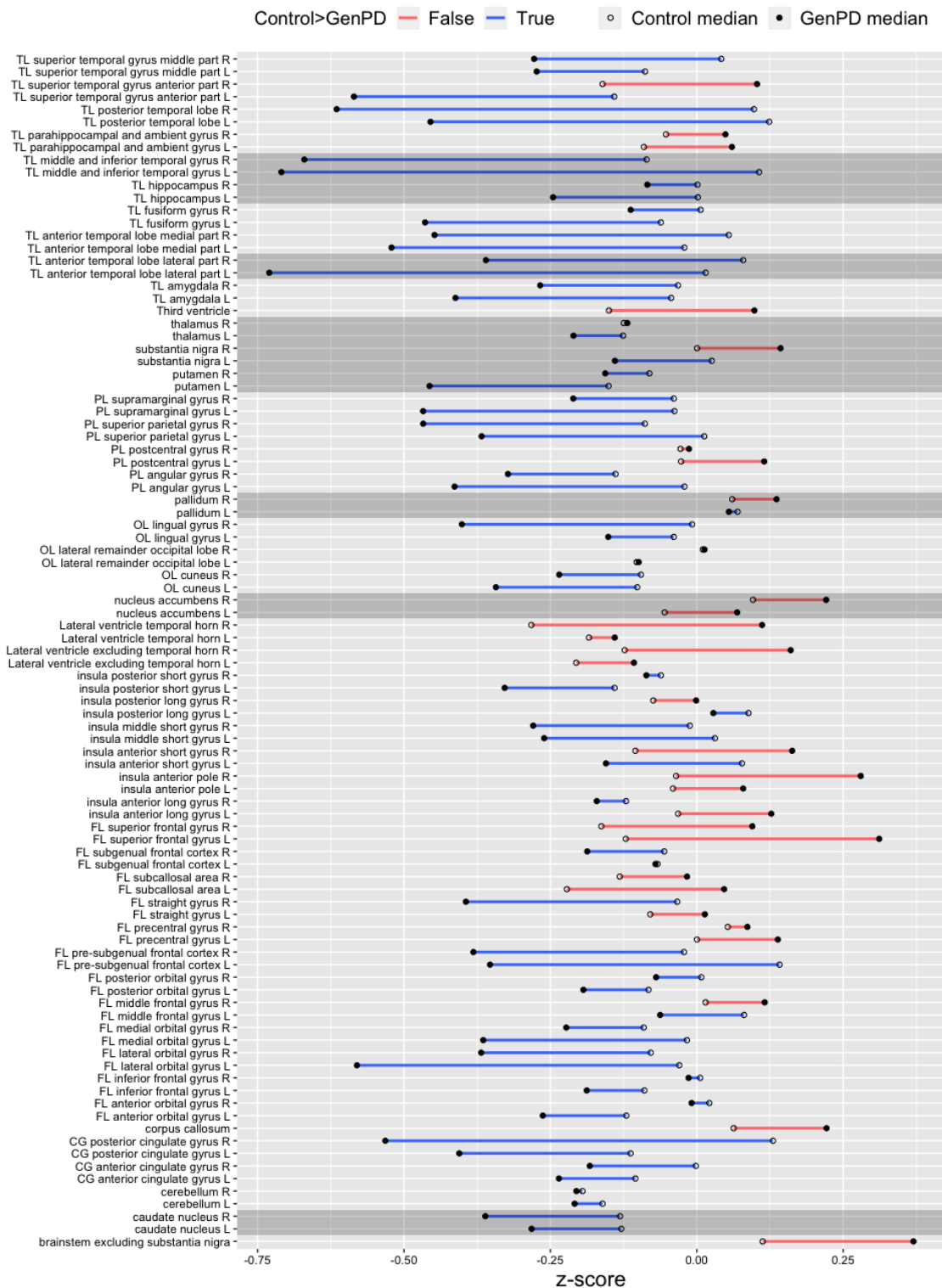


Figure 4.5: Fingerprint plot of the 95 regions comparing the control group against the GenPD group

short gyrus, were chosen to investigate further. Other interesting regions could have been *Lateral ventricle excluding temporal horn*, *FL posterior orbital gyrus* and *FL*

4. Results

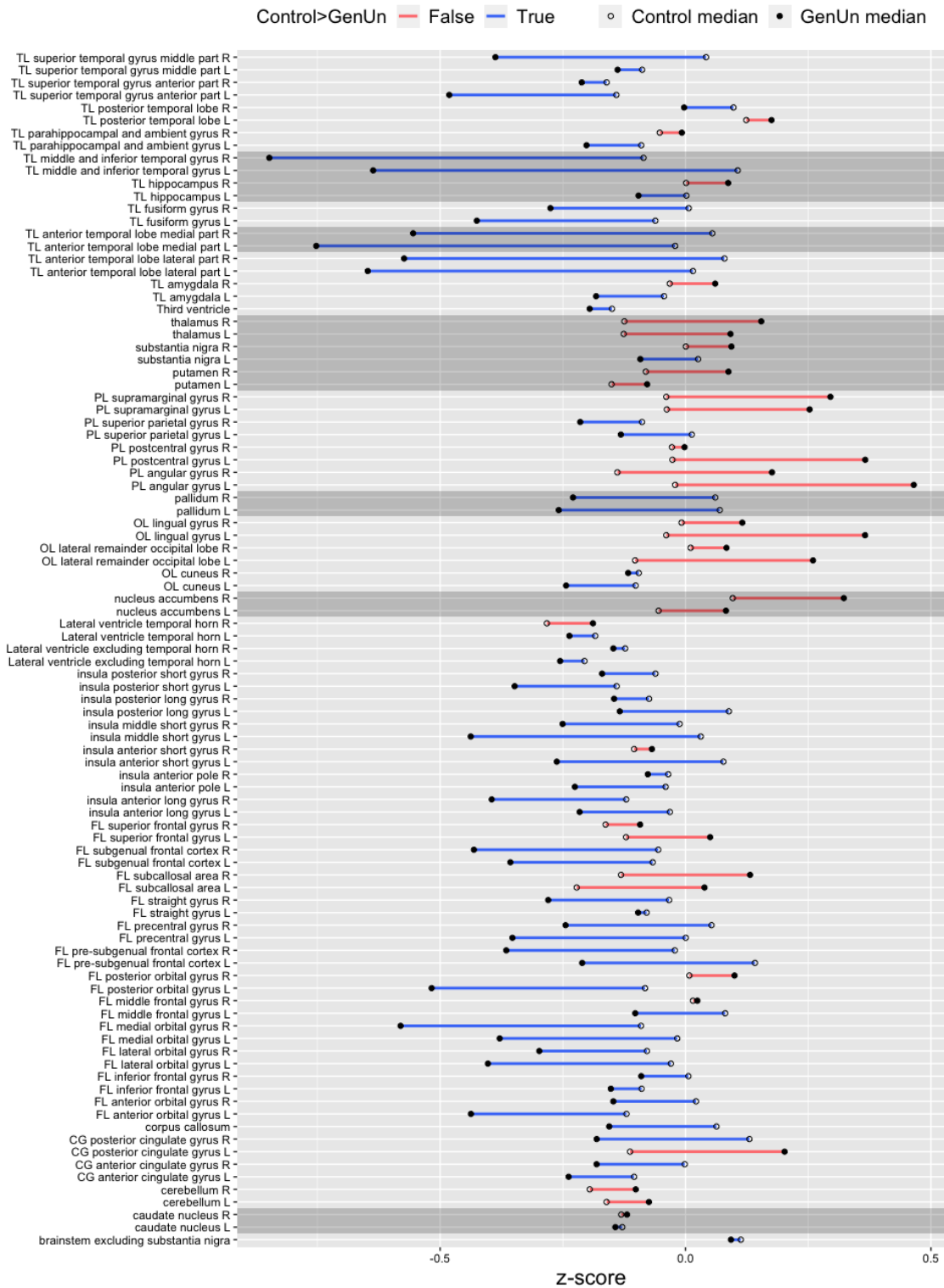


Figure 4.6: A fingerprint plot of the 95 regions comparing the control group against the GenUn group

middle frontal gyrus. A summary of the hypotheses can be found in Table A.7 in Appendix A.

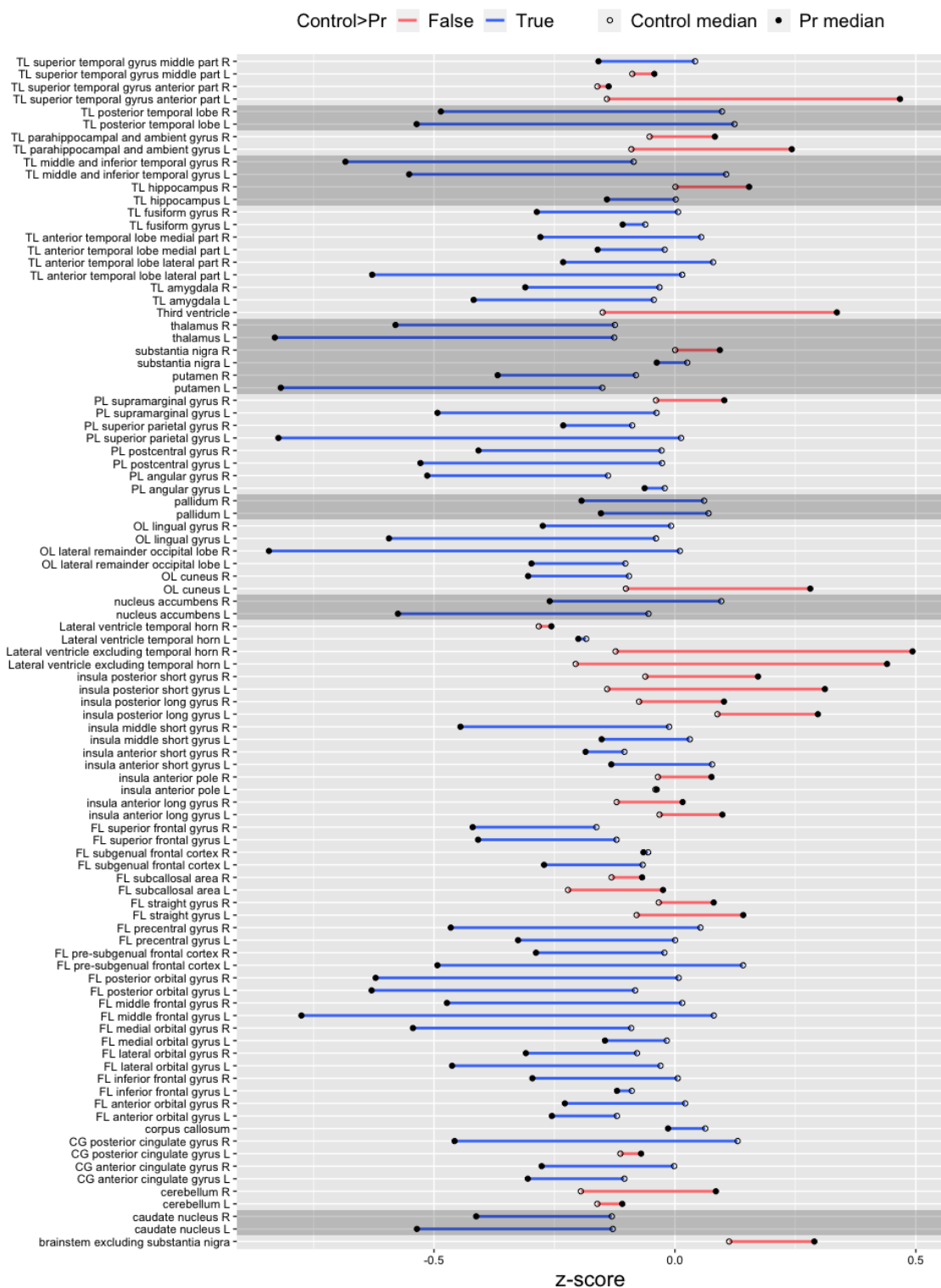


Figure 4.7: A fingerprint plot of the 95 regions comparing the control group with the Pr group

Epilepsy participants

A fingerprint plot of a comparison between the control group and epilepsy participants in the 95 regions are shown in Figure 4.8. The range of z-scores is larger for

4. Results

the epilepsy participants compared to the other cohorts. This is probably due to the small sample size of the epilepsy group. The most considerable z-score differences from the control group are found in the region *TL anterior temporal lobe lateral*, *Substantia nigra* and *TL superior temporal gyrus anterior part*. The generated hypotheses are listed in Table A.8 in Appendix A.

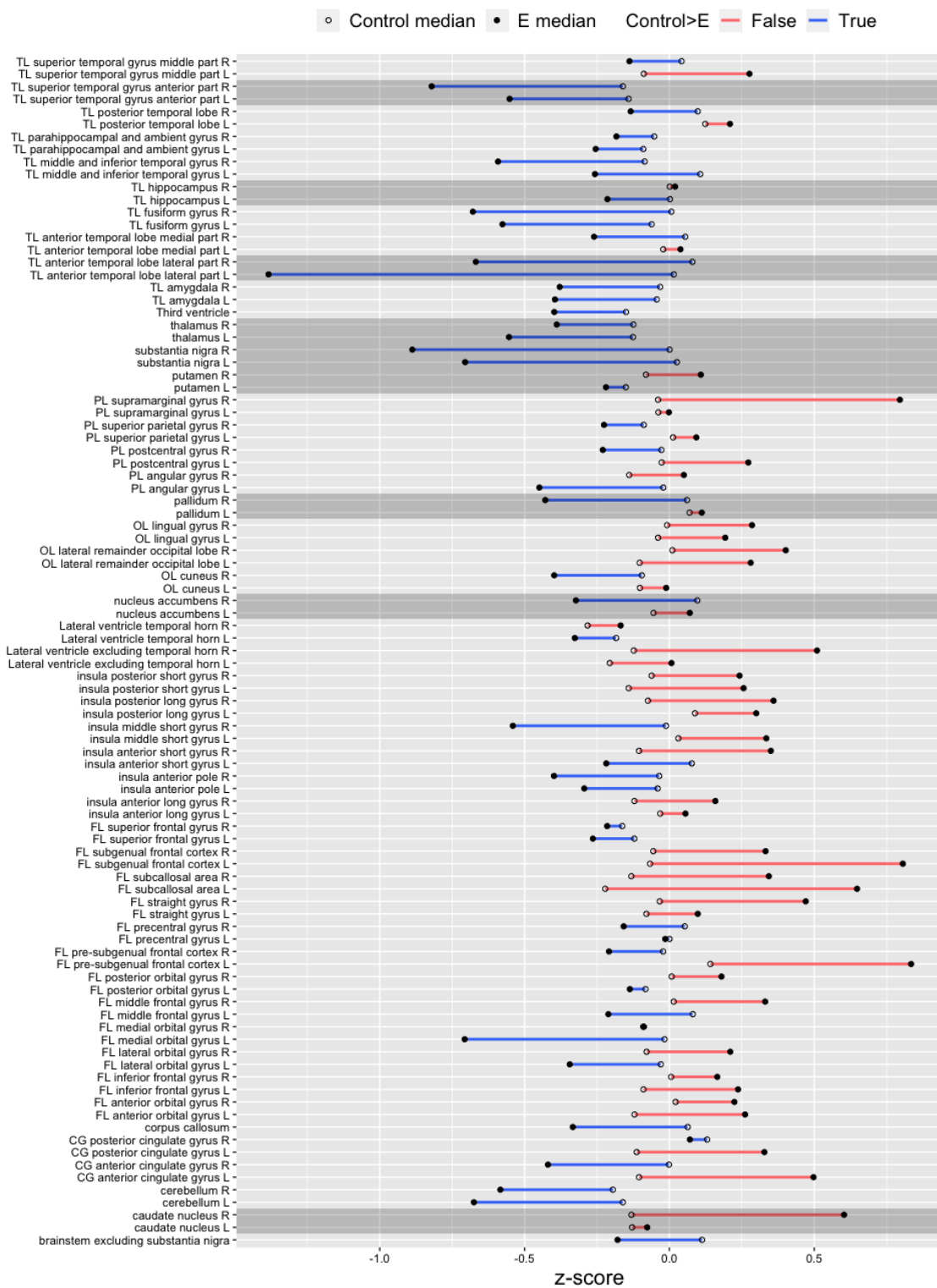


Figure 4.8: Fingerprint plot of the 95 regions comparing the control group with the E group

4.3.4 Asymmetry

Balanced asymmetry indices were calculated as presented in Section 3.7.3 for the seven predetermined paired regions. Outliers (asymmetry index greater than 1 or less than 0) were excluded from further investigation. The exploratory results are shown in Figure 4.9 and Figure 4.10. Various regions are associated with different index ranges. For example, Nucleus accumbens shows higher asymmetry indices in comparison to Thalamus. Hypotheses generated from the tables are found in Table A.9 in Appendix A.

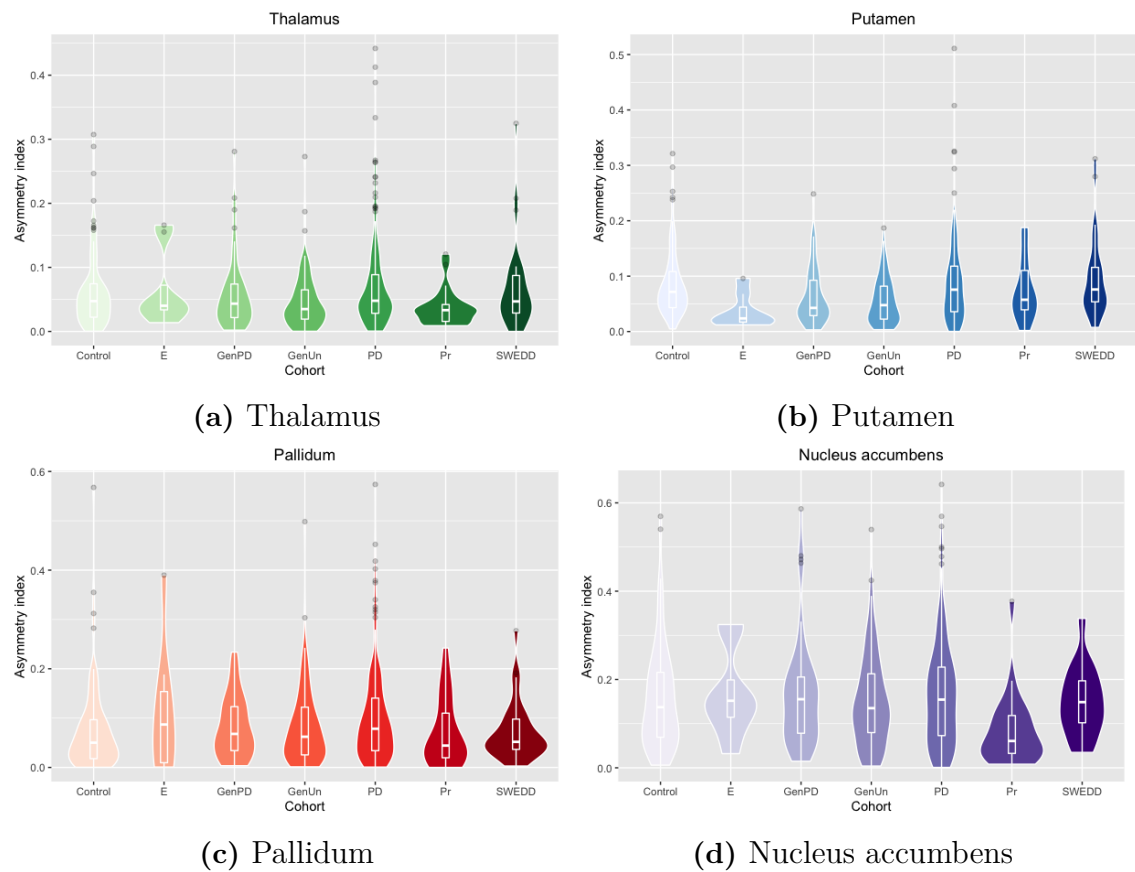


Figure 4.9: Asymmetry index for selected regions

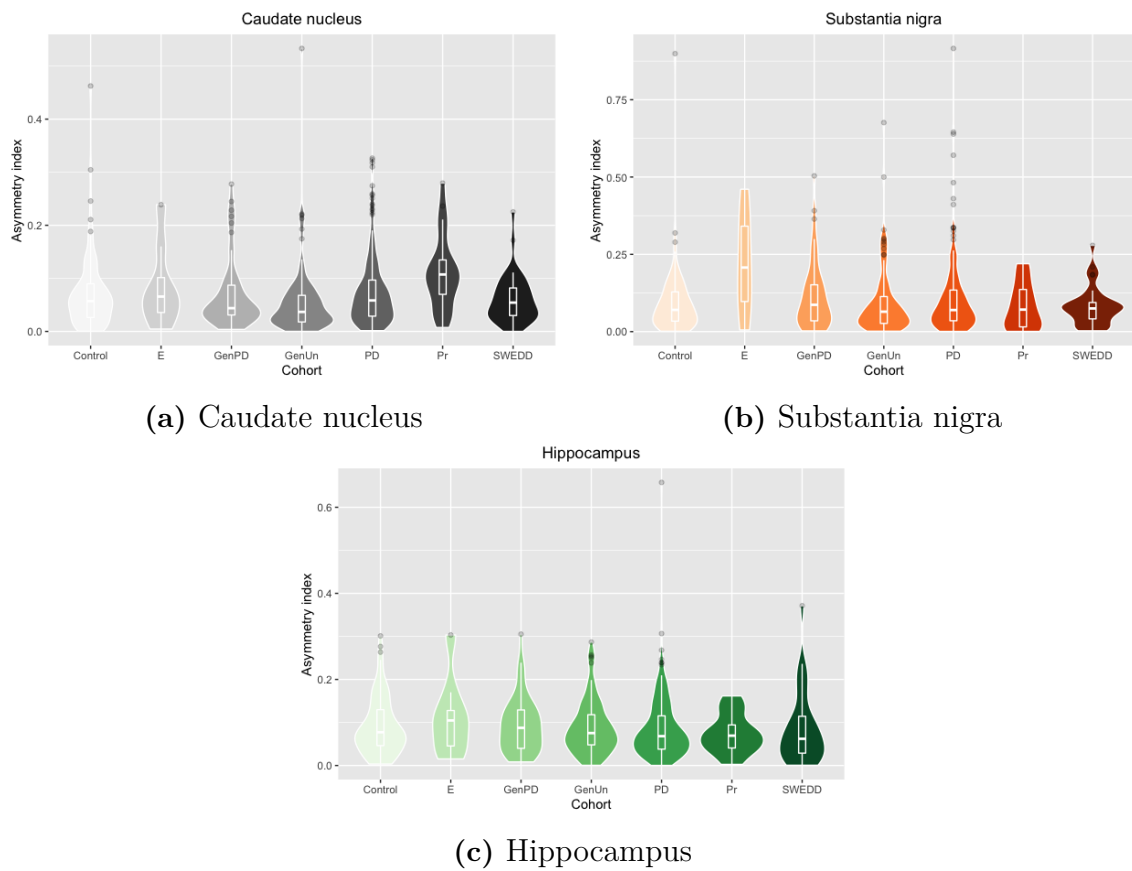


Figure 4.10: Asymmetry index for selected regions

4.4 Hypothesis testing

Generated hypotheses (cf. Section 4.3) were tested on the test group defined in Table 4.3. The cohorts are assumed to be normally distributed and independent from each other. Therefore, unpaired t-tests were performed to determine whether there is evidence for rejecting H_0 or not. When using multiple comparisons, the likelihood of observing a rare result increases. The Benjamini-Hochberg procedure was applied to adjust the significance level to compensate for the increased chance of finding a rare observation, as mentioned in Section 3.7.4. The False Discovery Rate (Q) was set to 0.05 for all tests.

4.4.1 Intracranial volume

The test group consisted of the second half of each cohort, and the intracranial volumes were plotted together in a violin plot once again, see Figure 4.11. By comparing Figure 4.11 with the exploratory results in Figure 4.1, one can observe that there are similar distributions of the ICV between the cohorts. The generated hypotheses (see Table A.1 in Appendix A), were tested and summarised in Table 4.4. Looking at Table 4.4, significant differences from the controls were found for PD, Pr and E ($p < 0.05$). When the significance level was adjusted, the p-value of Pr exceeded the critical value (p^{BH}). However, since the p-value for E was lower than the critical value ($.02486 < p^{BH}$), the p-value for Pr is considered significant. The results in Table 4.4 shows that PD, Pr, and E participants statistically have a larger intracranial volume compared to the controls.

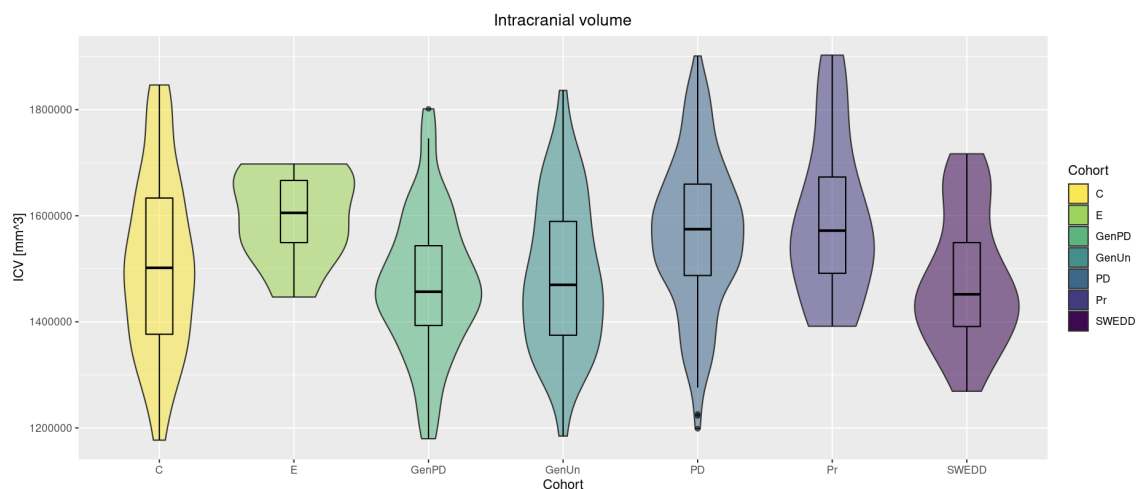


Figure 4.11: A violin boxplot with the intracranial volumes for the test half group

4.4.2 Difference index

The distribution of Difference indices for every test participant in the cohorts is found in Figure 4.12. What is striking about Figure 4.12 is that the Pr cohort has a median Difference index far above the other cohorts, which we saw indications of in Figure 4.2. As one can observe from Table 4.5, Pr and GenUn show a significant

Table 4.4: Results from the unpaired t-test for ICV.

T-test result				
Cohort	H_A :	Control mean	Cohort mean	P-Value
PD	C<PD	1508678	1566122	0.005316
SWEDD	C>SWEDD	1508678	1478379	0.2931
GenPD	C>GenPD	1508678	1469643	0.1279
GenUn	C>GenUn	1508678	1487968	0.3772
Pr	C<Pr	1508678	1593206	0.02481
E	C<E	1508678	1599968	0.02486
Benjamini-Hochberg procedure				
Cohort	P-value	Rank	p^{BH}	Reject the null hypothesis
PD	0.005316	1	0.008	✓
Pr	0.02481	2	0.017	✓
E	0.02486	3	0.025	✓
GenPD	0.1279	4	0.033	X
SWEDD	0.2931	5	0.042	X
GenUn	0.3772	6	0.050	X

Note: H_A = Alternative hypotheses generated in the exploratory part.

difference compared to the controls. Both Pr and GenUn are expected to have a larger difference between ICV and parenchyma volume compare to the control group.

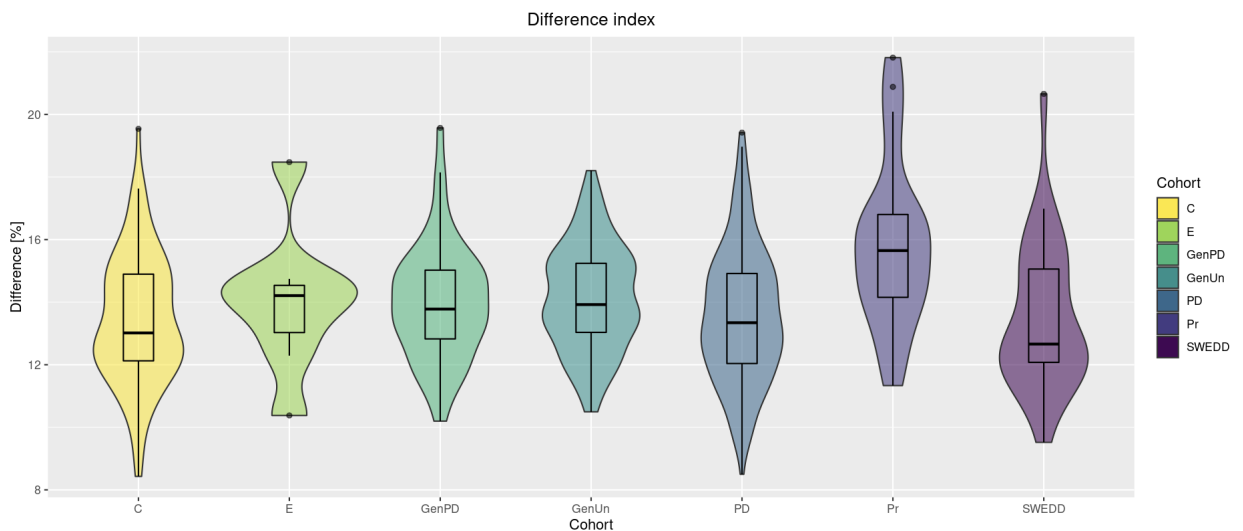


Figure 4.12: The figure shows a violin boxplot of the Difference index between ICV and parenchyma volume for the test group

Table 4.5: Results from the unpaired t-test for Difference index comparing ICV and Parenchyma.

T-test result				
Cohort	H_A :	Control mean	Cohort mean	P-Value
PD	C<PD	0.1344010	0.135671	0.635
SWEDD	C<SWEDD	0.1344010	0.1350488	0.8933
GenPD	C<GenPD	0.1344010	0.1398494	0.1092
GenUn	C<GenUn	0.1344010	0.1412968	0.01674
Pr	C<Pr	0.1344010	0.1582557	0.0004239
E	C<E	0.1344010	0.1400655	0.5228
Benjamini-Hochberg procedure				
Cohort	P-value	Rank	p^{BH}	Reject the null hypothesis
Pr	0.0004239	1	0.008	✓
GenUn	0.01674	2	0.017	✓
GenPD	0.1092	3	0.025	X
E	0.5228	4	0.033	X
PD	0.635	5	0.042	X
SWEDD	0.8933	6	0.050	X

Note: H_A = Alternative hypotheses generated in the exploratory part.

4.4.3 Individual region analysis

This subsection provides results from the hypothesis tests made on the nine hypotheses stated in each cohort in subsection 4.3. The hypotheses are tested region-wise, in contrast to cohort-wise as the hypotheses were generated in Subsection 4.3. The advantage of using a region-wise method is that it is useful for identifying and characterising differences between the cohorts in a specific region. The hypotheses were tested with an unpaired t-test, and the significance levels were corrected by the use of the Benjamini-Hochberg procedure. As for previously described tests, the False Discovery Rate (Q) was set at 0.05. Mean values for each region volume are presented in the tables below and are rounded to one or zero decimals.

Thalamus

Figure 4.13a shows the distribution of *Thalamus* volumes for the six cohorts. Table 4.6 provides the mean and p-value results from the unpaired t-test, together with the Benjamini-Hochberg procedure. As shown in Table 4.6, there is a significant difference in Thalamus volume between the controls and SWEDD group ($p < .05$). However, when the significant levels are corrected, no cohort shows a significant difference in Thalamus volume compared to the control group.

Putamen

The distribution of participants volumes for Putamen is shown in Figure 4.13b. As one can notice from Table 4.7, Pr provides a small P-value ($p < 0.01$). However,

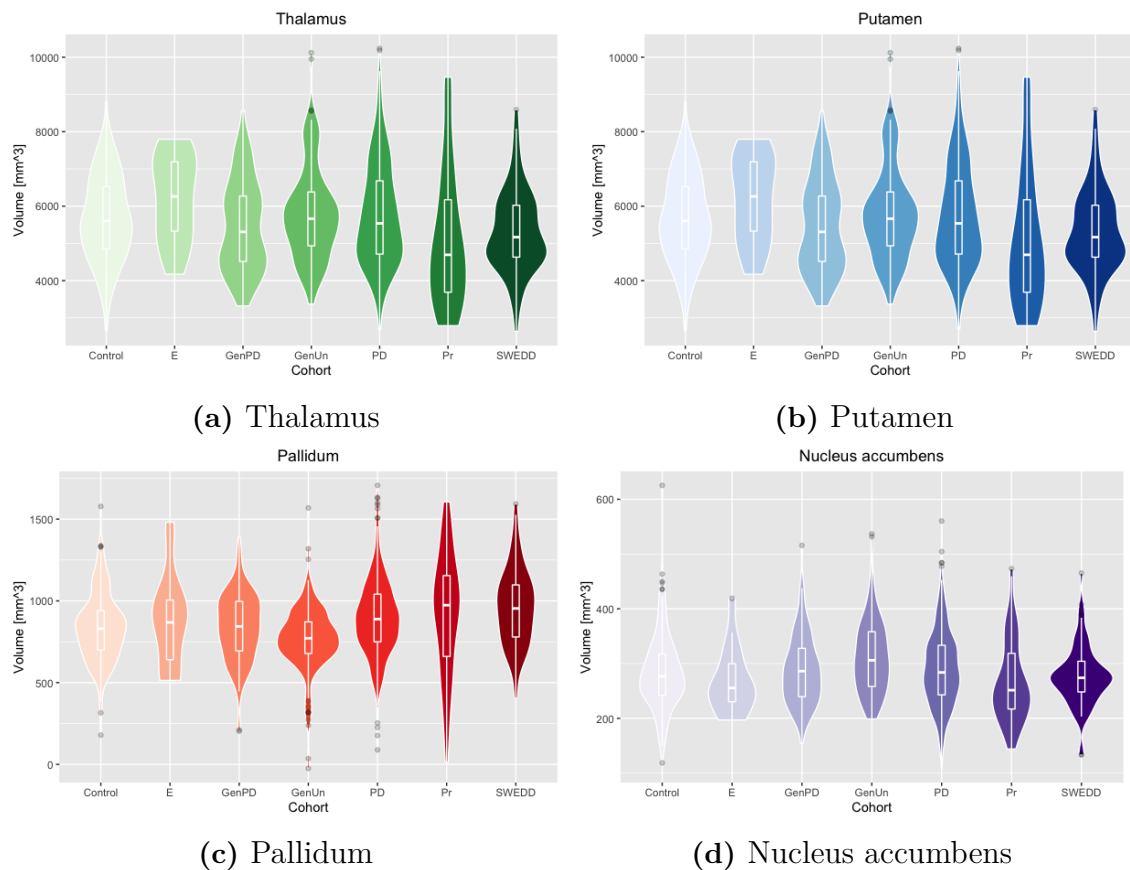


Figure 4.13: Volumes for selected regions

correction with Benjamini-Hochberg procedure still accepts the null hypotheses according to the definition. Moreover, there were no significant differences between the controls and the other cohorts in *Putamen* volume.

Pallidum

As we can notice from the hypotheses in Table 4.8, *Pallidum* had a smaller volume for the majority of the cohorts in the exploratory part compared to the controls. We can observe in Table 4.8, that three of the cohorts received a p-value indicating that the null hypotheses could be rejected: PD, SWEDD and GenUn. A visualisation of the results is shown in Figure 4.13c.

Nucleus accumbens

Visual results for *Nucleus accumbens* volume within the cohorts are seen in Figure 4.13d. As can be noticed in the Figure, *Nucleus accumbens* is a smaller region compared to previously mentioned regions. The results in Table 4.9 reveals that GenUn is the only cohort that has a significantly larger volume compared to the control group, and the t-test results accept the alternative hypothesis that was stated in the exploratory session.

Table 4.6: Results from the unpaired t-test for Thalamus.

T-test result				
Cohort	H_A :	Control mean	Cohort mean	P-Value
PD	C<PD	5680.8	5766.9	0.4411
SWEDD	C>SWEDD	5680.8	5325.8	0.04081
GenPD	C>GenPD	5680.8	5462.6	0.1419
GenUn	C<GenUn	5680.8	5792.2	0.3889
Pr	C>Pr	5680.8	5139.1	0.06211
E	C>E	5680.8	6198.2	0.1047
Benjamini-Hochberg procedure				
Cohort	P-value	Rank	p^{BH}	Reject the null hypothesis
SWEDD	0.04081	1	0.008	X
Pr	0.06211	2	0.017	X
E	0.1047	3	0.025	X
GenPD	0.1419	4	0.033	X
GenUn	0.3889	5	0.042	X
PD	0.4411	6	0.050	X

Note: H_A = Alternative hypotheses generated in the exploratory part.

Table 4.7: Results from the unpaired t-test for Putamen.

T-test result				
Cohort	H_A :	Control mean	Cohort mean	P-Value
PD	C<PD	4251.3	4264.6	0.8694
SWEDD	C>SWEDD	4251.3	4214.0	0.7072
GenPD	C>GenPD	4251.3	4217.4	0.7521
GenUn	C>GenUn	4251.3	4406.4	0.06594
Pr	C>Pr	4251.3	3849.3	0.008458
E	C<E	4251.3	4029.4	0.129
Benjamini-Hochberg procedure				
Cohort	P-value	Rank	p^{BH}	Reject the null hypothesis
Pr	0.008458	1	0.0083	X
GenUn	0.06594	2	0.017	X
E	0.129	3	0.025	X
SWEDD	0.7072	4	0.033	X
GenPD	0.7521	5	0.042	X
PD	0.8694	6	0.050	X

Caudate nucleus

A comparison of the *Caudate nucleus* volume between all cohorts can be found in Figure 4.14a. We can observe from the figure that several outliers in the GenPD, PD, Pr group differ up to 250 % from the median values. Apart from the outliers,

Table 4.8: Results from the unpaired t-test for Pallidum.

T-test result				
Cohort	H_A :	Control mean	Cohort mean	P-Value
PD	C>PD	838.2	896.7	0.003634
SWEDD	C<SWEDD	838.2	964.1	0.0005336
GenPD	C<GenPD	838.2	840.3	0.9359
GenUn	C>GenUn	838.2	767.7	0.001593
Pr	C>Pr	838.2	924.3	0.1381
E	C>E	838.2	879.8	0.5839
Benjamini-Hochberg procedure				
Cohort	P-value	Rank	p^{BH}	Reject the null hypothesis
SWEDD	0.0005336	1	0.0083	✓
GenUn	0.001593	2	0.017	✓
PD	0.003634	3	0.025	✓
Pr	0.1381	4	0.033	X
E	0.5839	5	0.042	X
GenPD	0.9359	6	0.050	X

Note: H_A = Alternative hypotheses generated in the exploratory part.

Table 4.9: Results from the unpaired t-test for Nucleus accumbens.

T-test result				
Cohort	H_A :	Control mean	Cohort mean	P-Value
PD	C<PD	284.6	290.8	0.3204
SWEDD	C>SWEDD	284.6	277.2	0.4193
GenPD	C<GenPD	284.6	287.9	0.6802
GenUn	C<GenUn	284.6	312.4	0.0001501
Pr	C>Pr	284.6	267.4	0.1673
E	C>E	284.6	268.4	0.3246
Benjamini-Hochberg procedure				
Cohort	P-value	Rank	p^{BH}	Reject the null hypothesis
GenUn	0.0001501	1	0.0083	✓
Pr	0.1673	2	0.017	X
PD	0.3204	3	0.025	X
E	0.3246	4	0.033	X
SWEDD	0.4193	5	0.042	X
GenPD	0.6802	6	0.050	X

Note: H_A = Alternative hypotheses generated in the exploratory part.

GenUn is the only cohort with a p-value <.05. When using Benjamini-Hochberg procedure, there was not any significant evidence for rejecting the null hypothesis.

4. Results

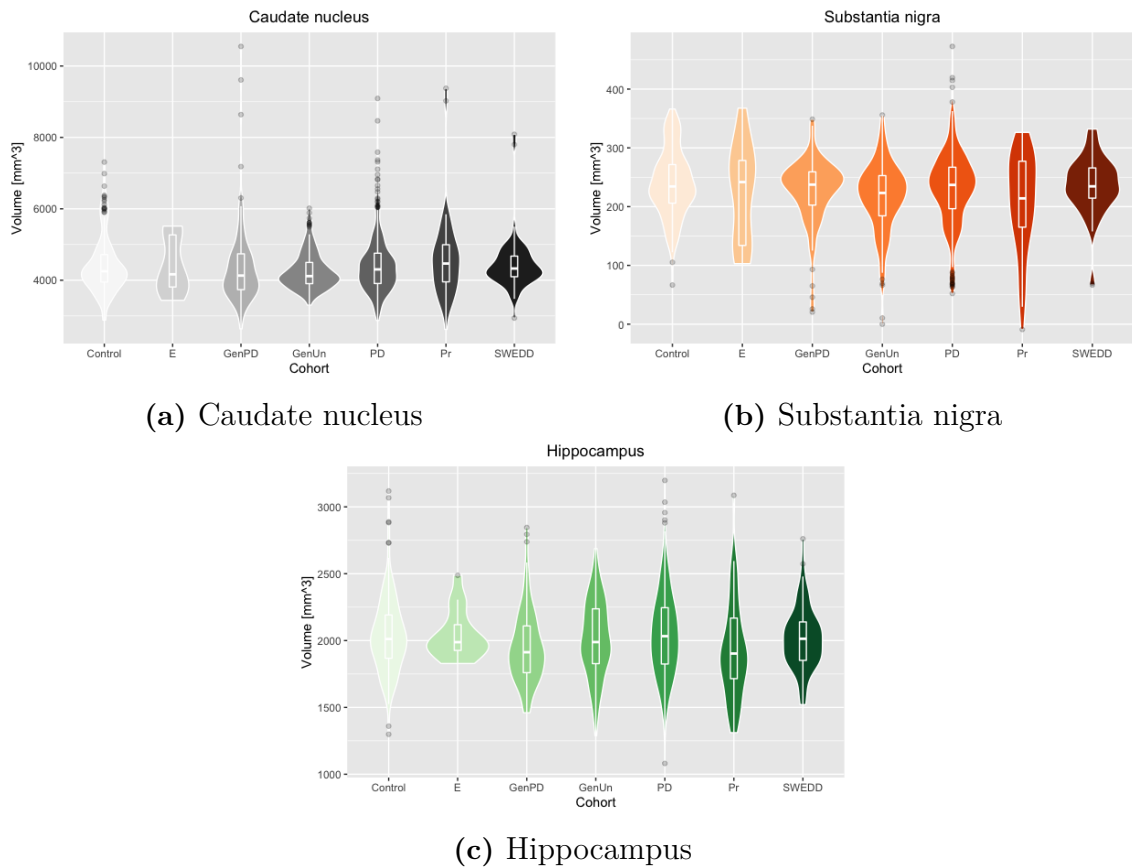


Figure 4.14: Volumes for selected regions

Table 4.10: Results from the unpaired t-test for Caudate nucleus.

T-test result				
Cohort	H_A :	Control mean	Cohort mean	P-Value
PD	$C < PD$	4418.2	4431.0	0.8624
SWEDD	$C > SWEDD$	4418.2	4455.8	0.7531
GenPD	$C > GenPD$	4418.2	4410.4	0.9526
GenUn	$C > GenUn$	4418.2	4264.5	0.03431
Pr	$C > Pr$	4418.2	4625.2	0.2849
E	$C < E$	4418.2	4392.4	0.8997
Benjamini-Hochberg procedure				
Cohort	P-value	Rank	p^{BH}	Reject the null hypothesis
GenUn	0.03431	1	0.0083	X
Pr	0.2849	2	0.017	X
SWEDD	0.7531	3	0.025	X
PD	0.8624	4	0.033	X
E	0.8997	5	0.042	X
GenPD	0.9526	6	0.050	X

Substantia nigra

Substantia nigra is the smallest region observed in this thesis. We can observe from Table 4.11 that all mean values of the test groups were slightly smaller than the mean value of the control . GenUn, Pr and GenPD received a p-value $<.05$. Although, when using the Benjamini-Hochberg procedure, only the GenUn and Pr groups can be considered as differing significantly from the control group.

Table 4.11: Results from the unpaired t-test for Substantia nigra.

T-test result				
Cohort	H_A :	Control mean	Cohort mean	P-Value
PD	C<PD	239.8	231.3	0.1139
SWEDD	C<SWEDD	239.8	235.8	0.6156
GenPD	C>GenPD	239.8	225.6	0.04839
GenUn	C>GenUn	239.8	216.5	0.0002748
Pr	C<Pr	239.8	207.3	0.01563
E	C>E	239.8	225.5	0.507
Benjamini-Hochberg procedure				
Cohort	P-value	Rank	p^{BH}	Reject the null hypothesis
GenUn	0.0002748	1	0.0083	✓
Pr	0.01563	2	0.017	✓
GenPD	0.04839	3	0.025	X
PD	0.1139	4	0.033	X
E	0.507	5	0.042	X
SWEDD	0.6156	6	0.050	X

Note: H_A = Alternative hypotheses generated in the exploratory part.

Hippocampus

Hippocampus is a predetermined region chosen for its involvement in epilepsy. Although, we can observe from table 4.12 that the epilepsy (E) group did not reveal any significant difference in comparison to the control group. Likewise the epilepsy group, we can not observe any significant difference for any of the other cohorts.

4. Results

Table 4.12: Results from the unpaired t-test for Hippocampus.

T-test result				
Cohort	H_A :	Control mean	Cohort mean	P-Value
PD	C<PD	2040.6	2043.4	0.9185
SWEDD	C>SWEDD	2040.6	2018.2	0.5547
GenPD	C>GenPD	2040.6	1956.7	0.01741
GenUn	C>GenUn	2040.6	2014.2	0.3919
Pr	C<Pr	2040.6	1925.5	0.05337
E	C>E	2040.6	2043.6	0.9537
Benjamini-Hochberg procedure				
Cohort	P-value	Rank	p^{BH}	Reject the null hypothesis
GenPD	0.01741	1	0.0083	X
Pr	0.05337	2	0.017	X
GenUn	0.3919	3	0.025	X
SWEDD	0.5547	4	0.033	X
PD	0.9185	5	0.042	X
E	0.9537	6	0.050	X

Note: H_A = Alternative hypotheses generated in the exploratory part.

Cohort-specific regions

The tables below provide the results from the cohort-specific regions. As we can observe from Table 4.13, 4.14 and 4.18, there were no significant difference observed between the PD, SWEDD or E and the controls in the selected regions.

Table 4.13: PD specific regions.

<p>Region: TL posterior temporal lobe $H_A: C_m > PD_m$ C_m: 48 578 PD_m: 48 903 p-value: 0.2563 p-value $>.05 \rightarrow X$</p>	<p>Region: Insula middle short gyrus $H_A: C_m > PD_m$ C_m: 1088.4 PD_m: 1073.2 p-value: 0.4424 p-value $>.05 \rightarrow X$</p>

Table 4.14: SWEDD specific regions.

<p>Region: TL parahippocampal and ambient gyrus $H_A: C_m < SWEDD_m$ C_m: 5898.0 $SWEDD_m$: 5911.6 p-value: 0.9215 p-value $>.05 \rightarrow X$</p>	<p>Region: OL lateral remainder occipital lobe $H_A: C_m > SWEDD_m$ C_m: 44 508 $SWEDD_m$: 44 023 p-value: 0.3367 p-value $>.05 \rightarrow X$</p>

The region *TL middle and inferior temporal gyrus* were selected from the exploration part for GenUn, GenPD and Pr, as can be seen in Table A.5, A.6 and A.7 in Appendix A. We can observe from the alternative hypotheses in table 4.15, 4.17 and 4.16 that all of the three cohorts assumes to have a smaller volume of *TL middle and inferior temporal gyrus* compared to the control group. Since the p-value was smaller than 0.03 ($p < .03$) for all of the three cohorts, we can reject the null hypotheses in these cases and assume that there is a significant difference.

As can shown in Table 4.17, *TL posterior temporal lobe* seems to be significantly smaller in the GenPD group compared to the control group.

For the GenUn cohort, *TL anterior temporal lobe medial part* is found to be significantly smaller than for the control group.

4. Results

Table 4.15: Pr specific regions.

<p>TL posterior temporal lobe</p>	<p>TL middle and inferior temporal gyrus</p>
<p>Region: TL posterior temporal lobe</p> <p>$H_A: C_m > Pr_m$</p> <p>C_m: 48 578</p> <p>Pr_m: 49 033</p> <p>p-value: 0.319</p> <p>p-value $>.05 \rightarrow X$</p>	<p>Region: TL middle and inferior temporal gyrus</p> <p>$H_A: C_m > Pr_m$</p> <p>C_m: 18 276</p> <p>Pr_m: 17 117</p> <p>p-value: 0.000746</p> <p>p-value $<.05 \rightarrow \checkmark$</p>

Table 4.16: GenUn specific regions.

<p>TL middle and inferior temporal gyrus</p>	<p>TL anterior temporal lobe medial part</p>
<p>Region: TL middle and inferior temporal gyrus</p> <p>$H_A: C_m > GenUn_m$</p> <p>C_m: 18 276</p> <p>$GenUn_m$: 17 173</p> <p>p-value: 6.896e-08</p> <p>p-value $<.05 \rightarrow \checkmark$</p>	<p>Region: TL anterior temporal lobe medial part</p> <p>$H_A: C_m > GenUn_m$</p> <p>C_m: 8188</p> <p>$GenUn_m$: 7749</p> <p>p-value: 3.805e-05</p> <p>p-value $<.05 \rightarrow \checkmark$</p>

Table 4.17: GenPD specific regions.

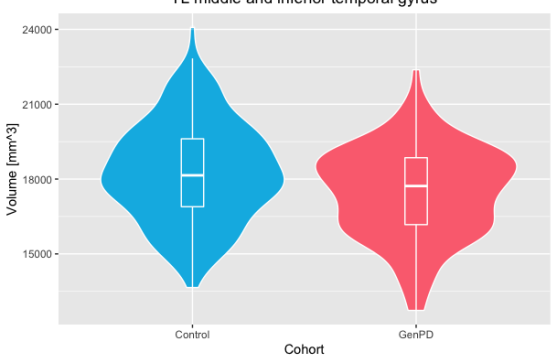
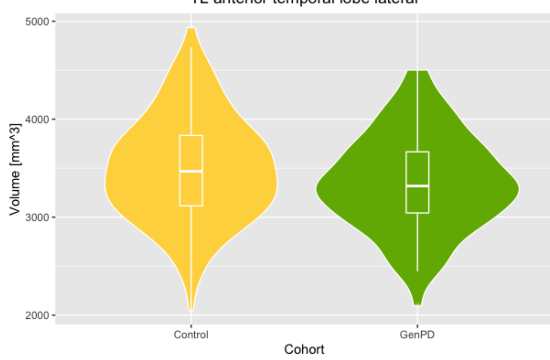
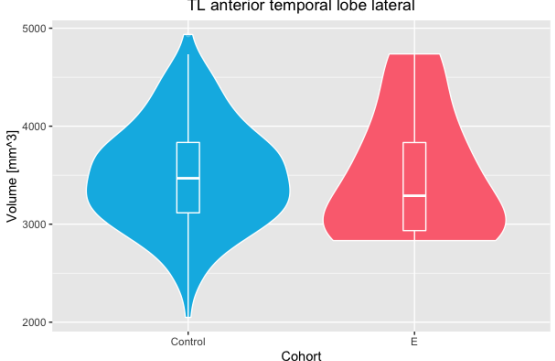
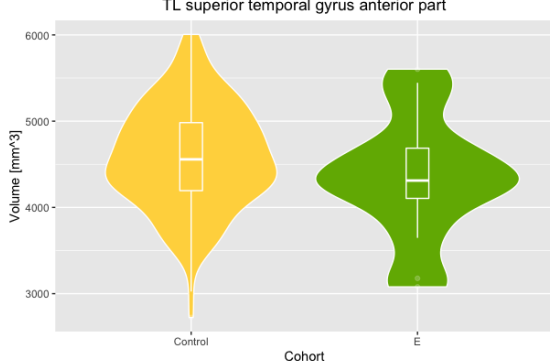
	
<p>Region: TL middle and inferior temporal gyrus $H_A: C_m > \text{GenPD}_m$ C_m: 18 276 GenPD_m: 17 478 p-value: 0.0007463 p-value $< .05 \rightarrow \checkmark$</p>	<p>Region: TL anterior temporal lobe lateral $H_A: C_m > \text{GenPD}_m$ C_m: 3501 GenPD_m: 3356 p-value: 0.021 p-value $< .05 \rightarrow \checkmark$</p>

Table 4.18: E specific regions.

	
<p>Region: TL anterior temporal lobe lateral $H_A: C_m > E_m$ C_m: 3501 E_m: 3477 p-value: 0.8856 p-value $> .05 \rightarrow X$</p>	<p>Region: TL superior temporal gyrus anterior part $H_A: C_m > E_m$ C_m: 4587 E_m: 4358 p-value: 0.2271 p-value $> .05 \rightarrow X$</p>

4.4.4 Asymmetry

This subsection provides the results from the asymmetry analysis. Asymmetry analysis was made for all cohorts on the seven predetermined regions Thalamus, Putamen, Pallidum, Nucleus accumbens, Nucleus accumbens, Substantia nigra and Hippocampus. Statistical significance was analysed using an unpaired t-tests on the hypotestes generated in Section 4.3. The significant levels were corrected with Benjamini-Hochberg procedure.

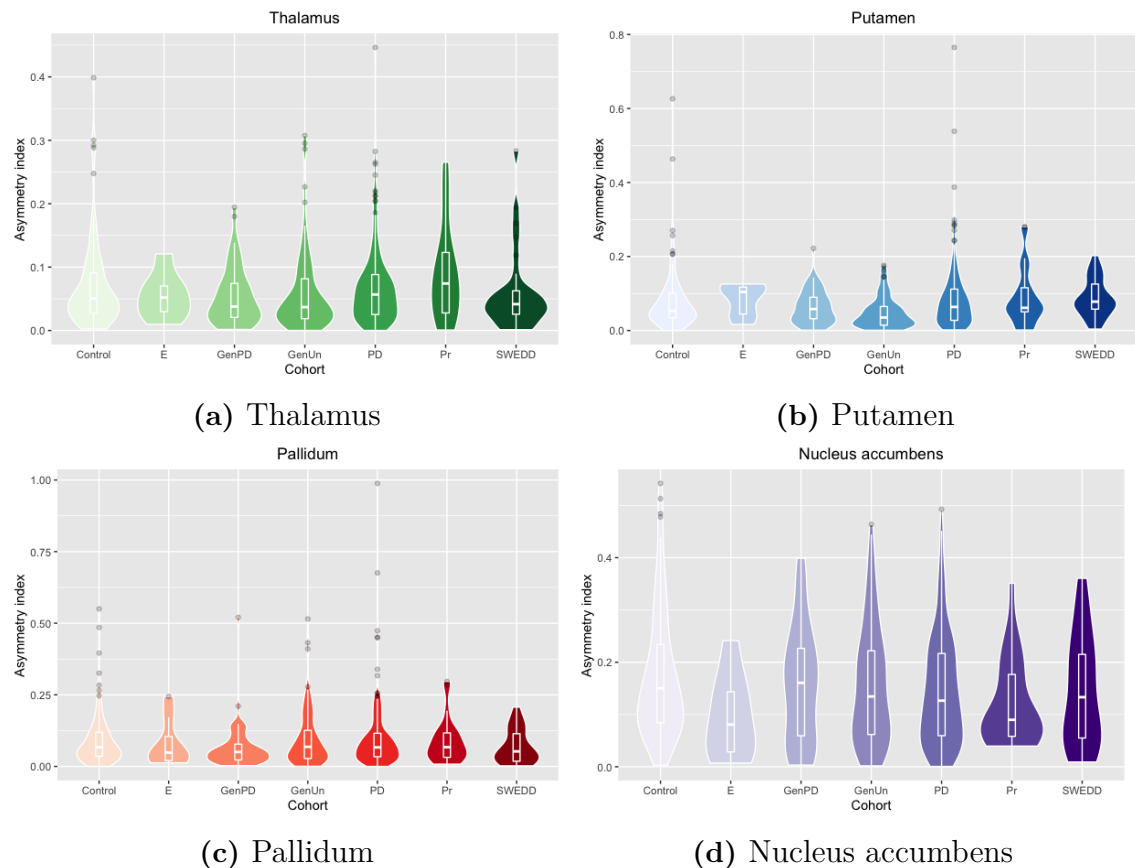


Figure 4.15: Asymmetry index for selected regions

Thalamus

The asymmetry indexes generated for *Thalamus* can be found in Figure 4.15a. One can notice from the figure that the asymmetry index is relatively small for *Thalamus* compared to the other regions in the figure, which implies that the difference between the left and right regions is much similar. As can be seen in Table 4.19, the mean value for the asymmetry index is 0.0718 for the control group, and the cohort that differs the most from the control is the GenPD group with a lower mean value of 0.0547. The t-tests show no significant difference for any of the cohorts.

Putamen

A visual review of the results for the asymmetry indexes of *Putamen* is found in Figure 4.15b. Table 4.20 provides the results from the t-tests and reveals that the

Table 4.19: Results from the unpaired t-test for Thalamus.

T-test result				
Cohort	H_A :	Control mean	Cohort mean	P-Value
PD	C<PD	0.0718	0.0695	0.7905
SWEDD	C>SWEDD	0.0718	0.0600	0.4016
GenPD	C>GenPD	0.0718	0.0547	0.08629
GenUn	C>GenUn	0.0718	0.0602	0.2626
Pr	C>Pr	0.0718	0.0930	0.2398
E	C>E	0.0718	0.0550	0.2795
Benjamini-Hochberg procedure				
Cohort	P-value	Rank	p^{BH}	Reject the null hypothesis
GenPD	0.08629	1	0.008	X
Pr	0.2398	2	0.017	X
GenUn	0.2626	3	0.025	X
E	0.2795	4	0.033	X
SWEDD	0.4016	5	0.042	X
PD	0.7905	6	0.050	X

Note: H_A = Alternative hypotheses generated in the exploratory part.

GenUn cohort is the only cohort that has a significant different asymmetry index from the controls and suggests that the volume of the left and right *Putamen* differs less than it does for the control group.

Table 4.20: Results from the unpaired t-test for Putamen.

T-test result				
Cohort	H_A :	Control mean	Cohort mean	P-Value
PD	C<PD	0.0819	0.0853	0.7711
SWEDD	C>SWEDD	0.0819	0.0865	0.7323
GenPD	C>GenPD	0.0819	0.0629	0.1028
GenUn	C>GenUn	0.0819	0.0489	0.002482
Pr	C>Pr	0.0819	0.0914	0.6234
E	C>E	0.0819	0.0838	0.9177
Benjamini-Hochberg procedure				
Cohort	P-value	Rank	p^{BH}	Reject the null hypothesis
GenUn	0.002482	1	0.008	✓
GenPD	0.1028	2	0.017	X
Pr	0.6234	3	0.025	X
SWEDD	0.7323	4	0.033	X
PD	0.7711	5	0.042	X
E	0.9177	6	0.050	X

Note: H_A = Alternative hypotheses generated in the exploratory part.

Pallidum

A violin plot of *Pallidum* asymmetry indeces is found in Figure 4.15c and one can notice in the figure that the PD cohort have some outliers that differ almost ten times the group mean value. In Table 4.21 we can observe that no cohort had a significant difference in asymmetry index compared to the control group.

Table 4.21: Results from the unpaired t-test for Pallidum.

T-test result				
Cohort	H_A :	Control mean	Cohort mean	P-Value
PD	C<PD	0.0970	0.0978	0.9561
SWEDD	C<SWEDD	0.0970	0.0698	0.07785
GenPD	C<GenPD	0.0970	0.0779	0.05295
GenUn	C<GenUn	0.0970	0.0980	0.9464
Pr	C>Pr	0.0970	0.0903	0.739
E	C<E	0.0970	0.0809	0.6203
Benjamini-Hochberg procedure				
Cohort	P-value	Rank	p^{BH}	Reject the null hypothesis
GenPD	0.05295	1	0.008	X
SWEDD	0.07785	2	0.017	X
E	0.6203	3	0.025	X
Pr	0.739	4	0.033	X
GenUn	0.9464	5	0.042	X
PD	0.9561	6	0.050	X

Note: H_A = Alternative hypotheses generated in the exploratory part.

Nucleus accumbens

A visual distribution of asymmetry indeces for *Nucleus accumbens* between all cohorts is found in Figure 4.15d. By studying the figure, we can observe that the asymmetry indeces is larger and has a more extensive range than previously mentioned regions. The mean value for the control group is 0.1747, more than twice as large as the asymmetry index for *Thalamus*. The cohort Pr and E both receive a p-value less than $<.05$. However, when the significance levels are corrected with the Benjamini-Hochberg procedure, only Pr turns out to show a significant difference compared to the asymmetry indeces of the controls.

Caudate nucleus

The *caudate nucleus* is a region with a relatively small asymmetry, as can be seen in Figure 4.16a. The mean value of the asymmetry index for the control group is 0.0528, and a cohort that was striking out, as seen in Table 4.23, was Pr with a mean value of 0.0932 ($p<.05$). However, when adjusting the significant levels with the Benjamini-Hochberg procedure, Pr was not considered significant since ($p>0.008$).

Table 4.22: Results from the unpaired t-test for Nucleus accumbens.

T-test result				
Cohort	H_A :	Control mean	Cohort mean	P-Value
PD	C<PD	0.1747	0.1473	0.07232
SWEDD	C<SWEDD	0.1747	0.1440	0.1949
GenPD	C<GenPD	0.1747	0.1576	0.4004
GenUn	C<GenUn	0.1747	0.1576	0.3424
Pr	C>Pr	0.1747	0.1215	0.01846
E	C<E	0.1747	0.0956	0.02992
Benjamini-Hochberg procedure				
Cohort	P-value	Rank	p^{BH}	Reject the null hypothesis
Pr	0.01846	1	0.008	X
E	0.02992	2	0.017	X
PD	0.07232	3	0.025	X
SWEDD	0.1949	4	0.033	X
GenUn	0.3424	5	0.042	X
GenPD	0.4004	6	0.050	X

Note: H_A = Alternative hypotheses generated in the exploratory part.

Table 4.23: Results from the unpaired t-test for Caudate nucleus.

T-test result				
Cohort	H_A :	Control mean	Cohort mean	P-Value
PD	C<PD	0.0528	0.0617	0.2246
SWEDD	C<SWEDD	0.0528	0.0529	0.9915
GenPD	C<GenPD	0.0528	0.0569	0.7025
GenUn	C<GenUn	0.0528	0.0406	0.06612
Pr	C<Pr	0.0528	0.0932	0.02386
E	C<E	0.0528	0.0630	0.6329
Benjamini-Hochberg procedure				
Cohort	P-value	Rank	p^{BH}	Reject the null hypothesis
Pr	0.02386	1	0.008	X
GenUn	0.06612	2	0.017	X
PD	0.2246	3	0.025	X
E	0.6329	4	0.033	X
GenPD	0.7025	5	0.042	X
SWEDD	0.9915	6	0.050	X

Note: H_A = Alternative hypotheses generated in the exploratory part.

Substantia nigra

A violin plot with asymmetry indexes for *Substantia nigra* for the cohorts is found in Table 4.16b. As one can observe in Table 4.24, no cohort had a p-value indicating

4. Results

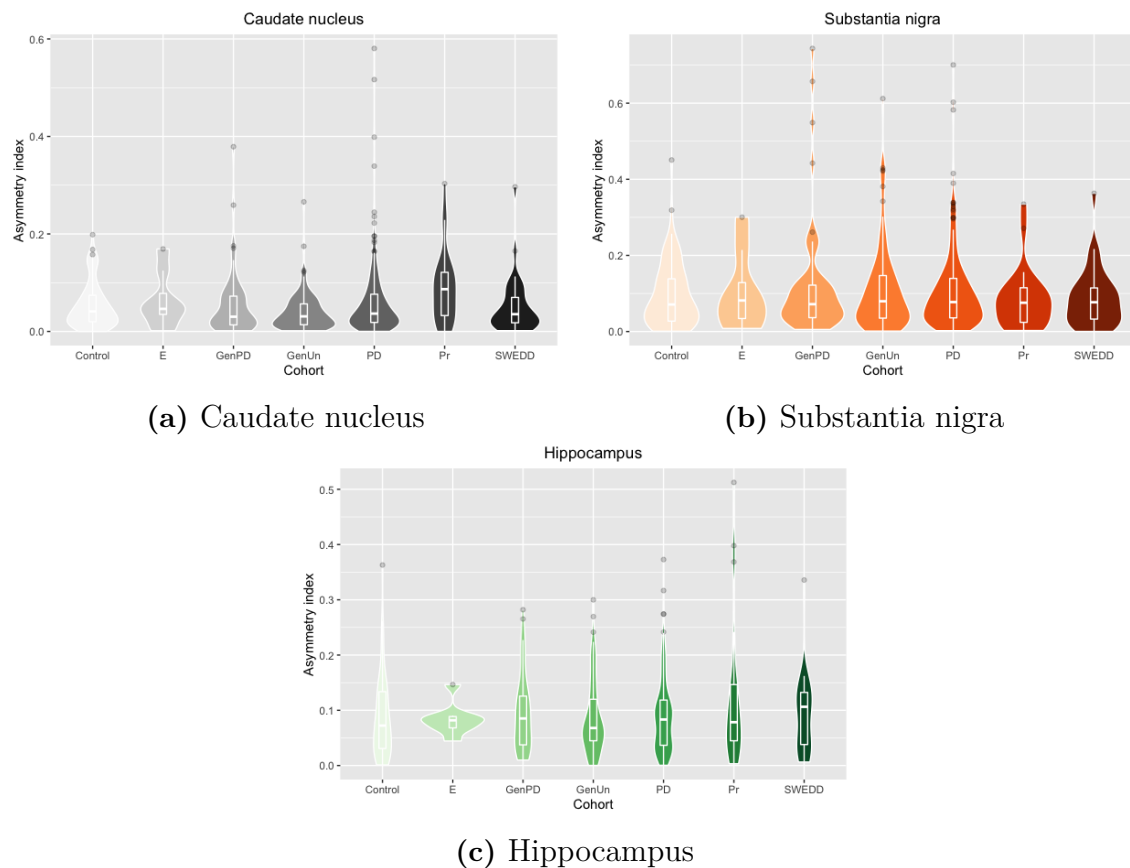


Figure 4.16: Asymmetry index for selected regions

a significant difference in asymmetry compared to the control group.

Hippocampus

The distribution of the asymmetry indices for *Hippocampus* in the cohorts is found in Figure 4.16c. Studying Table 4.25, one can observe that, likewise the result for *Substantia nigra*, no cohort had a significant difference in comparison to the control group.

Table 4.24: Results from the unpaired t-test for Substantia nigra.

T-test result				
Cohort	H_A :	Control mean	Cohort mean	P-Value
PD	C>PD	0.0962	0.1073	0.343
SWEDD	C<SWEDD	0.0962	0.0894	0.6865
GenPD	C<GenPD	0.0962	0.1255	0.2178
GenUn	C>GenUn	0.0962	0.1118	0.3076
Pr	C<Pr	0.0962	0.0877	0.6672
E	C>E	0.0962	0.1048	0.8246
Benjamini-Hochberg procedure				
Cohort	P-value	Rank	p^{BH}	Reject the null hypothesis
GenPD	0.2178	1	0.008	X
GenUn	0.3076	2	0.017	X
PD	0.343	3	0.025	X
Pr	0.6672	4	0.033	X
SWEDD	0.6865	5	0.042	X
E	0.8246	6	0.050	X

Note: H_A = Alternative hypotheses generated in the exploratory part.

Table 4.25: Results from the unpaired t-test for Hippocampus.

T-test result				
Cohort	H_A :	Control mean	Cohort mean	P-Value
PD	C<PD	0.0855	0.0906	0.568
SWEDD	C<SWEDD	0.0855	0.0902	0.7486
GenPD	C<GenPD	0.0855	0.0977	0.3226
GenUn	C<GenUn	0.0855	0.0878	0.8265
Pr	C<Pr	0.0855	0.1270	0.1617
E	C<E	0.0855	0.0835	0.8782
Benjamini-Hochberg procedure				
Cohort	P-value	Rank	p^{BH}	Reject the null hypothesis
Pr	0.1617	1	0.008	X
GenPD	0.3226	2	0.017	X
PD	0.568	3	0.025	X
SWEDD	0.7486	4	0.033	X
GenUn	0.8265	5	0.042	X
E	0.8782	6	0.050	X

Note: H_A = Alternative hypotheses generated in the exploratory part.

4.5 Key findings

ICV and Difference index between ICV and parenchyma

- Table 4.4 indicates that there was a significant difference in ICV between the control and PD, Pr and E. PD, Pr and E had all a larger ICV volume compared to the control group.
- Table 4.5 shows that there were a greater difference between the ICV and parenchyma volume for Pr and GenUn compared to the control group.

Individual regional volume

- No cohort showed a significant difference in **Thalamus** volume compared to the control group, as seen in Table 4.12.
- No cohort showed a significant difference in **Putamen** volume compared to the control group, as seen in Table 4.7. Although, Pr received a p-value of .008458, which is relatively small and the False Discovery rate of 0.05 could be considered as a bit to strict.
- The results in Table 4.8 suggests that the volume of **Pallidum** is greater in the SWEDD cohort compared to the controls, and that the **Pallidum** volume is less in the PD and GenUn cohort compared to the control group.
- Evidence that the **Nucleus accumbens** volume is larger for the GenUn cohort compared to the control group is found in Table 4.9
- No cohort showed a significant difference in **Caudate nucleus** volume compared to the control group, as seen in Table 4.9.
- The result in Table 4.11 suggests that the volume of **Substantia nigra** is smaller for the GenUn and Pr cohort compared to the control group.
- No cohort showed a significant difference in **Hippocampus** volume compared to the control group, as seen in Table 4.12
- As seen in Table 4.17, 4.16 and 4.15, GenPD, GenUn and Pr have significantly smaller volume of **TL middle and inferior temporal gyrus** compared to the control group.
- As can be seen in Table 4.17, **TL posterior temporal lobe** are significantly smaller in the GenPD group compared to the control group.
- For the GenUn cohort, **TL anterior temporal lobe medial part** is found to be significantly smaller than for the control group, as seen in Table 4.16

Asymmetry

- GenUn showed a significant difference in asymmetry index in **Putamen** compared to the control, see Table 4.20. The result suggest that the asymmetry between left and right Putamen is smaller for the GenUn, compared to the controls.

5

Discussion

This is the first study that uses region-based morphometry on a large cohort study of Parkinson's disease. While there was insufficient morphometric evidence for the hypothesised link between PD and epilepsy, the analysis revealed several unexpected characteristics of the various groups defined in the PPMI study. The split exploration/testing design ensured that group differences I observed to be significant are true morphometric correlates of the respective study groups' conditions. These will be interesting to explore and interpret in future work.

5.1 Intracranial volume

One of the aims of this study was to investigate differences in ICV between the study cohorts and the controls. I found that participants in the PD cohort had a larger intracranial volume (3.8%) compared to the control group ($p=0.005316$). This finding is consistent with that of Krabbe et al. [10]. Moreover, I found that the epilepsy participants (E) and the Pr cohort showed significantly larger intracranial volume than the control group ($p=0.02486$, $p=0.02481$).

5.2 Difference between ICV and parenchyma

The DI was higher in Pr and GenUn participants than in the control group ($p=0.0004239$, $p=0.01674$). This indicates that persons with prodromal PD or a risk of developing PD may be affected by subclinical brain atrophy, a finding that warrants further study.

5.3 Individual regional volume

PD

This study showed that the volume of *Pallidum* was significantly larger for the PD cohort than for the controls ($p=0.003634$).

Contrary to expectations ([9], [8]), this study did not find a significant difference in *Caudate nucleus* between the PD cohort and controls ($p=0.8624$).

As for the *Caudate nucleus*, no significant difference was found in *Thalamus* volume between de novo PD and control participants, which was suggested by Lee et al. [9].

In contrast to earlier findings, this study shows that the volume of *Putamen* did not show any significant difference between de novo PD participants compared to the controls, which was suggested by Pitcher et al. [8].

In conclusion, this experiment did not detect any evidence for significant differences between the de novo PD participants and the controls in any other regions except *Pallidum*.

SWEDD

Unlike the finding for the de novo PD participants, this study showed that the volume of *Pallidum* is greater in SWEDD participants compared to the controls ($p=0.0005336$).

Epilepsy

Contrary to expectations [12]–[14], I found relatively few epilepsy participants in the PPMI data. The epilepsy cohort was relatively small compared to the other cohorts, and the inclusion criterion for epilepsy participants in this study is not as established as in the other cohorts. In addition, I was not able to gather information about which side of the brain the epilepsy seizures occurred, and thereby, I could not compare our study with the findings found by Keihaninejad et al. [11]. I did not find any significant findings between the epilepsy participants in any of the individual region volumes.

Pr, GenUn and GenPD

One surprising region that was found to be significantly associated with GenPD, GenUn and Pr was *TL middle and inferior temporal gyrus*. All of the three regions had a smaller volume of *TL middle and inferior temporal gyrus* (4.5-6.5 % smaller) compared to the controls ($p=0.0007463$, $p=6.896e-08$, $p=0.000746$).

In addition, both Pr and GenUn showed a significantly smaller volume of *Substantia nigra* ($p=0.01563$ and $p=0.0002748$).

In this thesis, I showed that *TL anterior temporal lobe lateral* were significantly smaller in GenPD participants ($p=0.021$) compared to the control and that *TL anterior temporal lobe medial part* was significantly smaller in GenUn participants compared to the controls ($p=3.805e-05$). Interestingly, when I investigated the exploratory results, GenPD indicated a large difference from the control in *TL anterior temporal lobe medial part*, and GenUn indicated a large difference compared to the control in *TL anterior temporal lobe lateral*. However, since I chose to pick only two regions in each cohort, I did not test whether those two hypotheses were significant.

Both GenUn and GenPD participants commonly have a genetic mutation in LRRK2,

GBA, or SNCA. The common observations above raise the question if a PD genetic mutation might be associated with hyposmia or REM sleep behaviour disorder (the Pr cohort). Moreover, the genetic mutation might be coupled to *Substantia nigra* and regions within the temporal lobe. This is a question that could be of interest to investigate in future analysis.

When looking at the individual cohorts, we saw that the GenUn cohort showed a significant difference from the controls in the regions *Pallidum* and *Nucleus accumbens* ($p=0.001593$, $p=0.0001501$). The GenUn cohort showed the overall most significant difference compared to the control group when looking at all results.

The Pr cohort showed a significant difference in *Putamen* volume compared to the controls ($p=0.008458$). However, correcting the significance level with the Benjamini Hochberg procedure does not allow rejection of the null hypotheses according to the definition ($p>0.0083$).

5.4 Asymmetry

One of the aims of this study was to investigate whether there was a difference in asymmetry index between the cohorts and controls in any of the predetermined regions. I found that the *Putamen* is more symmetrical in the GenUn cohort than the controls ($p=0.002482$).

6

Conclusion

This large-cohort morphometry study on Parkinson's disease confirms previous results regarding intracranial volume, which was found to be larger in patients than in controls. As a novel finding warranting further study, I was able to show involvement of the Pallidum in PD. Some previously described correlates of PD (in the Thalamus, Putamen, and Caudata nucleus) could not be confirmed on this large cohort.

Evidence from this study suggests that there might be a coupling between a PD genetic mutation and hyposmia or REM sleep behaviour disorder associated with the region *Substantia nigra* and regions within the temporal lobe (*TL middle and inferior temporal gyrus*, *TL anterior temporal lobe medial part* and *TL anterior temporal lobe lateral*). Further investigation of the association of these factors in future studies is warranted.

I have also shown that epilepsy participants had a significantly larger ICV compared to the controls. Except for the finding on intracranial volume, I did not find evidence supporting the hypothesised volume differences between the epilepsy participants in any of the individual region volumes.

Bibliography

- [1] O.-B. Tysnes and A. Storstein, “Epidemiology of parkinson’s disease,” *Journal of Neural Transmission*, vol. 124, no. 8, pp. 901–905, Aug. 1, 2017, ISSN: 1435-1463. DOI: 10.1007/s00702-017-1686-y. [Online]. Available: <https://doi.org/10.1007/s00702-017-1686-y> (visited on 04/19/2021).
- [2] E. R. Dorsey, A. Elbaz, E. Nichols, F. Abd-Allah, A. Abdelalim, J. C. Adsuar, M. G. Ansha, C. Brayne, J.-Y. J. Choi, D. Collado-Mateo, N. Dahodwala, H. P. Do, D. Edessa, M. Endres, S.-M. Fereshtehnejad, K. J. Foreman, F. G. Gankpe, R. Gupta, G. J. Hankey, S. I. Hay, M. I. Hegazy, D. T. Hibstu, A. Kasaeian, Y. Khader, I. Khalil, Y.-H. Khang, Y. J. Kim, Y. Kokubo, G. Logroscino, J. Massano, N. Mohamed Ibrahim, M. A. Mohammed, A. Mohammadi, M. Moradi-Lakeh, M. Naghavi, B. T. Nguyen, Y. L. Nirayo, F. A. Ogbo, M. O. Owolabi, D. M. Pereira, M. J. Postma, M. Qorbani, M. A. Rahman, K. T. Roba, H. Safari, S. Safiri, M. Satpathy, M. Sawhney, A. Shafieesabet, M. S. Shiferaw, M. Smith, C. E. I. Szoeki, R. Tabarés-Seisdedos, N. T. Truong, K. N. Ukwaja, N. Venketasubramanian, S. Villafaina, K. g. weldegwergs, R. Westerman, T. Wijeratne, A. S. Winkler, B. T. Xuan, N. Yonemoto, V. L. Feigin, T. Vos, and C. J. L. Murray, “Global, regional, and national burden of parkinson’s disease, 1990–2016: A systematic analysis for the global burden of disease study 2016,” *The Lancet Neurology*, vol. 17, no. 11, pp. 939–953, Nov. 2018, ISSN: 14744422. DOI: 10.1016/S1474-4422(18)30295-3. [Online]. Available: <https://linkinghub.elsevier.com/retrieve/pii/S1474442218302953> (visited on 04/16/2021).
- [3] (). “Estimation of the 2020 global population of parkinson’s disease (PD),” MDS Abstracts, [Online]. Available: <https://www.mdsabstracts.org/abstract/estimation-of-the-2020-global-population-of-parkinsons-disease-pd/> (visited on 04/18/2021).
- [4] (). “Statistics,” Parkinson’s Foundation, [Online]. Available: <https://www.parkinson.org/Understanding-Parkinsons/Statistics> (visited on 01/28/2021).
- [5] E. Tolosa, G. Wenning, and W. Poewe, “The diagnosis of parkinson’s disease,” *The Lancet Neurology*, vol. 5, no. 1, pp. 75–86, Jan. 1, 2006, ISSN: 1474-4422. DOI: 10.1016/S1474-4422(05)70285-4. [Online]. Available: <https://www.sciencedirect.com/science/article/pii/S1474442205702854> (visited on 04/19/2021).

- [6] K. Bhatia, K. R. Chaudhuri, and M. Stamelou, *Parkinson's Disease*. San Diego, UNITED STATES: Elsevier Science & Technology, 2017, ISBN: 978-0-12-809850-9. [Online]. Available: <http://ebookcentral.proquest.com/lib/chalmers/detail.action?docID=4866642> (visited on 04/19/2021).
- [7] M. Tamari and H. Utsunomiya, "Evaluation of substantia nigra volume of patients with parkinson's disease using 3-dimensional neuromelanin images," *International Journal of Physical Medicine & Rehabilitation*, vol. 06, no. 5, 2018, ISSN: 23299096. DOI: 10.4172/2329-9096.1000486. [Online]. Available: <https://www.omicsonline.org/open-access/evaluation-of-substantia-nigra-volume-of-patients-with-parkinsons-disease-using-3dimensional-neuromelanin-images-2329-9096-1000488-105839.html> (visited on 08/26/2021).
- [8] T. L. Pitcher, T. R. Melzer, M. R. Macaskill, C. F. Graham, L. Livingston, R. J. Keenan, R. Watts, J. C. Dalrymple-Alford, and T. J. Anderson, "Reduced striatal volumes in parkinson's disease: A magnetic resonance imaging study," *Translational Neurodegeneration*, vol. 1, no. 1, p. 17, Aug. 21, 2012, ISSN: 2047-9158. DOI: 10.1186/2047-9158-1-17.
- [9] S. H. Lee, S. S. Kim, W. S. Tae, S. Y. Lee, J. W. Choi, S. B. Koh, and D. Y. Kwon, "Regional volume analysis of the parkinson disease brain in early disease stage: Gray matter, white matter, striatum, and thalamus," *American Journal of Neuroradiology*, vol. 32, no. 4, pp. 682–687, Apr. 1, 2011, Publisher: American Journal of Neuroradiology Section: Brain, ISSN: 0195-6108, 1936-959X. DOI: 10.3174/ajnr.A2372. [Online]. Available: <http://www.ajnr.org/content/32/4/682> (visited on 08/26/2021).
- [10] K. Krabbe, M. Karlsborg, A. Hansen, L. Werdelin, J. Mehlsen, H. B. W. Larsson, and O. B. Paulson, "Increased intracranial volume in parkinson's disease," *Journal of the Neurological Sciences*, vol. 239, no. 1, pp. 45–52, Dec. 15, 2005, ISSN: 0022-510X. DOI: 10.1016/j.jns.2005.07.013. [Online]. Available: <https://www.sciencedirect.com/science/article/pii/S0022510X05002698> (visited on 08/26/2021).
- [11] S. Keihaninejad, R. A. Heckemann, I. S. Gousias, J. V. Hajnal, J. S. Duncan, P. Aljabar, D. Rueckert, and A. Hammers, "Classification and lateralization of temporal lobe epilepsies with and without hippocampal atrophy based on whole-brain automatic MRI segmentation," *PLOS ONE*, vol. 7, no. 4, e33096, Apr. 2012, Publisher: Public Library of Science, ISSN: 1932-6203. DOI: 10.1371/journal.pone.0033096. [Online]. Available: <https://journals.plos.org/plosone/article?id=10.1371/journal.pone.0033096> (visited on 09/01/2021).
- [12] K. Gruntz, M. Bloechliger, C. Becker, S. S. Jick, P. Fuhr, C. R. Meier, and S. Rüegg, "Parkinson disease and the risk of epileptic seizures.," *Annals of neurology*, vol. 83, no. 2, pp. 363–374, Feb. 2018, Place: United States Publisher: Wiley-Liss, ISSN: 1531-8249. DOI: 10.1002/ana.25157. [Online]. Available: <https://search.ebscohost.com/login.aspx?direct=true&db=cmedm&AN=29369409&site=eds-live&scope=site&authtype=guest&custid=s3911979&groupid=main&profile=eds>.

-
- [13] P. I. Yakovlev, "EPILEPSY AND PARKINSONISM," *The Journal of Nervous and Mental Disease*, vol. 67, no. 3, pp. 261–274, Mar. 1928, ISSN: 0022-3018. [Online]. Available: https://journals.lww.com/jonmd/Citation/1928/03000/Epilepsy_and_Parkinsonism.4.aspx (visited on 04/19/2021).
- [14] B. Feddersen, J. Rémi, M. Einhellig, C. Stoyke, P. Krauss, and S. Noachtar, "Parkinson's disease: Less epileptic seizures more status epilepticus," *Epilepsy Research*, vol. 108, no. 2, pp. 349–354, Feb. 1, 2014, ISSN: 0920-1211. DOI: 10.1016/j.eplepsyres.2013.11.013. [Online]. Available: <https://www.sciencedirect.com/science/article/pii/S0920121113002970> (visited on 04/19/2021).
- [15] (). "Parkinson's progression markers initiative |," [Online]. Available: <https://www.ppmi-info.org/> (visited on 01/28/2021).
- [16] K. Marek, D. Jennings, S. Lasch, A. Siderowf, C. Tanner, T. Simuni, C. Coffey, K. Kieburtz, E. Flagg, S. Chowdhury, W. Poewe, B. Mollenhauer, P.-E. Kleinik, T. Sherer, M. Frasier, C. Meunier, A. Rudolph, C. Casaceli, J. Seibyl, S. Mendick, N. Schuff, Y. Zhang, A. Toga, K. Crawford, A. Ansbach, P. De Blasio, M. Piovela, J. Trojanowski, L. Shaw, A. Singleton, K. Hawkins, J. Eberling, D. Brooks, D. Russell, L. Leary, S. Factor, B. Sommerfeld, P. Hogarth, E. Pighetti, K. Williams, D. Standaert, S. Guthrie, R. Hauser, H. Delgado, J. Jankovic, C. Hunter, M. Stern, B. Tran, J. Leverenz, M. Baca, S. Frank, C.-A. Thomas, I. Richard, C. Deeley, L. Rees, F. Sprenger, E. Lang, H. Shill, S. Obradov, H. Fernandez, A. Winters, D. Berg, K. Gauss, D. Galasko, D. Fontaine, Z. Mari, M. Gerstenhaber, D. Brooks, S. Malloy, P. Barone, K. Longo, T. Comery, B. Ravina, I. Grachev, K. Gallagher, M. Collins, K. L. Widnell, S. Ostrowizki, P. Fontoura, T. Ho, J. Luthman, M. v. d. Brug, A. D. Reith, and P. Taylor, "The parkinson progression marker initiative (PPMI)," *Progress in Neurobiology*, Biological Markers for Neurodegenerative Diseases, vol. 95, no. 4, pp. 629–635, Dec. 1, 2011, ISSN: 0301-0082. DOI: 10.1016/j.pneurobio.2011.09.005. [Online]. Available: <https://www.sciencedirect.com/science/article/pii/S0301008211001651> (visited on 04/19/2021).
- [17] H. T. C. M. Officer. (). "PPMI needs people at risk for parkinson's — even if not diagnosed with PD | parkinson's disease," [Online]. Available: <https://www.michaeljfox.org/news/ppmi-needs-people-risk-parkinsons-even-if-not-diagnosed-pd> (visited on 04/19/2021).
- [18] R. A. Heckemann, S. Keihaninejad, P. Aljabar, K. R. Gray, C. Nielsen, D. Rueckert, J. V. Hajnal, and A. Hammers, "Automatic morphometry in alzheimer's disease and mild cognitive impairment," *NeuroImage*, vol. 56, no. 4, pp. 2024–2037, Jun. 15, 2011, ISSN: 1053-8119. DOI: 10.1016/j.neuroimage.2011.03.014. [Online]. Available: <https://www.sciencedirect.com/science/article/pii/S1053811911002734> (visited on 04/21/2021).
- [19] M. O. Holmberg, H. Malmgren, P. Berglund, L. Bunketorp-Käll, R. A. Heckemann, B. Johansson, N. Klasson, E. Olsson, S. Skau, and H. Nystrom Filipsson, "Structural brain changes in hyperthyroid graves' disease: Protocol for an ongoing longitudinal, case-controlled study in göteborg, sweden-the CogThy

- project.,” *BMJ open*, vol. 9, no. 11, e031168, Nov. 3, 2019, Place: England Publisher: BMJ Publishing Group Ltd, ISSN: 2044-6055. DOI: 10.1136/bmjopen-2019-031168. [Online]. Available: <https://search.ebscohost.com/login.aspx?direct=true&db=cmedm&AN=31685507&site=eds-live&scope=site&authtype=guest&custid=s3911979&groupid=main&profile=eds>.
- [20] C. Ledig, A. Schuh, R. Guerrero, R. A. Heckemann, and D. Rueckert, “Structural brain imaging in alzheimer’s disease and mild cognitive impairment: Biomarker analysis and shared morphometry database,” *Scientific Reports*, vol. 8, no. 1, p. 11 258, Dec. 2018, ISSN: 2045-2322. DOI: 10.1038/s41598-018-29295-9. [Online]. Available: <http://www.nature.com/articles/s41598-018-29295-9> (visited on 01/28/2021).
- [21] S. Siuly and Y. Zhang, “Medical big data: Neurological diseases diagnosis through medical data analysis,” *Data Science and Engineering*, vol. 1, no. 2, pp. 54–64, Jun. 1, 2016, ISSN: 2364-1541. DOI: 10.1007/s41019-016-0011-3. [Online]. Available: <https://doi.org/10.1007/s41019-016-0011-3> (visited on 01/25/2021).
- [22] R. A. Heckemann, S. Keihaninejad, P. Aljabar, D. Rueckert, J. V. Hajnal, and A. Hammers, “Improving intersubject image registration using tissue-class information benefits robustness and accuracy of multi-atlas based anatomical segmentation,” *NeuroImage*, vol. 51, no. 1, pp. 221–227, May 15, 2010, Publisher: Elsevier Inc., ISSN: 1053-8119. [Online]. Available: <https://search.ebscohost.com/login.aspx?direct=true&db=edselp&AN=S1053811910000947&site=eds-live&scope=site&authtype=guest&custid=s3911979&groupid=main&profile=eds>.
- [23] X. Jia, P. Liang, Y. Li, L. Shi, D. Wang, and K. Li, “Longitudinal study of gray matter changes in parkinson disease,” *AJNR. American journal of neuroradiology*, vol. 36, no. 12, pp. 2219–2226, Dec. 2015, ISSN: 1936-959X. DOI: 10.3174/ajnr.A4447.
- [24] S. Boucetta, A. Salimi, M. Dadar, B. E. Jones, D. L. Collins, and T. T. Dang-Vu, “Structural brain alterations associated with rapid eye movement sleep behavior disorder in parkinson’s disease,” *Scientific Reports*, vol. 6, Jun. 1, 2016, ISSN: 2045-2322. DOI: 10.1038/srep26782. [Online]. Available: <https://www.ncbi.nlm.nih.gov/pmc/articles/PMC4887790/> (visited on 04/19/2021).
- [25] G. Pahuja and T. N. Nagabhushan, “A novel GA-ELM approach for parkinson’s disease detection using brain structural t1-weighted MRI data,” in *2016 Second International Conference on Cognitive Computing and Information Processing (CCIP)*, Aug. 2016, pp. 1–6. DOI: 10.1109/CCIP.2016.7802848.
- [26] A. Garg, S. Appel-Cresswell, K. Popuri, M. J. McKeown, and M. F. Beg, “Morphological alterations in the caudate, putamen, pallidum, and thalamus in parkinson’s disease,” *Frontiers in Neuroscience*, vol. 9, p. 101, 2015, ISSN: 1662-4548. DOI: 10.3389/fnins.2015.00101.
- [27] J. T. Bushberg, J. A. Seibert, E. M. Leidholdt, and J. M. Boone, *The Essential Physics of Medical Imaging*. Lippincott Williams & Wilkins, Dec. 28, 2011, 1049 pp., Google-Books-ID: RKcTgTqeniwC, ISBN: 978-1-4511-5394-1.

-
- [28] J. Peters and M. Ylitalo, “Magnetisk resonanstomografi,” Ph.D. dissertation, 2006. [Online]. Available: <http://urn.kb.se/resolve?urn=urn:nbn:se:ltu:diva-51990> (visited on 03/03/2021).
- [29] A. A. Farag, *Biomedical Image Analysis: Statistical and Variational Methods*. Cambridge: Cambridge University Press, 2014, ISBN: 978-0-521-19679-6. DOI: 10.1017/CB09781139022675. [Online]. Available: <https://www.cambridge.org/core/books/biomedical-image-analysis/89DF903AB940A2EC8F2C09E89078D4DF> (visited on 03/03/2021).
- [30] S. Abdullah. (). “T1, t2 and PD weighted imaging,” Radiology Cafe, [Online]. Available: <https://www.radiologycafe.com/radiology-trainees/frcr-physics-notes/t1-t2-and-pd-weighted-imaging> (visited on 04/26/2021).
- [31] J. G. Sled, A. P. Zijdenbos, and A. C. Evans, “A nonparametric method for automatic correction of intensity nonuniformity in MRI data,” *IEEE transactions on medical imaging*, vol. 17, no. 1, pp. 87–97, Feb. 1998, ISSN: 0278-0062. DOI: 10.1109/42.668698.
- [32] N. J. Tustison, B. B. Avants, P. A. Cook, Yuanjie Zheng, A. Egan, P. A. Yushkevich, and J. C. Gee, “N4itk: Improved n3 bias correction,” *IEEE Transactions on Medical Imaging*, vol. 29, no. 6, pp. 1310–1320, Jun. 2010, ISSN: 0278-0062, 1558-254X. DOI: 10.1109/TMI.2010.2046908. [Online]. Available: <http://ieeexplore.ieee.org/document/5445030/> (visited on 04/21/2021).
- [33] J. Swiebocka-Wiek, “Skull stripping for MRI images using morphological operators,” in *Computer Information Systems and Industrial Management*, K. Saeed and W. Homenda, Eds., ser. Lecture Notes in Computer Science, Cham: Springer International Publishing, 2016, pp. 172–182, ISBN: 978-3-319-45378-1. DOI: 10.1007/978-3-319-45378-1_16.
- [34] P. Kalavathi and V. B. S. Prasath, “Methods on skull stripping of MRI head scan images—a review,” *Journal of Digital Imaging*, vol. 29, no. 3, pp. 365–379, Jun. 2016, ISSN: 0897-1889. DOI: 10.1007/s10278-015-9847-8. [Online]. Available: <https://www.ncbi.nlm.nih.gov/pmc/articles/PMC4879034/> (visited on 03/03/2021).
- [35] A. M. Winkler. (Sep. 23, 2012). “The NIFTI file format,” Brainder. [Online]. Available: <https://brainder.org/2012/09/23/the-nifti-file-format/> (visited on 03/24/2021).
- [36] V. Vadmal, G. Junno, C. Badve, W. Huang, K. A. Waite, and J. S. Barnholtz-Sloan, “MRI image analysis methods and applications: An algorithmic perspective using brain tumors as an exemplar,” *Neuro-Oncology Advances*, vol. 2, no. 1, Jan. 1, 2020, ISSN: 2632-2498. DOI: 10.1093/noajnl/vdaa049. [Online]. Available: <https://doi.org/10.1093/noajnl/vdaa049> (visited on 08/30/2021).
- [37] N. Kumar and M. Nachamai, “Noise removal and filtering techniques used in medical images,” *Oriental Journal of Computer Science and Technology*, vol. 10, no. 1, pp. 103–113, [Online]. Available: <http://www.computerscijournal.org/vol10no1/noise-removal-and-filtering-techniques-used-in-medical-images/> (visited on 08/30/2021).

- [38] D. Rueckert and J. A. Schnabel, "Medical image registration," in *Biomedical Image Processing*, ser. Biological and Medical Physics, Biomedical Engineering, T. M. Deserno, Ed., Berlin, Heidelberg: Springer, 2011, pp. 131–154, ISBN: 978-3-642-15816-2. DOI: 10.1007/978-3-642-15816-2_5. [Online]. Available: https://doi.org/10.1007/978-3-642-15816-2_5 (visited on 03/03/2021).
- [39] E. Golkar, A. A. A. Rahni, and R. Sulaiman, "Comparison of image registration similarity measures for an abdominal organ segmentation framework," in *2014 IEEE Conference on Biomedical Engineering and Sciences (IECBES)*, Dec. 2014, pp. 442–445. DOI: 10.1109/IECBES.2014.7047538.
- [40] T. W. Sederberg, "Free-form deformation of solid geometric models," vol. 20, no. 4, p. 10, 1986.
- [41] D. Rueckert, L. I. Sonoda, C. Hayes, D. L. Hill, M. O. Leach, and D. J. Hawkes, "Nonrigid registration using free-form deformations: Application to breast MR images," *IEEE transactions on medical imaging*, vol. 18, no. 8, pp. 712–721, Aug. 1999, ISSN: 0278-0062. DOI: 10.1109/42.796284.
- [42] K.-P. Wong, "Medical image segmentation: Methods and applications in functional imaging," in *Handbook of Biomedical Image Analysis: Volume II: Segmentation Models Part B*, ser. Topics in Biomedical Engineering International Book Series, J. S. Suri, D. L. Wilson, and S. Laxminarayan, Eds., Boston, MA: Springer US, 2005, pp. 111–182, ISBN: 978-0-306-48606-7. DOI: 10.1007/0-306-48606-7_3. [Online]. Available: https://doi.org/10.1007/0-306-48606-7_3 (visited on 03/03/2021).
- [43] R. A. Heckemann, J. V. Hajnal, P. Aljabar, D. Rueckert, and A. Hammers, "Automatic anatomical brain MRI segmentation combining label propagation and decision fusion," *NeuroImage*, vol. 33, no. 1, pp. 115–126, Oct. 15, 2006, ISSN: 1053-8119. DOI: 10.1016/j.neuroimage.2006.05.061. [Online]. Available: <https://www.sciencedirect.com/science/article/pii/S1053811906006458> (visited on 09/01/2021).
- [44] Zhou S. Kevin, "11. multiple-atlas segmentation in medical imaging," in *Medical Image Recognition, Segmentation and Parsing - Machine Learning and Multiple Object Approaches*, Journal Abbreviation: Medical Image Recognition, Segmentation and Parsing - Machine Learning and Multiple Object Approaches, Elsevier, Mar. 29, 2016, ISBN: 978-0-12-802676-2. [Online]. Available: <https://search.ebscohost.com/login.aspx?direct=true&AuthType=sso&db=edsknv&AN=edsknv.kt010SLSXG&site=eds-live&scope=site&custid=s3911979&authtype=sso> (visited on 03/03/2021).
- [45] (). "Edit-image — MIRTk," [Online]. Available: <https://mirtk.github.io/commands/edit-image.html> (visited on 04/21/2021).
- [46] R. A. Heckemann, C. Ledig, K. R. Gray, P. Aljabar, D. Rueckert, J. V. Hajnal, and A. Hammers, "Brain extraction using label propagation and group agreement: PinCram," *PLOS ONE*, vol. 10, no. 7, e0129211, Jul. 2015, Publisher: Public Library of Science, ISSN: 1932-6203. DOI: 10.1371/journal.pone.0129211. [Online]. Available: <https://journals.plos.org/plosone/article?id=10.1371/journal.pone.0129211> (visited on 04/20/2021).

-
- [47] A. Hammers, R. Allom, M. J. Koeppe, S. L. Free, R. Myers, L. Lemieux, T. N. Mitchell, D. J. Brooks, and J. S. Duncan, “Three-dimensional maximum probability atlas of the human brain, with particular reference to the temporal lobe,” *Human Brain Mapping*, vol. 19, no. 4, pp. 224–247, Aug. 2003, ISSN: 1065-9471, 1097-0193. DOI: 10.1002/hbm.10123. [Online]. Available: <http://doi.wiley.com/10.1002/hbm.10123> (visited on 01/28/2021).
- [48] C. R. Jack, R. C. Petersen, Y. Xu, P. C. O’Brien, G. E. Smith, R. J. Ivnik, E. G. Tangalos, and E. Kokmen, “The rate of medial temporal lobe atrophy in typical aging and alzheimer’s disease,” *Neurology*, vol. 51, no. 4, pp. 993–999, Oct. 1998, ISSN: 0028-3878. [Online]. Available: <https://www.ncbi.nlm.nih.gov/pmc/articles/PMC2768817/> (visited on 08/24/2021).
- [49] Y. Benjamini and Y. Hochberg, “Controlling the false discovery rate: A practical and powerful approach to multiple testing,” *Journal of the Royal Statistical Society: Series B (Methodological)*, vol. 57, no. 1, pp. 289–300, 1995, eprint: <https://rss.onlinelibrary.wiley.com/doi/pdf/10.1111/j.2517-6161.1995.tb02031.x>, ISSN: 2517-6161. DOI: 10.1111/j.2517-6161.1995.tb02031.x. [Online]. Available: <https://rss.onlinelibrary.wiley.com/doi/abs/10.1111/j.2517-6161.1995.tb02031.x> (visited on 08/24/2021).

A

Hypotheses

Table A.1: Summation of hypotheses generated for the intracranial volume.

Region	Description	Notation
PD	The intracranial volume is smaller in the control group compared to the PD group	$H_A:C < PD$
SWEDD	The intracranial volume is larger in the control group compared to the SWEDD group	$H_A:C > SWEDD$
GenPD	The intracranial volume is larger in the control group compared to the GenPD group	$H_A:C > GenPD$
GenUn	The intracranial volume is larger in the control group compared to the GenUn group	$H_A:C > GenUn$
Pr	The intracranial volume is smaller in the control group compared to the Pr group	$H_A:C < Pr$
E	The intracranial volume is smaller in the control group compared to the E group	$H_A:C < E$

Table A.2: Summation of hypotheses generated for DI.

Region	Description	Notation
PD	The difference index is smaller in the control group compared to the PD group	$H_A:C < PD$
SWEDD	The difference index is smaller in the control group compared to the SWEDD group	$H_A:C < SWEDD$
GenPD	The difference index is smaller in the control group compared to the GenPD group	$H_A:C < GenPD$
GenUn	The difference index is smaller in the control group compared to the GenUn group	$H_A:C < GenUn$
Pr	The difference index is smaller in the control group compared to the Pr group	$H_A:C < Pr$
E	The difference index is smaller in the control group compared to the Pr group	$H_A:C < Pr$

Table A.3: Summation of hypotheses generated for individual regions in the PD cohort.

Region	Description	Notation
Thalamus	The mean volume of thalamus is smaller in the control group compared to the PD group	$H_A:C_m < PD_m$
Putamen (L+R)	The mean volume of Putamen is smaller in the control group compared to the PD group	$H_A:C_m < PD_m$
Pallidum (L+R)	The mean volume of Pallidum is larger in the control group compared to the PD group	$H_A:C_m > PD_m$
Nucleus accumbens (L+R)	The mean volume of Nucleus accumbens is smaller in the control group compared to the PD group	$H_A:C_m < PD_m$
Caudate nucleus (L+R)	The mean volume of Caudate nucleus is smaller in the control group compared to the PD group	$H_A:C_m < PD_m$
Substantia nigra (L+R)	The mean volume of Substantia nigra is smaller in the control group compared to the PD group	$H_A:C_m < PD_m$
Hippocampus	The mean volume of Hippocampus is smaller in the control group compared to the PD group	$H_A:C_m < PD_m$
TL posterior temporal lobe	The mean volume of TL posterior temporal lobe is larger in the control group compared to the PD group	$H_A:C_m > PD_m$
Insula middle short gyrus	The mean volume of Insula middle short gyrus is larger in the control group compared to the PD group	$H_A:C_m > PD_m$

Table A.4: Summation of hypotheses generated for individual regions in the SWEDD cohort.

Region	Description	Notation
Thalamus	The mean volume of thalamus is larger in the control group compared to the SWEDD group	$C_m > \text{SWEDD}_m$
Putamen	The mean volume of Putamen is larger in the control group compared to the SWEDD group	$C_m > \text{SWEDD}_m$
Pallidum	The mean volume of Pallidum is smaller in the control group compared to the SWEDD group	$C_m < \text{SWEDD}_m$
Nucleus accumbens	The mean volume of Nucleus accumbens is larger in the control group compared to the SWEDD group	$C_m > \text{SWEDD}_m$
Caudate nucleus	The mean volume of Caudate nucleus is larger in the control group compared to the SWEDD group	$C_m > \text{SWEDD}_m$
Substantia nigra	The mean volume of Substantia nigra is smaller in the control group compared to the SWEDD group	$C_m < \text{SWEDD}_m$
Hippocampus	The mean volume of Hippocampus is larger in the control group compared to the SWEDD group	$C_m > \text{SWEDD}_m$
TL parahippocampal and ambient gyrus	The mean volume of TL parahippocampal and ambient gyrus is smaller in the control group compared to the SWEDD group	$C_m < \text{SWEDD}_m$
OL lateral remainder occipital lobe	The mean volume of OL lateral remainder occipital lobe is larger in the control group compared to the SWEDD group	$C_m > \text{SWEDD}_m$

Table A.5: Summation of hypotheses generated for individual regions in the GenPD cohort.

Region	Description	Notation
Thalamus	The mean volume of thalamus is larger in the control group compared to the GenPD group	$H_A:C_m > \text{GenPD}_m$
Putamen (L+R)	The mean volume of Putamen is larger in the control group compared to the GenPD group	$H_A:C_m > \text{GenPD}_m$
Pallidum (L+R)	The mean volume of Pallidum is smaller in the control group compared to the GenPD group	$H_A:C_m < \text{GenPD}_m$
Nucleus accumbens (L+R)	The mean volume of Nucleus accumbens is smaller in the control group compared to the GenPD group	$H_A:C_m < \text{GenPD}_m$
Caudate nucleus (L+R)	The mean volume of Caudate nucleus is larger in the control group compared to the GenPD group	$H_A:C_m > \text{GenPD}_m$
Substantia nigra (L+R)	The mean volume of Substantia nigra is larger in the control group compared to the GenPD group	$H_A:C_m > \text{GenPD}_m$
Hippocampus	The mean volume of Hippocampus is larger in the control group compared to the GenPD group	$H_A:C_m > \text{GenPD}_m$
TL middle and inferior temporal gyrus	The mean volume of TL middle and inferior temporal gyrus is larger in the control group compared to the GenPD group	$H_A:C_m > \text{GenPD}_m$
TL anterior temporal lobe lateral	The mean volume of TL anterior temporal lobe lateral is larger in the control group compared to the GenPD group	$H_A:C_m > \text{GenPD}_m$

Table A.6: Summation of hypotheses generated for individual regions in the GenUn cohort.

Region	Description	Notation
Thalamus	The mean volume of thalamus is smaller in the control group compared to the GenUn group	$H_A:C_m < \text{GenUn}_m$
Putamen (L+R)	The mean volume of Putamen is smaller in the control group compared to the GenUn group	$H_A:C_m < \text{GenUn}_m$
Pallidum (L+R)	The mean volume of Pallidum is larger in the control group compared to the GenUn group	$H_A:C_m > \text{GenUn}_m$
Nucleus accumbens (L+R)	The mean volume of Nucleus accumbens is smaller in the control group compared to the GenUn group	$H_A:C_m < \text{GenUn}_m$
Caudate nucleus (L+R)	The mean volume of Caudate nucleus is larger in the control group compared to the GenUn group	$H_A:C_m > \text{GenUn}_m$
Substantia nigra (L+R)	The mean volume of Substantia nigra is larger in the control group compared to the GenUn group	$H_A:C_m > \text{GenUn}_m$
Hippocampus	The mean volume of Hippocampus is larger in the control group compared to the GenUn group	$H_A:C_m > \text{GenUn}_m$
TL middle and inferior temporal gyrus	The mean volume of TL middle and inferior temporal gyrus is larger in the control group compared to the GenUn group	$H_A:C_m > \text{GenUn}_m$
TL anterior temporal lobe medial part	The mean volume of TL anterior temporal lobe medial part is larger in the control group compared to the GenUn group	$H_A:C_m > \text{GenUn}_m$

Table A.7: Summation of hypotheses generated for individual regions in the Pr cohort.

Region	Description	Notation
Thalamus	The mean volume of thalamus is larger in the control group compared to the Pr group	$H_A:C_m > Pr_m$
Putamen (L+R)	The mean volume of Putamen is larger in the control group compared to the Pr group	$H_A:C_m > Pr_m$
Pallidum (L+R)	The mean volume of Pallidum is larger in the control group compared to the Pr group	$H_A:C_m > Pr_m$
Nucleus accumbens (L+R)	The mean volume of Nucleus accumbens is larger in the control group compared to the Pr group	$H_A:C_m > Pr_m$
Caudate nucleus (L+R)	The mean volume of Caudate nucleus is larger in the control group compared to the Pr group	$H_A:C_m > Pr_m$
Substantia nigra (L+R)	The mean volume of Substantia nigra is smaller in the control group compared to the Pr group	$H_A:C_m < Pr_m$
Hippocampus	The mean volume of Hippocampus is smaller in the control group compared to the Pr group	$H_A:C_m < Pr_m$
TL posterior temporal lobe	The mean volume of TL posterior temporal lobe is larger in the control group compared to the Pr group	$H_A:C_m > Pr_m$
TL middle and inferior temporal gyrus	The mean volume of TL middle and inferior temporal gyrus is larger in the control group compared to the Pr group	$H_A:C_m > Pr_m$

Table A.8: Summation of hypotheses generated for individual regions in the E cohort.

Region	Description	Notation
Thalamus	The mean volume of thalamus is larger in the control group compared to the E group	$H_A:C_m > E_m$
Putamen (L+R)	The mean volume of Putamen is smaller in the control group compared to the E group	$H_A:C_m < E_m$
Pallidum (L+R)	The mean volume of Pallidum is larger in the control group compared to the E group	$H_A:C_m > E_m$
Nucleus accumbens (L+R)	The mean volume of Nucleus accumbens is larger in the control group compared to the E group	$H_A:C_m > E_m$
Caudate nucleus (L+R)	The mean volume of Caudate nucleus is smaller in the control group compared to the E group	$H_A:C_m < E_m$
Substantia nigra (L+R)	The mean volume of Substantia nigra is larger in the control group compared to the E group	$H_A:C_m > E_m$
Hippocampus	The mean volume of Hippocampus is larger in the control group compared to the E group	$H_A:C_m > E_m$
TL anterior temporal lobe lateral	The mean volume of TL posterior temporal lobe is larger in the control group compared to the E group	$H_A:C_m > E_m$
TL superior temporal gyrus anterior part	The mean volume of TL middle and inferior temporal gyrus is larger in the control group compared to the E group	$H_A:C_m > E_m$

Table A.9: Generated hypothesis (H_A) for asymmetry index.

Cohort	Thalamus	Putamen	Pallidum
PD	C<PD	C<PD	C<PD
SWEDD	C>SWEDD	C<SWEDD	C<SWEDD
GenPD	C>GenPD	C>GenPD	C<GenPD
GenUn	C>GenUn	C>GenUn	C<GenUn
Pr	C>Pr	C>Pr	C>Pr
E	C>E	C>E	C<E
Cohort	Nucleus accumbens	Caudate nucleus	Substantia nigra
PD	C<PD	C<PD	C>PD
SWEDD	C<SWEDD	C<SWEDD	C<SWEDD
GenPD	C<GenPD	C>GenPD	C<GenPD
GenUn	C<GenUn	C>GenUn	C>GenUn
Pr	C>Pr	C<Pr	C<Pr
E	C<E	C<E	C<E
Cohort	Hippocampus		
PD	C<PD		
SWEDD	C<SWEDD		
GenPD	C<GenPD		
GenUn	C<GenUn		
Pr	C<Pr		
E	C<E		

DEPARTMENT OF ELECTRICAL ENGINEERING
CHALMERS UNIVERSITY OF TECHNOLOGY
Gothenburg, Sweden
www.chalmers.se



CHALMERS
UNIVERSITY OF TECHNOLOGY